Molecular Microplacement Using a Scanning Tunneling Microscope

by

Richard H. Bernhardt

A thesis
presented to the University of Manitoba
in partial fulfilment of the
requirements for the degree of
Master of Science
in
Electrical Engineering

Winnipeg, Manitoba, 1990

ISBN 0-315-63295-X

Canada

MOLECULAR MICROPLACEMENT USING A SCANNING TUNNELING MICROSCOPE

BY

RICHARD H. BERNHARDT

A thesis submitted to the Faculty of Graduate Studies of the University of Manitoba in partial fulfillment of the requirements of the degree of

MASTER OF SCIENCE

I hereby declare that I am the sole author of this thesis.

I authorize the University of Manitoba to lend this thesis to other institutions or individuals for the purpose of scholarly research.

June 21, 1990

I further authorize the University of Manitoba to reproduce this thesis by photocopying or by other means, in total or in part, at the request of other institutions or individuals for the purpose of scholarly research.

June 21, 1990

The University of Manitoba requires the signatures of all persons using or photocopying this thesis. Please sign below, and give address and date.

Abstract

Molecular microplacement using a Scanning Tunneling Microscope (STM) was investigated. Prior to describing the experimental work in this area, a short review of STM is given, with particular emphasis on other researchers' efforts in this area.

Experimentally, materials studied included the *n*-alkanes and other organic liquids, such as dimethyl phthalate. Manipulation was accomplished by the application of a short duration (hundreds of nanoseconds) voltage pulse to the tunneling tip as it scanned a graphite surface. A theshold voltage of about 3.5V was discovered before successful manipulation occurred. In addition, the use of single crystal tungsten tips was found to increase the success rate and the consistency of the process. However, no convincing evidence was discovered to support the contention that the pulse excites chemical bonding between the molecules and the surface.

More exciting results were discovered when a study of the adsorption of the alkanes by the graphite was undertaken. The formation of a highly-ordered two dimensional monolayer of the molecules was observed. From these observations, an imaging mechanism was developed, whereby the carbon atoms of the molecules modulate the barrier height of the underlying graphite surface, leading to a convolution of the molecule with the graphite.

Besides these endeavours, a theoretical study was performed to determine the effect of shot noise in the tunneling junction on the performance of a bandwidth limited instrument operating in the constant-current mode. The noise manifests itself as an uncertainty in the vertical position of the tip. This may cause errors in the identification of surface features and, in the extreme case, may cause destructive contact between tip and surface. For typical operating currents of 1nA and more, the limiting bandwidth will be well into the MHz. However, at very low currents of 1 to 10pA, the limiting bandwidth may fall below 100kHz.

Acknowledgments

I would like to thank Professor Doug Thomson for his guidance and assistance during the work described in this thesis. His help and good humor are very much appreciated. This same appreciation applies to Doctor Gord McGonigal and his particular brand of good humor.

I enjoyed greatly the stimulating environment created by my colleagues within the Materials and Devices Research Lab and the VLSI group. An expression of thanks must go to them. In addition, I want to acknowledge the assistance of the various technicians in the Department of Electrical and Computer Engineering and, in particular, the efforts of Al McKay. Finally, the financial support of the Natural Sciences and Engineering Research Council is appreciated.

Contents

List of Tables

List of Figures

Chapter 1

Introduction

1.1 Preamble

The Scanning Tunneling Microscope (STM) is a recent invention capable of producing an image of a conducting surface with a spatial resolution on the order of several angstroms. To accomplish this, the instrument exploits the quantum mechanical phenomenon of tunneling. In an STM, a pointed probe electrode is placed in very close proximity (usually on the order of 10Å) to the surface of interest. When a small bias voltage is placed across this junction, a tunneling current will flow. The exponential dependence of this current on the separation between probe and surface produces the spectacular resolution of the STM. The current state of the art in Scanning Tunneling Microscopy[1] features a spatial resolution of approximately 2Å parallel to a surface, and less than 1Å perpendicular to it.

1.2 Historical Perspective

The concept of electron tunneling, whereby an electron is able to traverse a classically forbidden energy region, began with the advent of quantum mechanics at the

[1]Hereafter, STM may refer to the instrument (ST Microscope) or the field (ST Microscopy) - the specific meaning will be clear from the context

beginning of the century. Initial efforts in this area were predominantly theoretical, because the problems inherent in experimenting at the distances demanded for tunneling were difficult to overcome. This early theoretical work[1]-[3] laid much of the foundation for later experimentalists.

In the late 1950's, Esaki's invention of the the tunnel diode gave concrete evidence of the phenomenon in p-n diodes[4]. Other experimental successes resulted from advances in the semiconductor processing industry. Specifically, the growth of uniform, good-quality, thin oxide films by thermal oxidation made possible experiments on metal-insulator-metal (MIM) structures; the insulator stabilizes the tunnel gap. The MIM structure was used extensively in spectroscopic measurements designed to probe the vibrational energy states of materials adsorbed onto the insulating layer[5].

No corresponding stabilizing layer is present in a metal-vacuum-metal (MVM) structure. Consequently, work on these systems lagged. One notable exception was provided by Young, Ward and Scire in the early 1970's[6]. They designed and built a device employing a probe electrode scanned above a surface. Unlike the STM however, their device operated with voltages corresponding to field emission described by Fowler and Nordheim. The resolution of the "Topografiner" was 4000Å parallel to the surface, and 30Å perpendicular to it. They did try operating the device in the tunnel limit, with low biases, and with a projected resolution of 3Å perpendicular to the surface. However, precise probe positioning still proved problematic.

The stabilizing effect of the insulating layer is a large advantage enjoyed by a MIM structure over a MVM one. However, due to the solid nature of the insulating layer, the two metal electrodes must be planar. Consequently, the information obtained from MIM experiments is an average over the entire area of the insulator. In contrast, the electrodes in a MVM structure need not be planar; one can then be fashioned into a probe. More importantly, the probe and surface can move relative to one another. This enables the MVM structure to yield spatially resolved information.

Binnig and Rohrer succeeded in moving the probe electrode while controling its position with the precision demanded for tunneling. In 1982, they published the results of their experiments, describing tunneling through a controllable vacuum gap[7]-[9]. For their efforts, they received the Nobel Prize for Physics in 1986.

1.3 Basic Physics of the STM

As described in the preamble, the physical phenomenon exploited in the STM is electron tunneling. For tunneling to occur, the wavefunctions of both the pointed probe electrode or *tip* and the surface must overlap. This will only occur when the tip is located in very close proximity to the surface. Once this condition has been satisfied, electrons are able to *tunnel*, or cross the classically forbidden energy gap which still separates the two electrodes. Figure 1.1 is an energy diagram illustrating the tunneling concept. With the application of bias voltage V, electrons in electrode 1 with energies above E_{F_2} are able to tunnel to empty states in electrode 2. The greatest contribution to the tunneling current is made by electrons at the Fermi level in electrode 1. The tunnel junction shown would have planar electrodes, with a simple trapezoidal energy barrier separating them. In an STM, at least one electrode is not planar, and the barrier does not have the simple shape shown in figure 1.1. However, the basic concept illustrated in the figure does apply to STM. Note that without the applied bias, electrons would still tunnel between the electrodes, but the process would be in equilibrium; consequently, no net current would flow. Only with the application of a bias voltage will a net tunnel current flow.

Simmons[10] has shown that the expression for current density in a tunnel junction with a low applied bias is:

$$J_t \propto V_t \exp -(A\sqrt{\phi}\, s) \tag{1.1}$$

where J_t is the current density, V_t is the applied bias, ϕ is the average barrier between the electrodes, s is the separation between the electrodes and $A = 4\pi h^{-1}\sqrt{2m} \approx 1.025$ with ϕ in eV and s in Å. For the simple barrier of figure 1.1, $\phi \approx (\phi_1 + \phi_2)/2$. However, for the more complicated barriers encountered in STM, and with image forces taken into consideration, this approximation begins to break down.

The approximately unity value of the exponential constant in equation 1.1 indicates the reason for the phenomenal resolution of the STM. For typical barriers of 4 eV, the current may drop by an order of magnitude for a 1Å change in separation. A 1Å separation is on the same order as a change in height of a single layer of atoms;

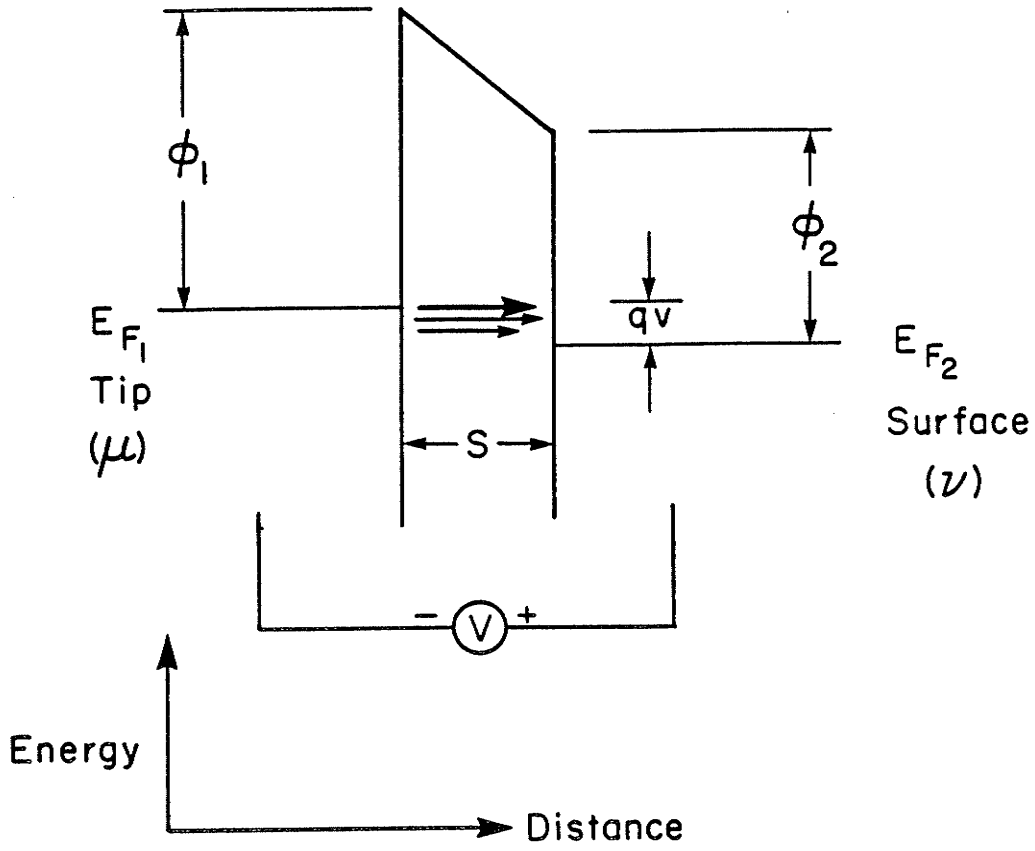

Figure 1.1: Energy diagram illustrating tunneling concept

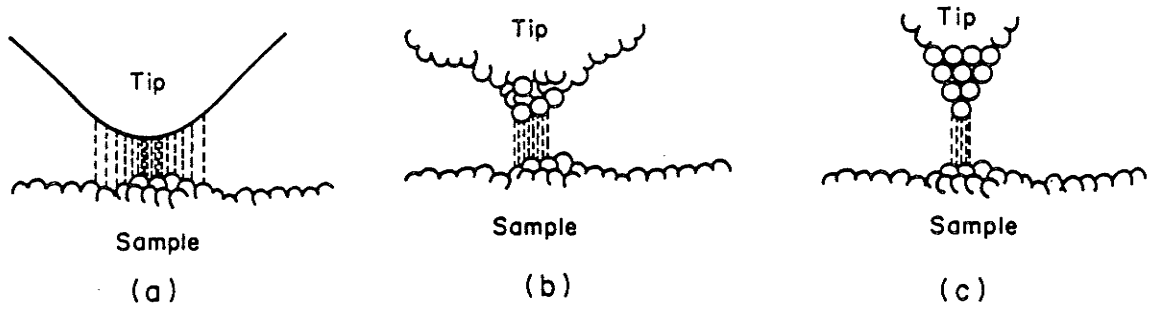

Figure 1.2: Tip structure and resolution. (a) shows situation initially envisioned by Binning and Rohrer. (b) is the experimental reality, while (c) shows the ideal (from[11]).

consequently, most of the current is confined to a narrow beam of atomic proportions defined by at most a few atoms at the apex of the tip. Figure 1.2 illustrates the current confining aspect of the tip, and its importance to the resolution of the STM. Binning and Rohrer first envisioned the situation shown in figure 1.2(a); their calculations indicated that the beam of tunneling electrons would be fairly large, giving lateral resolutions on the order of 45Å. However, their initial images displayed an atomic resolution (ie. on the order of a few Å), so the beam must be confined to a few atoms on a protuberance at the end of the tip, as shown in figure 1.2(b). An ideal STM tip would consist of a single atom at the apex as shown in figure 1.2(c).

The confinement of the tunneling electrons to a few atoms on a tip protuberance is responsible for the high resolution of the STM. As the tip is scanned within tunneling range of the surface of interest, local variations in the structure of the surface change the instantaneous tunneling probability, which in turn changes the current. These current changes are sensed by the instrument, and used to form images of the surface. Two methods currently exist for forming images. The predominant method is the constant current (variable height) mode. In this mode, as the instrument senses a change in the current, it adjusts the vertical position of the tip in order to keep the average current value constant. The vertical adjustments are used to form the image, with increasing image height corresponding to displacements away from the

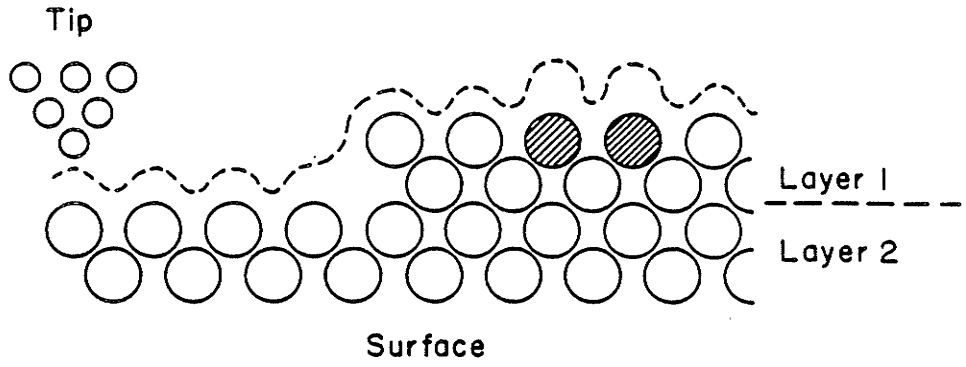

Figure 1.3: Structure variations sensed by the STM

surface and decreasing height corresponding to displacements towards the surface. The second method is the constant height (variable current) mode. Here, the tip is scanned at some fixed separation from the surface. The resulting current is used directly to form the image, with a large current value yielding a large image height, and a small current value yielding a small height. A constant height STM can scan a surface faster than a constant current instrument; however, because of dynamic range limitations in the tunneling current amplifier, it can only be used on monolayer surfaces, as it cannot accommodate large variations in surface height.

The local variations in the surface structure can be divided into two types. The first reflects solely the atomic structure of the surface, while the second is more macroscopic and relates to large scale physical variations of the surface. Figure 1.3 illustrates the two types. The ideal tip, scanning in a constant current mode STM, traces out a contour of constant tunneling probability. This contour changes spatially as a result of the underlying atomic structure of the surface. It also changes as a result of more macroscopic features, such as a monolayer step. In addition, the amount of variation in the contour can itself change because of differences in the chemical composition of the underlying surface atoms. In figure 1.3, the presence of the two different atoms in layer 1 is indicated by a change in the contour. As a result, both the composition of a surface, as well as its topography, can be investigated by the STM.

1.4 Instrument Considerations

At first glance, the concepts behind STM seem relatively simple; however, as the historical perspective pointed out, experimental practice is much harder. This is due mainly to considerations relating to the instrument itself. A typical STM consists of three subsystems:

1. initial tip approach and scanner,
2. electronic control, and
3. vibration isolation.

Each has important problems associated with it.

1.4.1 Initial Tip Approach and Scanner

Although these issues appear connected, each is fairly independent of the other. With the tip in tunneling range, it must be scanned reproducibly in a raster pattern over distances ranging from the atomic to those corresponding to optical wavelengths. In addition, the tip height must be controlled to a precision of approximately 0.1 Å. To accomplish this, piezoelectric elements have been used to date. These are ceramics which will deform or bend when a voltage is applied across them. A tip attached to such a ceramic will then displace slightly. The amount of the bending, and hence of the tip displacement, is a function of the magnitude of the applied electric field, and the size of the element. Problems with piezoelectrics include the need for high voltages (up to several hundred volts) for large displacements, hysteresis effects and creep with large fields.

Initial designs used a tripod scanner, with legs perpendicular to each other. Displacement in each of the three dimensions was controlled by one leg of the tripod. For greater displacements, an individual leg must be made longer, with higher required voltages. Newer designs use a tube scanner[12], with displacements in the

three dimensions affected by a combination of voltages applied around the circumference of the tube's inner and outer walls. The required signals are more complex, but the tube is more compact then the tripod and hence possesses a higher mechanical resonant frequency, which is an important feature for decreasing the effects of vibrations.

Before tunneling can begin however, the tip must be brought from an initial placement close to the surface, done visually by the instrument's operator, into tunneling range *without contacting the surface.* Because it is done visually, the initial placement cannot be closer then about 50μm. The method used for initial approach must be able to move the tip over a very long distance relative to tunneling distances, and yet stop prior to contact. Furthermore, this mechanism must be fairly fast and reasonably free of vibration. Binning and Rohrer used a mechanism called a "louse"[9], which is a walker device incorporating piezoelectric elements to elongate the assembly, and electrostatic clamping to hold one end in place while the other moves. Its movement resembles an inchworm. The "louse" could move in any direction in steps of 100Å to 1μm, with up to 30 steps per second. Drawbacks of the "louse" include the high voltages needed for the piezoelectrics, complicated drive signals and electrical isolation of the assembly from its surroundings in order to allow for electrostatic clamping.

Newer designs use a fine screw driven by a stepper motor. The screw moves a lever to which the tip is attached. The lever has a large mechanical disadvantage, and thereby allows for small tip displacements per step of the motor, which can be driven smoothly at a high number of steps per second. The STM used during the experimental work described in this thesis incorporated this feature. The motor is driven at a frequency of 50 steps/sec, with the tip moving on the order of 500Å per step.

1.4.2 Electronic Control

The feedback control system for most STMs is both proportional and integral. This allows for quick and precise tracking of the surface with a large vertical dynamic range. Note that feedback is used only in conjunction with the z or vertical piezo

signal. The lateral (x and y) signals are usually simple triangular waves. The most important problem associated with the electronic control system is the need to measure nanoampere tunnel currents, at reasonably high frequencies, without adding any noise. Consequently the initial amplifier stage must be quiet electrically. Figure 1.4 shows a schematic of an STM control system using PI feedback. This instrument also uses a tripod scanner. As the voltage on the z piezo is used to form an image, this STM is being operated in the constant current mode.

1.4.3 Vibration Isolation

Tunneling requires operating at angstrom separations. The amplitudes of most building vibrations are well above this value; consequently, an STM must be well isolated from all such vibrations. For their first experiments, Binnig and Rohrer located their instrument on magnets levitating within a superconducting lead bowl. This entire apparatus was itself placed on an air suspended stone bench. This rather exotic and clumsy design was later replaced by a system using eddy-current damping. Still later, the STM community realized that vibrations could be tolerated as long as the entire instrument vibrated in unison. In this way, the separation between electrodes would be maintained, even though the electrodes themselves were moving. To effect this, recent STM designers have concentrated on making the instrument rigid and compact[14].

1.5 Imaging Mechanisms

As described in section 1.3, the tip traces out a contour of constant tunneling probability, which is dependent upon the surface structure. At first glance, this easily understood explanation of the STM imaging mechanism seems complete. However, to fully appreciate the complexity of the imaging mechanism (and therefore to understand the nuances of the images produced by the instrument), the relationship of current to tunneling probability, as found from the wavefunctions of the electrodes, must be examined.

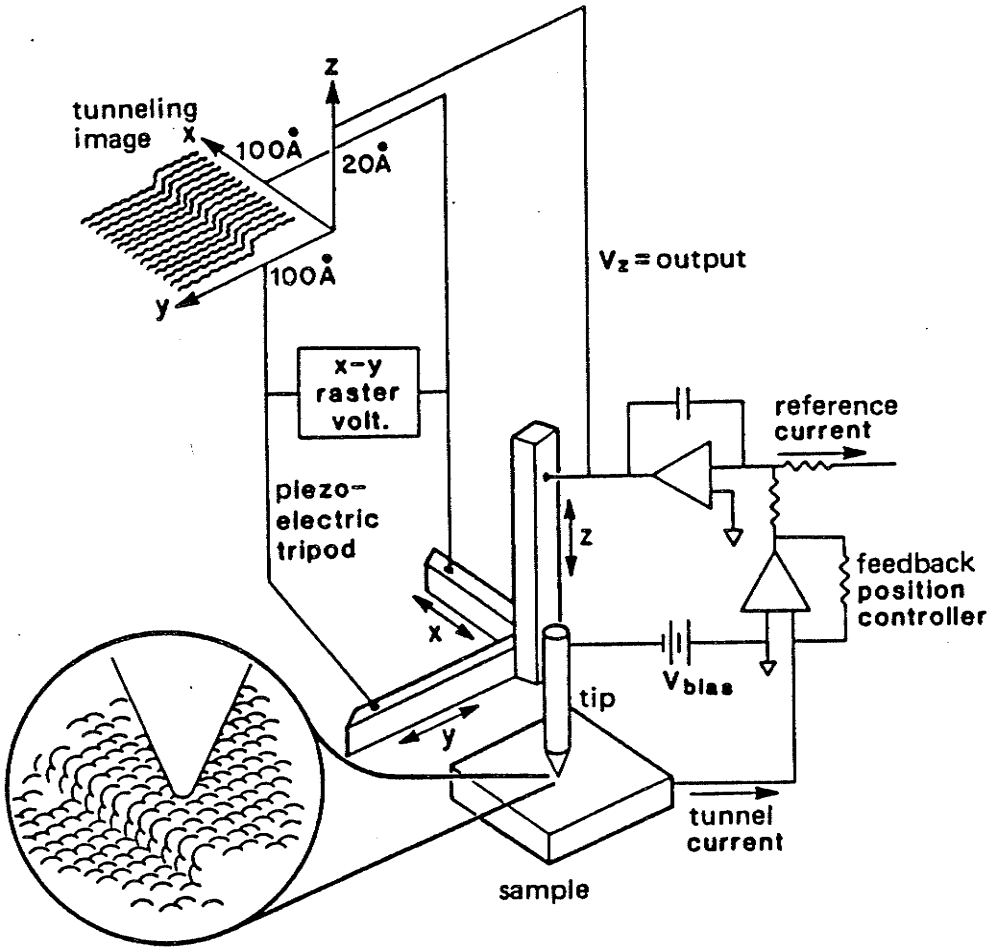

Figure 1.4: Schematic of a constant current mode STM showing control circuitry, piezo's and resulting image (from[13])

The relationship used here between tunneling current and the wavefunctions of the tip and surface is attributable to Bardeen[15]. At low applied bias and temperature, this relationship is:

$$J = \frac{2\pi e^2}{\hbar} V \sum_{\mu,\nu} |M_{\mu,\nu}|^2 \delta(E_\nu - E_F)\delta(E_\mu - E_F) \tag{1.2}$$

where V is the applied bias, $M_{\mu,\nu}$ is the tunneling matrix between states ν of the surface and μ of the tip, and δ is the Kroenecker delta. The tunneling matrix gives the probability of an electron at μ tunneling to ν. It is found from the wavefunctions of the electrodes:

$$M_{\mu,\nu} = \frac{\hbar^2}{2m} \int d\vec{s} \cdot (\psi_\mu^* \vec{\nabla} \psi_\nu - \psi_\nu \vec{\nabla} \psi_\mu^*) \tag{1.3}$$

The expression in the brackets is the current operator; it essentially defines the probability flux flowing across a differential surface element, $d\vec{s}$. This flux is integrated over the total surface to determine the tunneling matrix.

To illustrate how to use these expressions, consider again the energy diagram shown in figure 1.1. This diagram applies to one-dimensional tunneling (symmetric about the other two dimensions), and is not fully applicable to STM. However, it is useful for illustrative purposes. Let x denote a direction parallel to s. Using the WKB approximation, the wavefunctions of the two electrodes are derived as

$$\psi_\mu(x) = C \exp(-kx) \tag{1.4}$$

$$\psi_\nu(x) = C \exp(-k(s-x)) \tag{1.5}$$

$$k = 0.512\sqrt{\phi} \qquad \text{for s in Å and } \phi \text{ in eV} \tag{1.6}$$

where C is a constant and k is the inverse decay length of the wavefunction into the barrier. Note that A in equation 1.1 is twice k. The tunneling matrix for these wavefunctions is:

$$M_{\mu,\nu} = \frac{\hbar}{2m} C^2 k \exp(-ks) \tag{1.7}$$

With this matrix, the tunneling current is:

$$J = \frac{2\pi e^2 \hbar^3}{m^2} C^4 k^2 V \exp(-2ks) \tag{1.8}$$

$$= C' V \exp -(1.025\sqrt{\phi} s) \qquad \text{where} \tag{1.9}$$

$$C' = \frac{2\pi e^2 \hbar^3}{m^2} C^4 k^2 \tag{1.10}$$

This is the same as equation 1.1.

Tersoff and Hamann[16], and Lang[17] developed an expression for the tunneling current between non-planar electrodes. Tersoff and Hamann used Bardeen's formalism and modelled the tip electrode with a sphere of large radius. Lang used a method similar to Bardeen's, with a single atom adsorbed onto one of the planar electrodes. This became the tip. In both analyses, the wavefunction of the tip electrode was spherically symmetric. One possible such wavefunction for the system shown in figure 1.5 would be[18]:

$$\psi_\mu(r) = \frac{1}{\sqrt{\pi a^3}} \exp(-r/a) \tag{1.11}$$

where a is the Bohr radius, or width of the ground state in the atom's potential well. The surface wavefunction would have the same form as equation 1.6. The calculation of expression 1.3 defining the tunneling matrix is complicated by the need to work in cylindrical coordinates. The tunneling matrix is:

$$M_{\mu,\nu} = \frac{\hbar\pi}{m}\left[\frac{C}{\sqrt{\pi a^3}} sa \exp(-s/a)\right][k + a^{-1}] \tag{1.12}$$

$$= C' s \exp(-s/a) \qquad \text{where} \tag{1.13}$$

$$C' = \frac{\hbar\pi}{m}\left[\frac{C}{\sqrt{\pi a^3}} a\right][k + a^{-1}] \tag{1.14}$$

and the tunneling current is:

$$I = (C')^2 V s^2 \exp(-2s/a) \tag{1.15}$$

The exponential dependence of the current on separation is maintained, but additional terms appear in the pre-exponential factor. Tersoff and Hamann interpreted their corresponding result as an indication that the tip follows a contour of constant local density of states (LDOS) at the Fermi energy. Therefore, an STM image represents a map of constant surface LDOS. They further determined that variations induced by a non-spherical tip wavefunction would only appear in the prefactor, and would be overwhelmed by the exponential term.

Chen disagreed with the assumption of a spherically symmetric tip wave function[19]. He supported his argument by showing that the resolution predicted by Tersoff and Hamann is less then that encountered experimentally. He performed an analysis

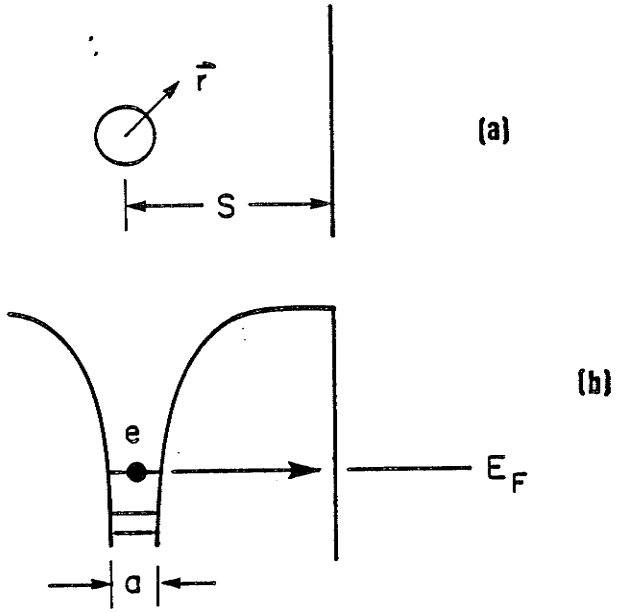

Figure 1.5: Spherical tip wavefunction - (a) shows spatial geometry, while (b) shows energy diagram (from[18])

whereby the apex atom is represented by different atomic states, some of which are not spherically symmetric. With these, he was able to predict more consistent resolution figures. However, his results still indicate an exponential dependence on separation.

Current in the STM varies exponentially with electrode separation. This variation is modified *slightly* by a prefactor, which itself depends upon the nature of the tip. Consequently, the exact interpretation of STM images will also vary. However, Tersoff and Hamann point out that in the limit of arbitrarily small tip radius, the tunneling current expression will reduce to:

$$I \propto \sum_{\nu} |\psi_{\nu}(\vec{r_0})|^2 \delta(E_{\nu} - E_F) \tag{1.16}$$

where $\vec{r_0}$ is the position of the probe. The right hand side of this equation is the local density of surface states at the Fermi energy; any dependence on the tip wavefunction has vanished. So ideally, the STM is sensitive solely to this feature of the surface. A spectroscopic measurement technique which exploits this sensitivity is described in section 1.7.

1.6 Anomalies

The tunnel current varies exponentially with electrode separation; the exponential constant is on the order of 1Å. However, some anomalies have been observed whereby the tunnel current remains constant even though the separation has apparently changed by hundreds of angstroms. Most notable are anomalously high corrugation amplitudes associated with highly oriented pyrolytic graphite (HOPG) surfaces observed in air. HOPG is the substrate of choice for many STM researchers because it is reasonably inert, atomically flat over vast areas and yields images of its atomic structure readily. The corrugation referred to is the normal variation in height that the tip experiences as it scans the surface in a constant current mode STM. Many researchers have noted the anomalous corrugation values, and proposed reasons for them.

Tersoff suggested that they were the result of the unique electronic structure of HOPG[20]. His analysis suggested that STM graphite images would be dominated by its electronic structure with the result that no atomic structure could be distinguished. This seems to be in conflict with experimental observations.

Soler et al. suggested that a single tip atom is actually in contact with the graphite and compressing it, as HOPG is a fairly spongy material[21]. As the tip scans the surface, it normally undergoes a series of advances towards and retreats from the surface. In the explanation proposed by Soler et al. the compressed graphite will rebound with the tip as these height changes occur, as shown in figure 1.6. Thus, a large change in tip height would be needed to effect any change in current. This results in the large corrugation amplitudes.

Pethica observed some flaws in the explanation of Soler et al.[22]. He showed that the single tip atom could not sustain the force on it resulting from compression of the surface without bending. In addition, he noted that the surface may also shear because of the force. This lead him to suggest that the top layers may be sliding with the tip over deeper layers, allowing for the lateral resolution observed on HOPG.

Coombs and Pethica use a contact theory similar to Soler et al. to explain anomalous barrier height measurements[23]. This measurement method is discussed later

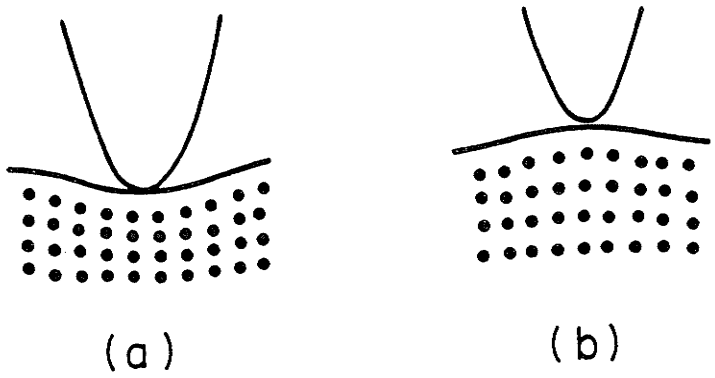

Figure 1.6: Explanation for anomalous corrugation values. In (a), the tip is compressing the surface. In (b), the tip has retracted with the HOPG following (from [21]).

in section 1.7.2. They proposed that the tip and surface are in contact through a non-conducting contamination particle. The tip would compress the surface through this particle until some other point on the tip came into tunneling range. Again, as the tip moved vertically, the surface would follow, leading to large corrugation amplitudes.

Mamin et al. extended this theory and provided some supporting experimental evidence[24]. They suggested that a contamination layer exists on the tip which extends over a vast area, yielding uniform graphite compression. A small tip protruding into the contamination provides a tunneling path. Experimentally, they found the largest corrugation amplitudes at low biases and high currents, where the separation must be small, and as a result the compression must be large. Soler et al. encountered similar results experimentally. Mamin et al. then subjected their tip and surface to repeated cleaning cycles in vacuum. At the conclusion of these cycles, the measured corrugation had diminished significantly, indicating that the contamination had been removed and could no longer compress the HOPG. The final amplitude measured was 0.9Å which agrees with the predicted value for HOPG.

This contamination layer has huge implications for STM experiments. These include:

1. material deposited onto surfaces may be removed inadvertantly by the contamination,

2. feature elevations determined solely on the basis of changes in tip height may not be accurate, and

3. surface modification may occur as a result of prolonged contact with the contamination layer.

As a result, caution must be excercised when performing experimental work and interpreting results.

1.7 Spectroscopy

The measurement capabilities of the STM can be extended through use of the instrument in a spectroscopic mode. Spectroscopy can give details of the electronic and chemical structure of a surface which may not be present in a topographical image, or which may be inadvertently interpreted as a topographical feature. As will be described in section 1.8, one group of researchers, Jahanmir et al. attribute their observed features to a change in the electronic structure of their surface, rather than to a change in its topography. However, this electronic change could be confused with a topographical feature. In a similar manner, the change in the chemical structure of the surface in figure 1.3 may be interpreted as a topographical change. Spectroscopy can unmask the subtle changes and clarify the confusing ones. And it can do this with the resolution inherent in the STM.

Two STM spectroscopic techniques are available; each yields different information about the surface. The first is similar to the MIM spectroscopy mentioned in section 1.2. It is used to probe the electronic structure of the surface; in addition, it can be extended to probe the vibrational modes of molecular adsorbates on the surface. STM researchers have given this technique various names, such as local tunneling spectroscopy (LTS), scanning tunneling spectroscopy (STS) or simply spectroscopy.

The second technique is usually called barrier height imaging or ϕ imaging. This technique reveals information related to the nature of the tunneling barrier, which

is a function of both the chemical makeup of the surface atoms as well as their local electronic structure.

Binnig and Rohrer[25] and Behm and Hösler[26] provide a good introduction to spectroscopic work in STM, as well as a good overall review of STM in general.

1.7.1 More Spectroscopy

At room temperature, this measurement technique is used to probe the electronic structure of a surface, or the local density of states at the Fermi level. Figure 1.7 illustrates the concept behind these spectroscopic measurements. This figure is similar to figure 1.1. The LDOS is shown as a function of energy. They are filled below the Fermi level and empty above it. Only those electrons with energies within ΔE can contribute to the tunneling current. As the bias voltage V_t changes, so does the portion of the LDOS which can contribute to the current. Consequently, the magnitude of the current will provide an indication of the structure of the LDOS; that is, the current will yield information about the electronic structure of the surface. The STM tip can probe the structure of both empty and filled states on the surface. In figure 1.7(a), the tip examines the filled states of the surface, while in (b), the empty states are examined. A simple change in the polarity of the bias voltage is the only requirement necessary to allow for this. The STM can provide this probing feature with the same resolution with which it images the topography of a surface.

There are a number of ways to perform spectroscopic measurements. LTS provides the most detailed information about a local area. To do this, the scan is halted, and the measurement is made with the tip held motionless above the surface. Two distinct measurement methods may be employed. The simplest involves ramping the bias voltage and measuring the tunneling current. Fluctuations of the current from a straight line provides the LDOS information. Note that the electrode separation must be held constant during the voltage ramp or else current changes attributable to varying separations would distort the spectroscopic results. In a constant current mode STM, this necessitates breaking the z feedback control loop.

The second and much more popular technique for performing LTS again involves

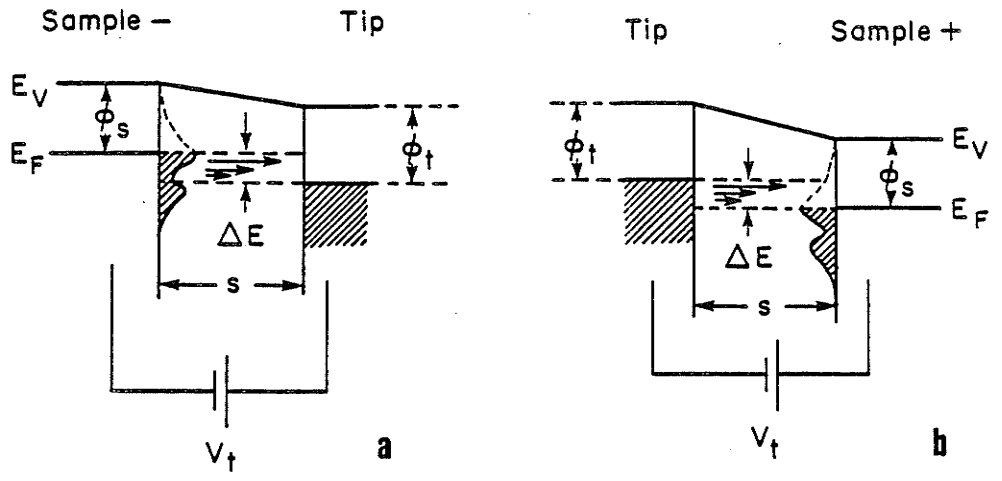

Figure 1.7: Energy diagram illustrating spectroscopy measurement. In (a), filled states of the sample are probed, while in (b), empty states are probed (from [26]).

ramping the bias voltage with constant electrode separation. However, a small voltage modulation is added to the bias. A lock-in amplifier measures the resulting modulated current. In this way, the conductance (dI/dV) is measured as a function of bias voltage. Peaks in the conductance correspond to a high LDOS. A conductance versus voltage spectrum of a NiO island discovered on a Ni(100) surface is shown in figure 1.8. The signal to noise ratio is increased using this coherent detection scheme.

LTS provides a conductance versus voltage spectrum for one particular area on the surface. It does not give an image of the surface. STS will give an image, at the expense of lowered spectral detail. As with LTS, two measurement methods are possible. The easier method involves the subtraction of two images taken at different bias voltages, *with no change in electrode separation allowed between the two scans.* The second involves the coherent detection technique described above. A small voltage modulation is again added to the bias voltage and the conductance measured as the surface is scanned. The gap distance is maintained during the scan by the usual z feedback control. However, the image is formed using the conductance information, rather then the z voltage information. Note that the bias modulation must be at a sufficiently high frequency that the feedback control circuit cannot respond to any

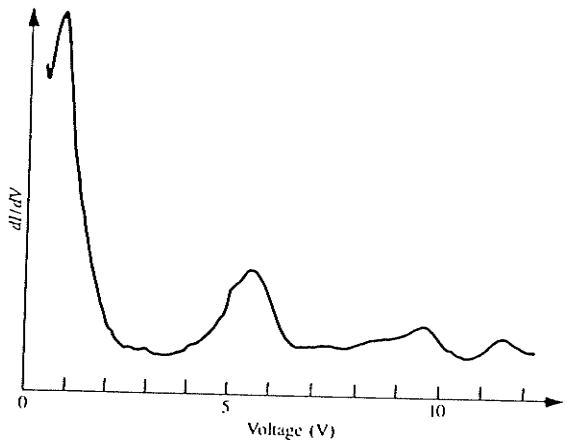

Figure 1.8: Conductance spectrum of NiO on Ni(100) (from [25]).

modulation induced changes in tunneling current. To obtain a complete spectrum, multiple images at different bias voltages must be taken, again without a change in electrode separation between scans.

An STS image in general contains both spectroscopic information, as well as a background which corresponds roughly to the surface topography[25]. Because of this, an STS image set can be difficult to interpret. A single STS image contains little information of a spectroscopic nature. However, the underlying topographical information may help locate a significant spectroscopic feature. In contrast, LTS provides an entire spectrum, but only of one small area on the entire surface. Both methods therefore have drawbacks as well as advantages.

At room temperature, the total energy of an individual tunneling electron cannot be determined exactly, as it will have some unknown thermal energy. The variation will be limited to 50meV, which is related to the average thermal energy of an electron in a room temperature environment. Because of this, individual conductance lines with widths of less then 50meV cannot be resolved by the aforementioned spectroscopic techniques. Consequently, measurement of the vibrational states of molecules adsorbed on the surface by inelastic tunneling spectroscopy[27] cannot be done at room temperature[28]. However, theoretical work indicated that inelastic tunneling processes may be measured by an STM operating at cryogenic temperatures[29].

Such operation has taken place[30].

1.7.2 Barrier Height Imaging

The concept behind barrier height or ϕ imaging can best be seen by considering equation 1.1, which is repeated here,

$$I_t \propto V_t \exp -(A\sqrt{\phi}\, s) \tag{1.17}$$

The value of the barrier height ϕ can be found from

$$\left|\frac{d \ln I_t}{ds}\right| \approx \phi^{1/2} \tag{1.18}$$

A number of different methods can be used to actually measure $\phi^{1/2}$. The simplest involves subtracting two images taken at different currents, with no change in bias voltage permitted between scans. The most popular method is similar to the coherent detection of conductance described above. The z piezo control voltage is modulated at a frequency above the control system bandwidth, and the resulting changes in the natural logarithm of the current measured at the same frequency with a lock-in amplifier. This is done as the surface is scanned, with the values measured at each point used to form an image. Note that $\phi^{1/2}$ can also be found by modulating the z piezo voltage and measuring the bias voltage change required to maintain a constant current. As most instruments do not operate in this manner, this method of obtaining $\phi^{1/2}$ would be somewhat more difficult.

The barrier heights measured would be a function of the local electronic structure and the chemical composition of the surface. In one of their original papers, Binnig and Rohrer[9] used barrier height imaging to distinguish between Au islands and the underlying silicon substrate. Behm and Hösler[26] consider the barrier height measurement to be sensitive principally to changes in the surface chemical composition.

Some barrier height measurements have yielded anomalously low values, not in keeping with the values expected from equation 1.18. The same mechanism causing the anomalously high corrugation values is responsible for the low barrier heights. As described in section 1.6, a contamination layer compresses the substrate; this causes

the surface to follow the tip when its height is adjusted. Resulting current variations are slight. That is, a given dz results in a much smaller actual change in separation s between tip electrode and sample, yielding a current change much smaller than expected. Both Coombs and Pethica[23] and Mamin et al.[24] noted this cause for low barrier height measurements.

The barrier height should be the average of the work functions of the two electrodes. However, this is a first approximation which neglects the image potential. Binnig et al. calculated the barrier height expected from equation 1.18 with the potential in the gap modified by image forces[31]. They found that this apparent barrier height differed little from the average of the two workfunctions. Their image-force lowered approximation to the potential in the gap cancelled when the derivative of the current was taken. Payne and Inkson[32], Coombs et al.[33] and Pitarke et al.[34] echoed the calculations performed by Binnig et al.; however, these other researchers used more complicated approximations to the image potential in the gap. They also found that the apparent barrier height closely approximates the average of the electrodes' workfunctions, with the correspondence digressing only as the electrode separation collapsed to intimate contact. Lang also performed similar calculations; but, unlike the others, his apparent barrier height began to differ from the workfunction average at a considerable distance away from intimate contact[35]. However, he used the findings of Binnig et al. that image potential had little effect on the apparent barrier height, and ignored the image potential at the beginning of his calculations. Consequently, his results are suspect.

Ideally, measurement of the barrier height taken on a chemically homogeneous surface should yield an image with no variations in surface height. However, barrier height images always include a topographical contribution. The reason for this can be seen in figure 1.9. The modulation of the z piezo does not result in a modulation of the gap spacing normal to the surface, which is demanded by ds in equation 1.18. The measurement made is in fact of $d\,(lnI)/dz$, not $d\,(lnI)/ds$. Consequently, topographic features are coupled into the barrier height images. The two are related in the following way:

$$\left|\frac{d\,\ln I}{dz}\right| = \left|\frac{d\,lnI}{ds}(s\cdot z)\right| \approx \phi^{1/2}\,|(s\cdot z)| \tag{1.19}$$

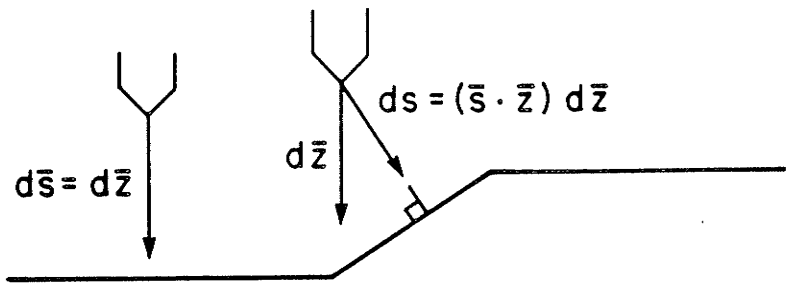

Figure 1.9: Relationship between dz and ds (from [36])

where $(s \cdot z)$ is the dot product of the normal to the surface at each point and the direction of tip modulation. Gómez et al. describe a method for decoupling the topographic and barrier height information using a technique which exploits this relationship[36].

1.8 Nanolithography

Besides merely examining surfaces with atomic resolution, the STM offers the possibility of manipulating matter on this scale. This could be extremely useful for biological applications involving genetic engineering; equally interesting would be its application to nanolithography. In this application, the STM would create patterns on semiconductor surfaces; these patterns would define electronic circuits. The advantage of the STM over more conventional lithographic methods, such as electron beam lithography, lies in its potential to create patterns with much smaller linewidths. This would result in a greater density of circuitry and a higher level of integration than currently possible with existing methods.

For the purposes of this thesis, nanolithography is considered to be the deposition of material onto a surface; mere modification of the existing surface is not considered nanolithography. Many researchers have attempted some form of manipulation with the STM. A portion of this work is just modification of the existing surface and hence not true nanolithography. However, it will still be discussed here, as it provides an indication of the capabilities of the STM.

In addition, some of the nanolithography or surface modification experiments were performed with an STM operating out of its usual tunneling regime, with the resolution of the instrument degraded. This is also included, as it demonstrates the versatility of the instrument.

McCord and Pease[37]-[41] used an STM operating in field emission, like the "Topografiner" of Young et al. By operating at higher voltages than usual for an STM, electrons at the tip undergo Fowler- Nordheim emission[2] with the result that the tip becomes the source (or collector) of a low energy electron beam. Their initial calculations indicated that such a beam would feature a radius of 200Å with high currents (up to 100μA), but with a low electron landing energy of approximately 100eV[37]. In addition, they found that the beam radius diminishes with decreasing electron energy. To confirm their predictions, they performed a series of studies in which various resist materials were irradiated with the STM electron beam.

In their first study[39], a variety of target surfaces were used, including bare silicon, and metal films (Au, Al, Cr and Pt) vacuum deposited on silicon. The composition of the tip was not specified. The deposition resist used was "contamination"[2] and docosenoic acid. A 10V, 60nA beam moving at 0.1μ/s formed lines with widths less then 0.1μm onto gold using the contamination resist. A 25V, 15nA beam traveling at 0.5μm/s formed lines with comparable widths onto aluminum out of the docosenoic acid; however, the quality of the lines was poorer. The exact mechanism for the deposition of the lines was not discussed.

In their second study[40], the resist material used was primarily calcium fluoride. Using a 20V, 2nA beam moving at 0.85μm/s, 200Åwide lines were formed. Aluminum flouride and lithium fluoride also yielded similar results. The mechanism for the deposition was thought to be electron stimulated desorption, which requires a minimum energy of 26eV. Because lines were formed with a 20V beam, some other mechanism must be involved.

In their third study[41], the resist material was poly(methyl methacrylate) or PMMA, a popular polymer resist used in electron beam lithography. The PMMA was patterned by the STM electron beam, and metal lines formed using a lift-off

[2]Contamination is predominantly hydrocarbons naturally found on most surfaces

metallization process. Using a 20V, 100pA beam traveling at 1μm/s, 200Å wide lines were obtained.

The experiments of McCord and Pease confirm that an STM can be used for nanolithography. While improvement in attainable line widths was made, the use of the field emission regime degrades the resolution of the instrument, and sacrifices some of the STM's potential. Their experiments also pointed out a number of problems common to all nanolithography attempts with the STM, namely uncertain deposition mechanisms, and slow speeds of patterning.

Later, McCord et al.[42] and Ehrichs et al.[43, 44] formed deposits from organometallic gases. McCord et al. used a 30V, 10nA beam moving at 0.25μm/s to form 100Å wide lines. They also formed metallic dots with a 300Å diameter using a 25V, 20nA beam. Ehrichs et al. used two different techniques. In the first, they decreased the tip-surface separation with the tip biased between 1 and 5 volts. During the approach of the tip, the current increased to 1 to 300μA. A deposit results from this procedure. Features with diameters of 200Å and lines with widths of 250Å were formed. In the second technique, as the surface was scanned, voltage pulses with amplitudes ranging from 2 to 10V and durations of 10 to 400ns were applied to the tip. Lines with widths of 200Å were formed. Ehrichs et al. were most successful with no gas present in their chamber. They believed that they were also using a "contamination" resist. In addition, Ehrichs noticed that the pulse must exceed a threshold of approximately 3.5V to form any deposits. Again, the exact mechanisms involved in the formation of the deposits remained unknown.

Lin et al.[45] also produced patterns using an STM operating in a non-tunneling mode. The process cannot be considered nanolithography as no material was deposited onto the GaAs substrate. Instead, the STM was used to promote a photoelectrochemical etch of the surface. Initially, the instrument was used in the low voltage tunneling mode; the surface was examined to ensure that no tilt nor roughness exists which may cause problems during the etch. The partially insulated tip was then raised to approximately 1μm above the surface and an electrolytic solution introduced. The tip then scanned the substrate again, while at the same time a light irradiated the area. The light radiation and localized current promote an etch of the surface. Etched line widths ranged from 0.3 to 2μm.

Surface modification by direct contact between surface and tip has also been achieved by a number of researchers. McCord and Pease used the tip to machine 0.36μm wide lines in 200Å thick films of calcium fluoride and aluminum fluoride which had been vacuum deposited onto silicon[46]. The process did no apparent damage to the tip nor the substrate. Jaklevic and Elie made deformations in a gold surface by applying a short duration voltage pulse to the z piezo control voltage[47]. They were not interested in surface modification per se; instead, they wished to observe the self-diffusion of gold. However, they did notice that the z voltage would change after the contact had taken place, indicating that the tip had approached towards or retreated from the surface. They interpreted this to mean that some material had been transferred onto or off of the tip. Other experimenters have observed this change during surface modification experiments. Van Loenen et al. also formed indentations, but in silicon[48, 49]. Like Jacklevic and Elie, they also changed the voltage on the z piezo to push the tip into the surface. The indentations had typical diameters of 20 to 100Å; size could be controlled by varying the depth of penetration of the tip into the surface. Using a matrix of the indentations, they were able to form lines and figures. Like McCord and Pease, the tip, made of tungsten, suffered no apparent damage during the procedure.

Surface modification attributed to localized heating and melting was explored by Staufer et al.[50]-[52]. The substrate used was a glassy $Rh_{25}Zr_{75}$ alloy. Hillocks were formed by increasing the bias voltage to 2V and the tunneling current to 315nA, with the scan stopped. After approximately 5 seconds, the current began to oscillate, and the control system withdrew the tip. This behaviour is attributed to the movement towards the tip of a molten portion of the surface; the melt is attracted because of the strong electric field, forming a Taylor cone. Hillocks formed in this manner had diameters of 350Å and heights of 100Å. Lines and complex patterns were also created. Typical line widths were 200Å. Structure size could be controlled by application of variable biases, yielding a range of diameters from 40 to 115Å. Structures were also formed on other glassy alloys, such as $Fe_{86}B_{14}$, and the ferrimagnetic $Co_{35}Tb_{65}$. Ringger et al.[53] also used a glassy alloy, $Pd_{81}Si_{19}$ for a substrate. However, they formed lines simply by scanning the surface at a bias of 100mV with a current of 10nA. Scan speed was 0.1μm/s. The resulting lines were less then 500Å wide. The

deposition mechanism was not attributed to heating; instead, they believe that a polymerization of a hydrocarbon contamination film may have occurred.

A number of researchers have performed surface modifying experiments on gold. Abraham et al.[54] produced indentations through contact by the tip, and observed surface self-diffusion, just as Jaklevic and Elie did. They produced depressions with typical diameters of 100Å and depths of 30Å. In addition, they also formed hillocks on the surface by increasing the tunneling current to 1μA with a 5mV bias. These hillocks were initially 200 to 250Å wide and 20Å high. They believe the hillocks were formed by the deposition of material from the tip to the surface. This material would be gold transferred to the tip on previous inadvertent touches with the surface.

Schneir et al. also produced both holes and mounds on a gold surface[55, 56]. Unlike Abraham et al. and Jaklevic and Elie, they worked in air, with the gold surface covered with a fluorocarbon grease. To modify the surface, the scan was stopped, and the bias was raised above the nominal level of 0.1V until the z voltage increased suddenly. Holes were usually formed if the bias reached 1.5 to 3V before the z voltage changed, whereas mounds usually formed if the z voltage increase occurred at 0.7V. Mounds were typically 100Å wide, while holes were usually smaller with widths of approximately 50Å. The researchers could not influence the type of feature formed. No modifications were possible if the grease was not present. In addition, not every attempt in the presence of the grease was successful.

Li et al. also increased the bias voltage in order to modify a gold surface[57]. However, they pulsed the bias, and continued to scan the surface during the pulse. They operated in air, with no substances deliberately introduced onto the surface. Their millisecond duration pulses typically formed craters which were 20 to 80Å in diameter. Sometimes, mounds with diameters approaching 200Å were formed. If mounds did form, the measured current saturated at approximately 90nA for up to 2ms, while it would only momentarily peak at the saturation value if craters were formed. In addition, observation of the voltage on the z piezo indicated that, following a surface-modifying pulse, the piezo returns the tip to a different nominal distance from the substrate in an attempt to maintain a constant current. The direction of the change in separation following formation of a hole is opposite to that following formation of a mound. Like Schneir, not every attempt was successful; Li et al.

also found that a threshold voltage of approximately 2.7V must be exceeded for any modification to occur. They speculated that explosive evaporation caused by rapid heating may cause the craters. This suggestion has been discounted by others[60], as the heat generated by the pulse is conducted away from the surface too quickly to allow for explosive evaporation.

Emch et al.[58] also used voltage pulses while scanning to modify a gold surface. They too created both craters and, less frequently, mounds. Like Li, they noted a voltage threshold of around 3V. In addition, they found that the thresold would approach 5V if the tip was blunt or dirty. Besides a voltage threshold, they also determined that a minimum pulse width was necessary. This was approximately 10ns. Their smallest features were on the order of 50Å wide.

Other researchers have performed surface modifying experiments on graphite. Albrecht et al. were able to obtain near atomically resolved images of poly (octadecyl-acrylate) or PODA, a polymer resist similar to PMMA, on graphite while operating in air[59]. By applying a 100ns duration voltage pulse to the tip while it was located over a portion of the PODA molecule, fibrils were modified and apparently cut. A voltage threshold of about 4V was found for this behaviour.

Foster et al. also performed experiments to deposit organic molecules, such as dimethyl phthalate, onto graphite from the liquid phase, with the STM operating in air[61]. As with Albrecht, a submicrosecond voltage pulse was applied to the tip in an effort to "pin" all or a portion of the molecule to the graphite. The sizes of the features formed in this way were of the same order of the graphite lattice; that is, approximately 4Å, which is an order of magnitude smaller then features formed by other means. A voltage threshold between 3 and 4 volts was reported. Mechanisms for the deposition were discussed, but no concrete determinations were possible.

Besides forming deposits on graphite, craters have also been formed. Albrecht et al.[60] produced craters using the same technique used to produce deposits; that is, by applying voltage pulses to the tip. Pulse amplitudes necessary to form craters varied from tip to tip and ranged from 3 to 8V. Pulse widths also varied between 1 to 100μs. Typical holes were 7Å deep and 40Å in diameter. Some tips failed to produce any craters. In addition, the process was foiled when attempted in vacuum

and in the presence of dry gases. The mechanism responsible for the formation of the craters is not well understood, but appears to be electrochemical in nature.

Becker et al. performed surface modification experiments on germanium in UHV[62]. They deposited material onto the surface by increasing the bias voltage with the scan halted. The diameter of the deposition was approximately 8Å with a height of 1Å. Not every attempt was successful; however, the success rate could be increased by lightly contacting the tip with the surface. Because of this, they attribute the deposition mechanism to an electrostimulation of Ge atoms adhered to the tip back onto the surface.

Jahanmir et al. modified the surface of a thin amorphous Si:H film on silicon while operating in air[63]. Like other researchers, they also applied voltage pulses to the tip. Their pulses were 10V in amplitude and 35μs long. These pulses produced lines with widths of 0.14μm. However, they do not believe that the lines correspond to actual topographical changes. Instead, they believe the lines were due to conductivity changes in the film caused by local crystallization induced by the pulse; that is, the features are the result of a change in the electronic rather then the topographical structure of the surface.

This body of work gives a vivid indication of the ability of the STM to perform surface modification and nanolithography on a scale close to atomic dimensions. However, because of unknown deposition mechanisms, the field remains very much an art as opposed to a science.

Chapter 2

STM Description

2.1 NanoScope I

The research for this thesis was performed using a commercially available STM, called the NanoScope^{TM} I, manufactured by Digital Instruments of Santa Barbara, California. Upon delivery, the NanoScope I consisted of three parts:

1. the microscope,
2. the control unit, and
3. a storage oscilloscope.

The storage oscilloscope, which is used to display images of surfaces, is made by another firm. It is a model COS5020-ST manufactured by Kikusui Electronic Corporation.

The NanoScope I is a recent design with many of the desirable features described in section 1.4. These include:

1. a piezoelectric tube scanner,
2. a stepper motor driven lever arrangement for coarse positioning,

3. proportional and integral feedback control, and

4. a compact and rigid structure.

The tube scanner can be driven with voltages up to ± 150V in all three dimensions, yielding a displacement of approximately 0.6μm in each. Digital Instruments claims that the unit is so insensitive to vibrations that it could be located and operated on a ground level concrete floor. However, to ensure good vibration isolation, the microscope was placed on a platform which is suspended by bungee cords from a supporting tripod; this tripod is itself sitting on an air supported granite slab which formerly was used as an optical table. The NanoScope I is a constant current mode instrument.

2.1.1 The Microscope

The microscope is a tiered structure about 17cm high with the cover shell removed. It consists of a base, a sample stage and a scanning head. The base is an thick-walled aluminum tube with a diameter of 12.5cm and a height of 7cm. It houses the stepper motor and a second amplifier stage. The first stage amplifier, or preamp, is located on the scanning head, which is described below. A plate acts as a lid on top of the base; the stepper motor shaft protrudes through this plate. The lid also acts as a foundation for four columns which support the sample stage.

The sample stage sits 4cm above the base. The sample is mounted horizontally on top of the stage and held in place with a tungsten clamp. Even though the bias voltage is applied to the entire stage, the clamp acts as an electrode to ensure that continuity with the sample occurs. Extending vertically through the sample stage are three magnetized screws, arranged in a triangular pattern. Two of the screws are turned manually by the operator of the instrument. The third is connected by a flexible driveshaft to the stepper motor. Ball bearings have been emplaced into the ends of the screws. The scanning head sits on top of these three bearings; the magnetization acts to hold the head firmly in place. The manually turned screws allow for initial placement of the tip by the operator. Then, coarse approach of the surface is provided by the stepper motor driven screw.

The entire scanning head[1] acts as the lever for the coarse approach. The sample is located between the two manually turned screws. A line connecting the two screws can be considered the fulcrum for the lever. When the scanning head is in place, the tip is held just slightly in front of this fulcrum. The motor driven screw meanwhile is substantially further away; the mechanical advantage for this arrangement is approximately 0.12. Like the base, the scanning head is also cylindrically shaped, with a diameter of 3cm and a height of 2cm. The tube scanner is fitted into the scanning head. Epoxied to the scanner is a small ceramic collar. A small hole in its center accommodates a stainless steel tube with a 12 thou inner diameter. This tube will accept 10 thou diameter tips. A length of #32 wire is soldered to the tube and routed to the preamp. This provides an electrical connection from the tip, through the tube to the preamp.

The preamp is affixed to the top of the scanning head. A schematic diagram of it is shown in figure 2.1. The tunneling current flows through the 1MΩ resistor to ground. The voltage developed by this current is applied to the non-inverting terminal of a low noise op-amp, which amplifies the voltage by a factor of 100. In this way, the tunneling current is converted to a voltage and amplified. It is later fed through an absolute value circuit; this allows use of bias voltages of either polarity. The current-to-voltage conversion circuit has a drawback. Part of the bias voltage is dropped across the 1MΩ resistor. Consequently, the voltage across the tunnel junction is reduced by an amount equal to the tunnel current value multiplied by 1MΩ. Consequently, the bias voltage will be reduced by 1mV/nA (ie. 1nA x 1MΩ = 1mV).

2.1.2 The Control Unit

A block diagram of the control unit is shown in figure 2.2. The diagram shows the feedback board, the x - y raster scan board, the interconnections to the piezo scanner, and the amplifiers located with the microscope. Besides specifying a bias voltage, the operator of the instrument must set also specify a tunnel current value, called

[1]Interchangeable scanning heads with different ranges are available from Digital Instruments. The one used is described here.

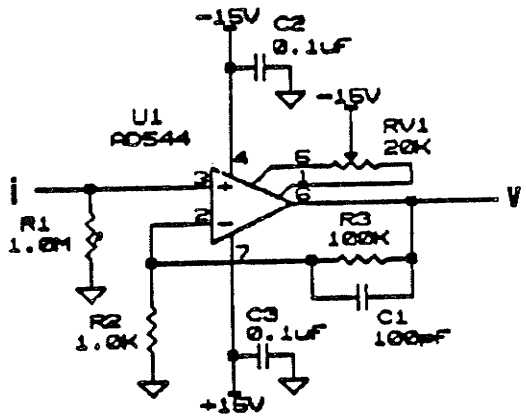

Figure 2.1: Preamp schematic diagram (from [64])

the setpoint current, denoted as **I set** in figure 2.2. As the NanoScope operates in constant current mode, the feedback board circuitry will adjust the z piezo voltage to keep the average current equal to the specified setpoint. Note that figure 2.2 does not show an outline of all the circuitry housed with the control electronics. For example, the stepper motor drive electronics is missing. However, the figure does present all the information needed to appreciate the control system of the actual microscope.

2.1.3 Display Oscilloscope

The NanoScope I was designed to display its images directly on a storage oscilloscope. The Kikusui oscilloscope is used for this purpose. The scope trace is moved across the screen in unison with the movement of the tip above the surface of interest. As shown in figure 2.2, the x scan voltage drives the horizontal motion of the scope trace. The vertical motion of the scope trace is controlled by a combination of the y scan voltage and the z control voltage. A third signal is used to control the intensity of the trace on the scope screen. It is derived from the z proportional control voltage. This combination of signals allows for two different types of image displays.

The first type can be considered a gray scale or contour image. The vertical motion of the scope trace is controlled solely by the y scan voltage. As the trace is scanned over the screen, the intensity of the beam is modulated by the z proportional

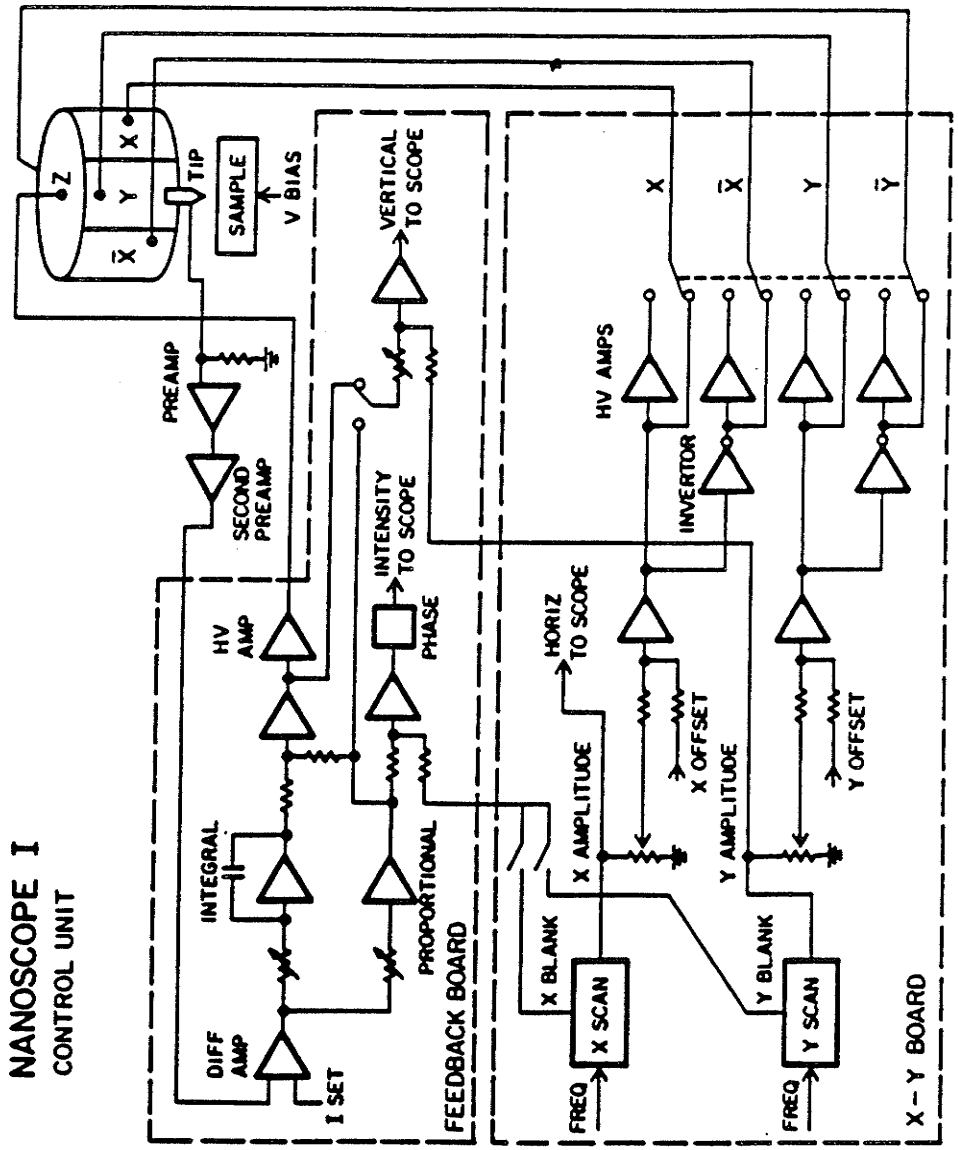

Figure 2.2: NanoScope I Control Unit (from [64])

control voltage. When this voltage increases (tip retracting from surface), the beam becomes more intense. Conversely, when the z voltage decreases (tip approaching the surface), the beam intensity lessens. Consequently, the image appears as if an observer viewed the surface from its zenith, with brighter areas corresponding to higher points on the surface.

The second type can be considered a line scan image. The vertical motion of the scope trace is controlled by both the y and z signals described above. Because of this, the trace will vary around a horizontal line as it moves across the screen. When this motion is coupled with the modulation of the beam intensity, relief appears in the image. This perspective is enhanced by a Digital Instruments proprietary technique called Dynamic Shading^{TM}. This technique gives the observer a sense that the surface is illuminated from an angle, enhancing the topography with a false shadow.

Additional information on most aspects of the operation and description of the NanoScope I can be found in the unit's manual[64].

2.1.4 Computer Interface

The oscilloscope display is useful for a quick evaluation of both the current performance of the STM and the topography of the surface. However, it is quite limited for image storage (photographs of the screen are the only means for saving a displayed image), and useless for image manipulation. To provide for these capabilities, the control unit was connected to a personal computer. An interface board providing A/D, D/A and digital I/O capabilities was used to provide the connection. The board is a model DASH16 manufactured by Metrabyte of Taunton, Massachusetts. A Turbo Pascal computer program was developed to provide handling of the board's information, and to provide for the display, manipulation and archiving of the resulting image and associated image parameters.

To perform nanolithography experiments, the ability to apply a voltage pulse to the tip while it scanned the surface was needed. The NanoScope I control unit provides for the application of an external bias voltage. This feature was used along

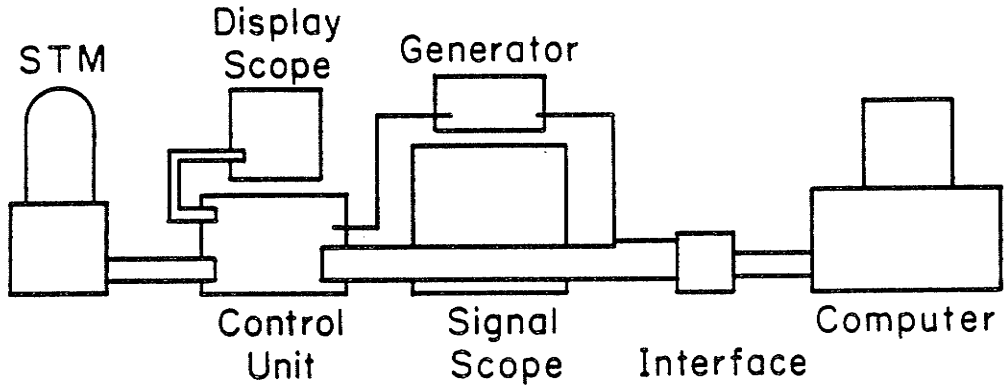

Figure 2.3: Component Interconnection

with a simple bias circuit and a pulse generator to provide for the application of the pulse. Figure 2.3 shows the interconnections of the different components used in the nanolithography experiments described in this thesis. The second storage oscilloscope was used to monitor the z piezo voltage and tunneling current during the pulse. The pulse generator and second scope were both triggered by the computer. The trigger was programmed to occur when the microscope scan reached its center. The pulse generator used initially was a Hewlett-Packard model 214A. It was later replaced by an HP model 8011A. The second storage scope initially was a Tektronix model 7613. It was later replaced with a Tektronix model 2221.

A schematic of the electrical circuit used for application of the voltage pulses is shown in figure 2.4. The bias circuit is an adjustable resistor divider allowing a bias voltage range of 10mV to approximately 2.2V. The output of the pulse generator is added to the external bias voltage through a capacitor. The purpose of the capacitor is twofold. It ensures that the pulse generator does not short the bias circuit and it acts as a high pass filter. The HP 214A pulse generator had a 60Hz noise signal present on its output, which would modulate the bias voltage, and hence the tunnel current, if the capacitor was not present. This noise does not appear at the output of the 8011A, but the capacitor is still needed to avoid shorting the bias.

The impedance of the external bias input on the control unit was specified to

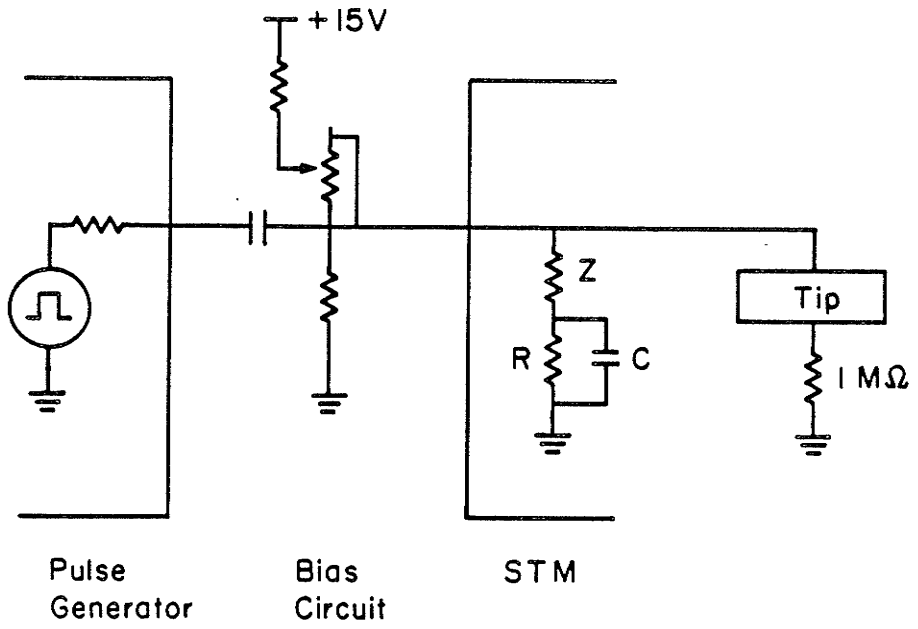

Figure 2.4: Voltage pulse circuit

be approximately 100kΩ. However, measurements indicated that it was only about 90Ω. An investigation revealed that the rubber driveshaft connecting the stepper motor to its screw was a conductor; it was shorting the specified input impedance. This driveshaft impedance is labelled Z in figure 2.4. To alleviate this problem, a resistor, labelled R, was introduced between the driveshaft impedance and ground. The value of this resistance was 22kΩ. After this resistance was introduced, the pulse measured at the sample stage exhibited considerable ringing. To reduce this, a capacitor, labelled C, was placed into the circuit. This resulted in the pulse shown in figure 2.5. Later, a mechanical problem related to the performance of the rubber driveshaft resulted in its replacement with a Teflon sleeve. This sleeve does not conduct. Because of this, the pulse once again exhibited ringing. To lessen this ringing, a 100Ω resistor was placed in parallel with the sleeve. This became the new Z in figure 2.4. These changes resulted in the pulse shown in figure 2.6.

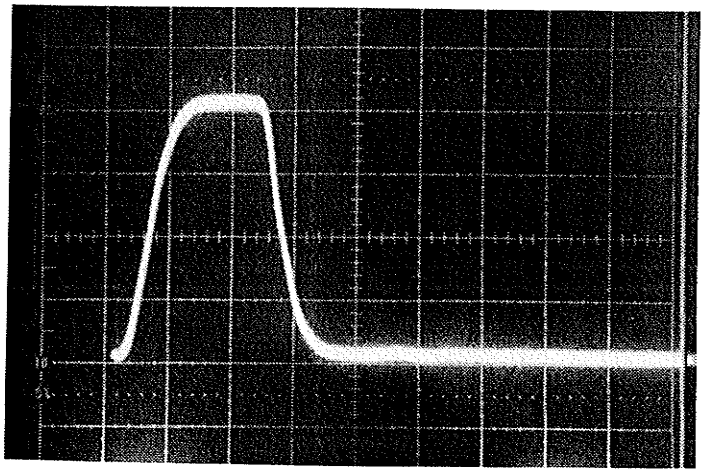

Figure 2.5: Pulse at head with rubber driveshaft. Scale factors are 1V/div vertically and 100ns/div horizontally.

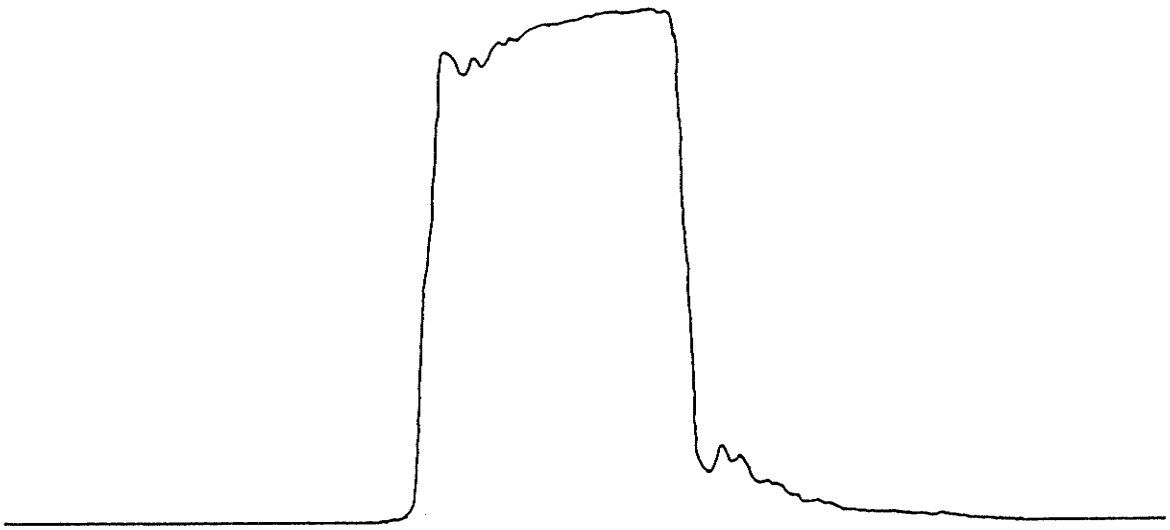

Figure 2.6: Pulse at head with Teflon sleeve driveshaft. Pulse is 6.5V in amplitude and 200ns in duration.

2.2 Tip Considerations

As described in section 1.3 and shown in figure 1.2, the phenomenal resolution of the STM is the result of tunneling to near monatomic tips. While the tip gives the instrument its unique probing ability, problems associated with it can result in puzzling instrument performance, such as the anomalous corrugation amplitudes detailed in section 1.5. In addition, unexpected or confusing images can also be traced to problems with the tip. Most of these unusual images are believed to be caused by the presence of multiple tips, which is a tip consisting of two or more protuberances to or from which electrons simultaneously tunnel.

Park et al.[65] obtained anomalous images of Si(111) which could be explained by the superposition of two images formed by simultaneous tunneling to two different tip atoms. In addition, their images provide evidence that these two different tunneling sites could be widely separated.

Mizes et al.[66] performed an analysis which showed that the experimental images of HOPG and similar layered materials are dominated by only three Fourier components. Significant aberrations in the image will result if the amplitudes or phases of these components are changed. Multiple tips images can cause these changes. The researchers created a number of computer generated images by changing the relative values of the three components. These computer generated images correspond well with confusing experimental images. Colton et al.[67] also numerically generated images. Their simulations assumed trigonally symmetric and asymmetric tip configurations; like Mizes et al. the resulting images correspond well with experimental ones. They also note that multiple tips could be responsible for the aberrant images.

Albrecht et al.[68] explored tilt boundaries on HOPG. They found that images with moiré patterns would sometimes occur near these boundaries. By superimposing two images taken at significant distances on opposite sides of the boundary, the moiré patterns could be duplicated. Because of this, they believe that multiple tips must image either side of the boundary simultaneously.

Because the STM owes its unique abilities to its tip, and because significant image problems may result from poorly characterized tips, a method for reliably producing

monatomic tips is needed. Numerous techniques exist which may be capable of fulfilling this need. Each has drawbacks and desirable features.

2.3 Tip Preparations

Three different methods of producing tips are generally used in STM. The first is simple physical or mechanical manipulation of the wire from which the tip is formed. Cutting, breaking or grinding of the wire has produced tips which have yielded atomically resolved images. For example, Colton et al.[69] used the ends of broken graphite pencil leads as tips and obtained images of HOPG. They believe that "whiskers" of graphite remain on the end after breaking the lead; tunneling takes place to one of these "whiskers." Grinding and cutting is also believed to leave these asperities.

Most tip preparation methods have their roots in the field of Field Ion Microscopy (FIM). The Field Ion Microscope, invented in the 1950's, is an instrument capable of producing images of tips with atomic resolution. In this device, a high voltage is applied to a tip which had been placed into an evacuated chamber. An imaging gas (typically He) is introduced into this chamber. Ionization of the gas occurs immediately above atoms on the tip surface which have enhanced the local electric field. These gas ions are accelerated along the field lines to a fluorescent screen where an image of the tip is formed. The magnification of the image is dependent upon the tip radius and distance between tip and screen; typical magnifications are on the order of 10^7. So, as in STM, resolution in FIM depends upon sharp tips. Much effort was spent in devising reliable tip preparation methods. The method of choice was electrochemical etching, which has been adopted by the STM community.

In an electrochemical etch, a portion of the tip wire is suspended below the surface of an aqueous etchant solution. A second electrode is also suspended within the solution. A voltage is then applied between these two electrodes. The resulting current flow causes an electrochemical attack of the wire. Heben et al.[70] found that the etch exhibits two distinct patterns of behaviour. At first, the diameter of the wire is reduced uniformly, while the length remains unchanged. At some point, this

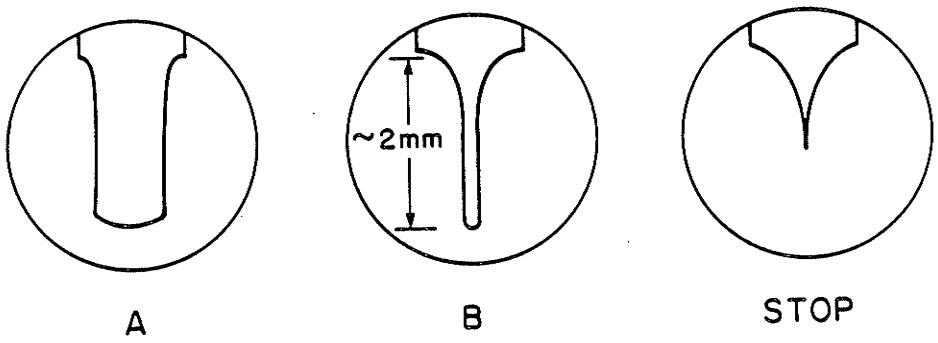

Figure 2.7: Tip changes during electrochemical etching. In A, the diameter reduces uniformly. In B, the length of the tip is reduced. At Stop, a sharp, well-supported tip has been formed (from[70]).

behaviour ceases and the length of the wire is decreased, with little or no further decrease in diameter. Figure 2.7 illustrates this process. They found that the etching should be halted just before the current dropped to zero in order to obtain a near-monatomic tip. To halt the etch, they monitor the current, which also exhibits a characteristic behaviour as the etching proceeds. Figure 2.8 shows a typical plot of etch current versus time.

Heben et al. used PtIr wire etched in a solution of NaCN and KOH. The voltage was $25V_{ac}$. The solution used will depend upon the kind of wire to be etched. In addition, ac or dc voltages can be used. Because many of the solutions and electrical parameters, as well as the choice of material for the second electrode, were originally developed for FIM, its literature[71]- [73] contains information about electrochemical etching. In addition, researchers active in STM have published numerous papers on the subject. A variation on the standard electrochemical etch is described by Bryant et al.[74]. Nicolaides et al.[75] examined etched W tips. They observed bending when the length of wire immersed into the solution is large. They believe that the mass of this immersed wire at some time during the etch exceeds its strength. This causes plastic flow during the etch and some recoil when the wire breaks. However, they were still able to produce images with these bent tips.

Tips produced by electrochemical etching have successfully produced atomically

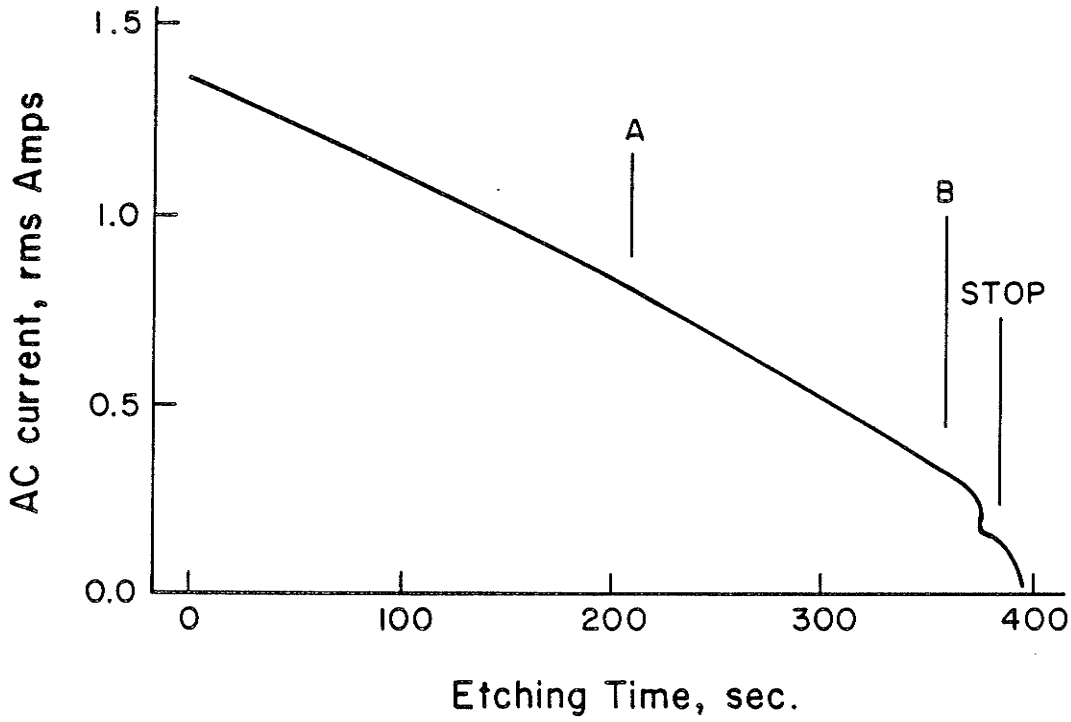

Figure 2.8: Typical current vs. time etch characteristic. Labels A, B and STOP correspond to tip views in figure 2.7 (also from[70]).

resolved images without any further processing steps. However, to avoid the contamination problems described in section 1.5, some reseachers have attempted to clean the tip by ion milling. In this technique, a beam of ions, typically Ar^+, is directed at the tip. This removes any residue left from the etching process, as well as any oxidation. However, Biegelsen et al.[76] has discovered that ion milling tends to preferentially thin tips formed from polycrystalline W wire. This could lead to an undesirable whipping action of the tip during operation of the STM. However, they found that ion milling with single crystal W<111> wire does not lead to the same problem[77]. Tiedje et al.[78] also explored cleaning with ion milling. They could not produce an image possessing atomic resolution with a tip which had been ion milled at near normal incidence. However, tips which were simultaneously ion bombarded and sputter coated did yield the desired images.

Several groups have used a phenomenon associated with FIM called field evaporation to enhance electrochemically etched tips. At sufficiently high field strength, tip surface atoms will evaporate. Field enhancements caused by protruding surface atoms reduce the activation energy necessary for evaporation, so these protrusions are evaporated preferentially from the surface. This results in a tip with a smooth hemispherical cap, similar to that originally envisioned by Binning and Rohrer. The ideal tip would consist of a field evaporated tip with just one atom adsorbed on it. Fink has produced such a tip[79]. He begins by field evaporating the tip until the apex plane consists of a trimer. Then, the tip is bombarded with Ne ions to minimize the area of the layers supporting the trimer, in effect to sharpen the tip. Following this, an atom is deposited onto the top of the trimer from the gas phase, yielding a single atom at the apex of the tip.

Binh et al.[80, 81] have also attempted to create monatomic tips *in vacuo*, using a combination of electric field and heat. In their "build-up" technique, a local rearrangement of atoms by surface diffusion is preferentially encouraged by a high field. This results in an enlargement of low index planes; a single atom tip will result when two planes collide at the apex. In the pseudo-stationary profile (PSP) technique, surface diffusion and evaporation or corrosion will act to produce the desired monatomic tip. Nedermeyer and Drechsler have used similar combinations of electric field and heat to produce tips by the "build-up" technique[82].

2.4 Tips Used

The tips used for the experiments described in this thesis were either polycrystalline W or PtIr (80/20). The PtIr tips are commercially available from Digital Instruments. These tips have been mechanically formed. On occasions, some of these PtIr tips became damaged; they could be rehabilitated simply by cutting with a pair of tin snips or side cutters. The W tips were electrochemically etched in an aqueous solution of KOH (10 gm per 140 ml of distilled H_2O). A variety of ac voltages, ranging from 7 to 25V, were used. The range of typical currents measured at the start of the etch was 250mA to 2A. Behaviour similar to that observed by Heben et al. and illustrated in figure 2.8 was seen, although no similar attempts to control the stop of the etch were made. Some of these etched tips were ion milled in a 5 keV Ar^+ ion beam with milling durations ranging from 2 to 10 minutes. Measured beam current was 50μA. Most etched, and etched and ion milled W tips yielded atomic resolution images of HOPG readily.

Chapter 3

Pinning Mechanisms

3.1 Introduction

As mentioned in section 1.8, the STM offers the possibility of manipulating matter on an atomic scale. This ability, when applied to nanolithography, may result in microelectronic circuits with a higher level of integration than those currently in existence. The use of an STM for such an application was investigated; this investigation is described here. Nanometer-sized structures were formed on graphite surfaces by the application of voltage pulses to the tunneling tip. This work pursues a line of study initiated by Foster et al.[61].

3.2 Background

The work of Foster et al. was described briefly in section 1.8. Because it provided some of the motivation for the investigation described presently, a more detailed description may prove beneficial.

Foster et al. attempted to "pin" or attach all or a portion of a molecule to a graphite surface by applying a submicrosecond voltage pulse to the tip as it scanned the surface. The STM of Foster et al. operated in the constant current mode. The

tip used was formed out of tungsten by an electrochemical etch. Prior to the commencement of these experiments, the surface was covered with a drop of an organic liquid, which was to act as the source for the pinned molecules. Many organic liquids were described as being amenable to this process, but only dimethyl phthalate and di(2-ethylhexyl) phthalate are specifically mentioned. A typical bias voltage was 30mV, with nominal currents ranging from 0.1 to 1.0nA. The amplitude of the pulse ranged from 2.0 to 4.3V, with a duration of 100ns. The pulse was triggered when the tip reached the center of the scanned area; the pinned feature or "hillock" appeared immediately following the pulse.

The hillocks created by the pulse contained no features which could uniquely identify their origin. However, the size of the hillocks was consistent with the dimensions of the organic liquid molecules deposited onto the surface at the start of the experiment.

By the repeated application of pulses with different amplitudes, a threshold of approximately 3.5V was discovered for the successful generation of hillocks. This threshold was not dependent upon the polarity of the tip voltage, nor did it depend upon the tunneling current value. In addition, the appearance of the hillock was not altered with changes in the polarity of the bias voltage nor with changes in the tunneling current value.

Foster et al. also discovered that the pinned structure could be partially modified or completely erased by another pulse. An erasure threshold roughly equivalent to the pinning threshold was also found. Through a process of pinning and partial erasure, the researchers were able to reproducibly form a hillock with a diameter of approximately 4Å.

Foster et al. suggested that the hillocks were formed when sufficiently energetic tunneling electrons activated adsorbed organic molecules or the surface, or both, resulting in attractive forces between the surface and the molecules. They also point out that some other mechanism, such as material transfer between tip and surface may be responsible for the formation of the hillocks.

3.3 Experimental Details

The experiments described here were performed in the same manner as those of Foster et al. A voltage pulse was applied to the tip as it scanned the surface. An organic liquid was introduced onto the surface prior to the start of the experiment; as a result, both the surface and the tip were immersed in the liquid.

Section 2.1.4 contains a description of the apparatus used for the pinning experiments. The pinning pulse was triggered by the computer, and coincided with the center of the scan. The amplitude and duration of the pulse was manually adjustable.

The conditions and procedures used during the experiments evolved as more experience and insight into the deposition process was gained. The experiments can be chronologically divided into three distinct studies. For clarity, each is described separately.

3.4 First Study

3.4.1 Experimental Details

During the first study, the only result monitored was the occurrence of a hillock following a voltage pulse. The bias conditions used are shown in table 3.1. For a tip free of contamination problems, the tip-to-surface separation was estimated to change by 6 to 9Å as the bias conditions change from set #1 to #6. The liquid present on the surface was either decane (n-$C_{10}H_{22}$) or dimethyl phthalate. The tips used were predominantly etched W; however, cold-worked PtIr and W tips were also tried. Some of the tips were ion-milled.

Later, with the same bias conditions described in table 3.1, different pulse durations were also investigated. The durations used were 0.2, 0.4, 1.0 and 2.0μs.

Set #	bias (mV)	current (nA)
1	20	2
2	20	1
3	20	0.5
4	40	0.5
5	80	0.5
6	160	0.5

Table 3.1: Bias conditions used during first study

3.4.2 Results

Like Foster et al., a voltage threshold of between 3.5 to 4.0V was found. However, even with a pulse amplitude exceeding 4.0V, the probability of forming a hillock ranged only from 0.45 to 0.7. Foster et al. found a probability approaching 1.0 for voltages above the threshold. No dependence on bias conditions, liquid, tip type or manufacture, nor pulse duration could be established.

A number of interesting observations about the hillocks were made. The hillocks were scattered throughout the field-of-view (FOV), which typically ranged in value from 60Å by 80Å to 120Å by 125Å. Generally, more then one hillock appeared per pulse. Like Foster et al., no identifiable features were discernable in the hillocks. The probability of a hillock appearing at the center of the FOV (that is, immediately under the tip when the pulse occurred) was no different than that for a hillock appearing off to a side. On occasion, the entire FOV would become filled with what was initially interpreted as a huge hillock. Following this, a clean portion of the graphite could not be located by moving the position of the FOV, which was accomplished by applying dc voltages to the x and y piezo's. Instead, the experiment would have to be halted momentarily to allow for the relocation of the graphite sample.

Towards the end of this study, the discovery was made that hillocks could be produced with no liquid present (ie. in an air ambient). In addition, the huge hillocks

mentioned previously were found to be part of a crater-like structure formed evidently as a result of a voltage pulse.

3.5 Second Study

3.5.1 Experimental Details

Following the discovery of the craters and air-ambient hillocks, there was concern that during some pulses, the tip would contact the surface (thereby producing a crater) and remove material which would be deposited back onto the surface during later pulses (producing hillocks). In an effort to determine if this was happening, the pinning experiments were repeated. However, during this study, the tunneling current and z piezo voltage during and immediately after the voltage pulse were recorded along with the incidence of hillocks. This was done in an effort to correlate the behaviour of the tip with the appearance of craters and hillocks.

The bias conditions used are shown in table 3.2. Both air and liquid ambients were used. The liquid was either an n-alkane (decane (n-$C_{10}H_{22}$), hexadecane (n-$C_{16}H_{34}$) or heptadecane(n-$C_{17}H_{36}$)) or dimethyl phthalate. Etched W tips along with cold-worked W and PtIr tips were used during this study. Some of the tips were ion-milled. Different pulse durations were also investigated. The ones used were 0.2, 0.4, 1.0, 2.0 and 4.0μs.

3.5.2 Results

Table 3.3 shows the probability of producing a hillock in an n-alkane or air ambient. The values given in the column labelled probability reflect the number of pulses which created some structures versus the total number of pinning pulses applied to the tip. Table 3.4 shows the probability of producing a hillock in an air ambient for different tip types and manufacture, while table 3.5 shows the same probability for different pulse widths. These tables are representative of the results obtained during

bias (mV)	current (nA)
80	0.3
500	0.5
200	0.5
80	0.5
500	1.0
200	1.0
50	1.0

Table 3.2: Bias conditions used during second study

Ambient	Pulse height (V)	probability
alkane	3→3.5	3/68 = 0.04
	4→4.5	31/53 = 0.58
air	3→3.5	7/216 = 0.03
	4→4.5	65/130 = 0.5

Table 3.3: Probability of producing hillocks in n-alkane or air ambients

this second study; however, some experimental attempts are not categorized in these tables.

The most significant result can be seen in table 3.3. A voltage threshold of between 3 and 4 volts exists for the production of hillocks in an organic liquid *and in air*. This suggests that even in a liquid ambient, some hillocks may be formed by a mechanism which does not involve the liquid.

The probability of hillock formation exhibited no clear dependence upon bias conditions. The results displayed in table 3.4 suggest that a PtIr tip may be less likely to form a hillock in air than a W tip. Besides this, as indicated in table 3.5, no clear dependence exists relating the probability of hillock production to pulse duration. More exhaustive trials are needed to prove both trends conclusively. Irregardless, no

Tip	Pulse height (V)	probability
etched W	3→3.5	8/112 = 0.07
	4→4.5	31/45 = 0.69
cold-worked W	3→3.5	1/52 = 0.02
	4→4.5	27/40 = 0.68
PtIr	3→3.5	1/80 = 0.01
	4→4.5	21/60 = 0.35

Table 3.4: Hillock production probability for different tip types in an air ambient

Tip	Pulse height (V)	Pulse duration (ns)	probability
PtIr	3→3.5	200	1/23 = 0.04
		1000	0/21 = 0.0
	4→4.5	200	17/41 = 0.41
		1000	2/11 = 0.18
W	3→3.5	200	1/30 = 0.03
		2000	12/59 = 0.20
	4→4.5	200	13/22 = 0.59
		2000	15/19 = 0.79

Table 3.5: Hillock production probability versus pulse duration

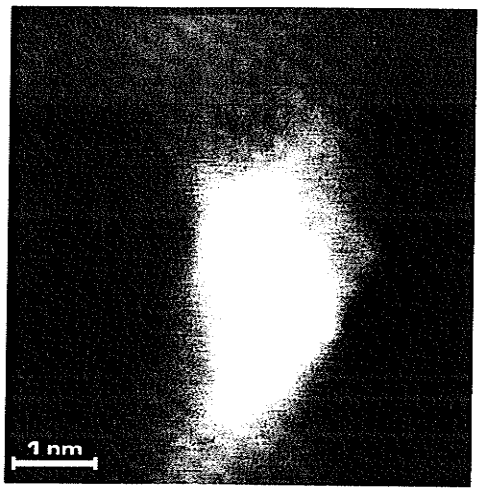

Figure 3.1: Hillock formed in air. Bias condition was 80mV and 0.5nA. Pinning pulse was 4V and 200ns. Tip was cold-worked PtIr. Feature dimensions are 17 by 25Å, with a height of approximately 5Å.

set of conditions could be discovered which inhibited the formation of hillocks in an air ambient.

Like the hillocks produced by Foster et al., and those made during the first study, the hillocks produced during this second study also contained no identifiable features nor any discernable molecular or atomic structure. Examples of the hillocks formed are shown in figures 3.1 to 3.3[83]. The size of the hillocks varied from 100Å^2 to 10000Å^2.

The lifetime of the hillocks (ie. the duration of time during which a hillock could be continuously observed) also varied greatly, and did not depend on tip type nor ambient. Some hillocks remained in the FOV for long periods, typically more than 5 minutes. Because of thermal drift, these hillocks would slowly move out of the FOV. Occasionally, these longer-lived hillocks would fade and disappear before drifting completely from the FOV. Some of these long-lived hillocks were erased by increasing the tunneling current. Very short-lived hillocks were also seen. Some abruptly vanished before the computer could acquire their image (ie. immediately following the scan which produced them). Others vanished during the first few scans following their manufacture. A typical abruptly vanishing hillock is shown in figure 3.4.

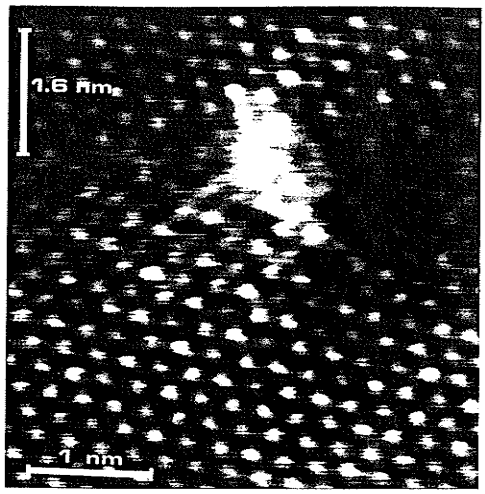

Figure 3.2: Hillock formed in dimethyl phthalate. Bias condition was 80mV and 0.3nA. The pulse was 4V and 400ns. Tip was etched, ion-milled W. Feature dimensions are 9 by 21Å, with a height of 8Å.

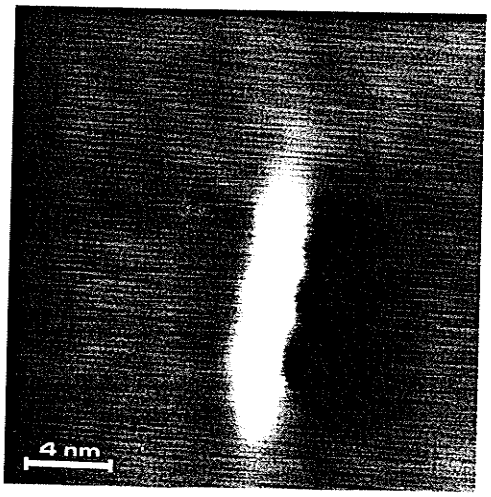

Figure 3.3: Large hillock formed in decane. Bias condition was 160mV and 0.5nA. Pinning pulse was 4V and 1μs. Tip was cold-worked W. Feature dimensions are 17 by 102Å, with a height of 6.5Å.

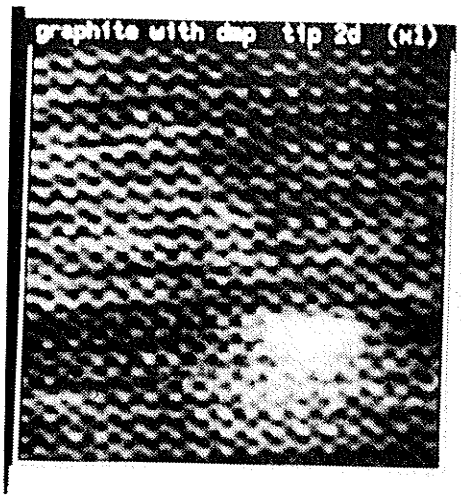

Figure 3.4: Cutoff hillock formed in dimethyl phthalate. Bias condition was 80mV and 0.3nA. The pulse was 4V and 2μs. Tip was etched, ion-milled W.

The hillock appears to be cutoff; no evidence of this hillock remained on subsequent scans. This suggests that the point of tunneling has changed to another location on the graphite away from the original hillock, or that the hillock has spontaneously left the surface. Several other structures similar to the cutoff hillock in figure 3.4 were observed during the second study.

As mentioned previously, at the end of the first study craters were discovered following some pinning pulses. An example is seen in figure 3.5. The experiments performed during this study showed that crater formation is rare compared to hillock formation. In addition, a tip which formed one crater was more likely to form additional craters on successive pulses. This suggests that the tip is modified substantially during the formation of the crater. The discovery of the craters initially caused concern that the tip was actually contacting the surface during the pulse, thereby forming the crater, and also modifying itself. The decision to monitor the tunneling current and z piezo voltage was motivated in part by the need to ascertain if this was happening.

Measurements of the tunneling current and z piezo voltage during and immediately after the voltage pulse yielded important clues regarding the formation of the hillocks and craters. Changes in the z piezo voltage indicate changes in the

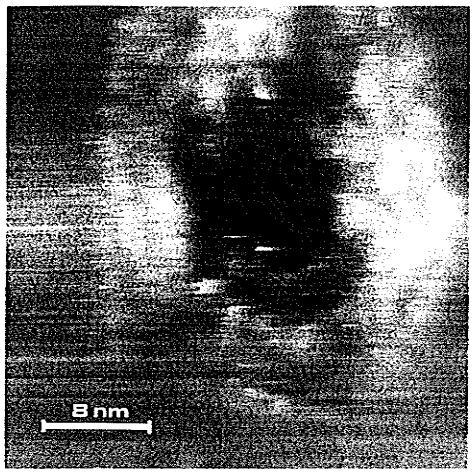

Figure 3.5: Crater formed during a pinning pulse. Bias condition was 160mV and 0.5nA. Pulse was 4.5V, 200ns. Tip was cold-worked PtIr. Decane was present on the surface. The depth is about 80Å.

steady-state tip position. Such changes result from tip modification. Typical storage oscilloscope traces of tip position and tunneling current, made during the second study, are shown in figure 3.6. A vertical dashed line indicates the occurrence of the voltage pulse. On a fast time scale, the traces in figure 3.6(a) were usually seen. Immediately after the pulse, the current begins to rise, with its rise time limited by the slew rate of the current amplifier. The control system responds to the current surge by withdrawing the tip. On a slower time scale, the traces in figure 3.6(b) were typically seen. The initial current spike is not visible on this time scale. The control system responds to the current surge by withdrawing the tip; this causes the current to drop to zero. Consequently, the control system ramps the tip back towards the surface, stopping when the current has risen and again matches the setpoint value. As there is no net change in z voltage, the steady-state position of the tip did not change as a result of the pulse. This behaviour was observed most often during the second study. Hillocks would sometimes appear following traces of this kind.

Occasionally, traces typified by figures 3.6(c) and (d) were seen. Figure 3.6(c) is similar to (b) except that the steady-state tip position following the pulse is significantly closer to the surface. The surface generally remains unchanged; however,

a hillock may occasionally be formed. Figure 3.6(d) is also similar to (b) except that the final tip position is further from the surface following the pulse. When a crater was formed, traces of this kind were always observed. This is attributed to the transfer of material from the surface to the tip; this may explain why successive pulses also cause the formation of craters. Note however that traces exemplified by figure 3.6(d) also occurred without a crater appearing.

3.5.3 Discussion

In air, a likely mechanism for hillock formation is the transfer of material from the tip to the surface. The traces in figure 3.6(c) suggest that material was removed from the tip at the point of tunneling, while those in (b) indicate that the tip material came from a location on the tip which was not involved in tunneling.

The oscilloscope traces shown in figure 3.6 were obtained while the tip was operating in air. Similar traces were obtained when the tip operated in a liquid. This fact, combined with the similar voltage thresholds required for hillock formation, suggests that the same mechanism (material transfer) may be responsible for the formation of hillocks in air *and in liquid.* However, conclusive evidence of this was not discovered during the second study.

Conclusive evidence was obtained to disprove the speculation that the tip was physically contacting the surface during a pulse and forming a crater. If this was happening, a momentary increase in the z piezo trace should occur as the tip is pushed into the surface. This behaviour was not observed during the second study. Instead, during crater formation, the tip was always retracted away from the surface, both during and after the pulse, as seen in figure 3.6(d). The work of Albrecht et al.[60], which was described in section 1.8, supports this finding. Their research suggests that the craters are produced by an electrochemical reaction rather than by physical contact by the tip.

The cutoff hillocks seen during this study provide additional evidence supporting the material transfer concept. As described previously, one possible explanation for this behaviour is the change of the point of tunneling from one location to another.

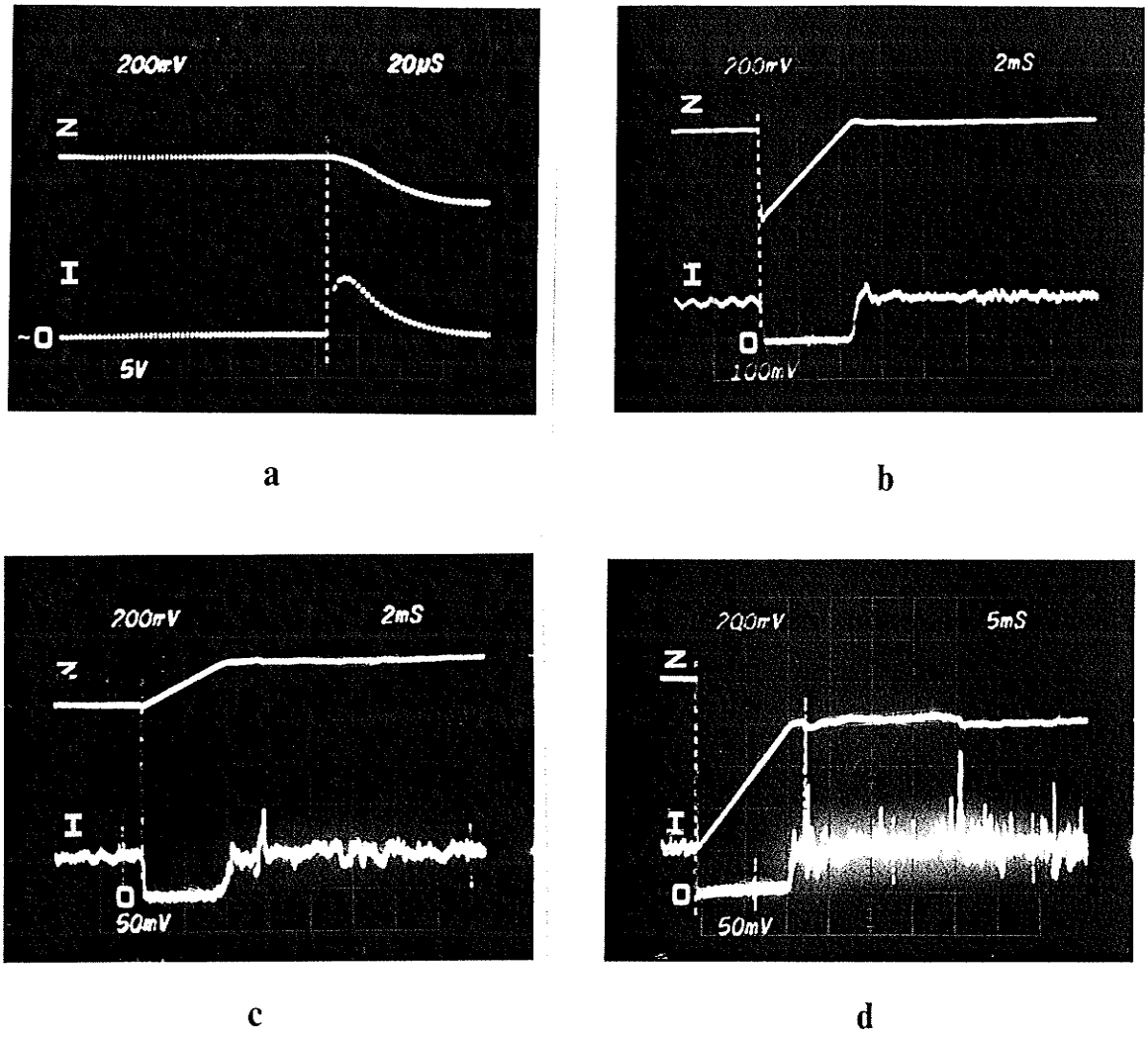

Figure 3.6: Vertical piezoelectric drive voltage z and tunneling current I recorded during pinning pulses. 200mV on z corresponds to 52Å, while 100mV on I is 1nA. Increasing the z voltage moves the tip towards the surface. The pulse occurred at the vertical dashed line. In (a), I rose at the pulse and peaked at 70nA, causing a tip withdrawal of 50Å. In (b), in response to the current surge, the control system withdrew the tip by more than 100Å causing I to drop to 0. The tip was then returned to its pre-pulse position. In (c), the piezo moved the tip approximately 50Å closer to the surface following the pulse. As the current remains constant a corresponding amount of tip material must have been removed by the pulse. In (d), the tip was withdrawn by the piezo about 50Å further from the surface following the pulse implying that the tip must have increased in length by 50Å. During this pulse, a crater similar to that in figure 3.5 was formed (from [83]).

The existence of multiple tunneling tips has been suggested by many STM researchers (see section 2.2). For the tunneling location to change, the separation between the second tip and the surface must diminish below that of the first tip and surface. This can occur either through lengthening of the second tip, or by shortening of the original. In either case, some material has to be transferred to or from the tip.

3.6 Third Study

3.6.1 Experimental Details

During the second study, no set of conditions was discovered which inhibited the formation of hillocks in air. As material transfer between tip and surface is a likely cause for the formation of some hillocks, a third study was initiated to determine a set of conditions which minimized this transfer. As in the second study, changes in the steady-state tip position, as given by fluctuations of the z piezo voltage, were monitored along with the tunneling current. The magnitude of the z piezo fluctuations were used as an indication of the severity of material transfer.

The bias voltages used were 0.1, 0.5, 1 and 2V. The tunneling current was maintained at a constant 0.75nA throughout the third study. The experiments were performed with the scan stopped and the tip stationary above the surface. Only 200ns pulses were used, but the amplitude of the pulses ranged from 1.3 to 4.7V. At least twenty attempts were made at each pulse voltage. All work was performed in air. Cold-worked PtIr and etched W tips were used. However, the type of W used was expanded to include single-crystal (<111> orientation) as well as polycrystalline stock. Biegelsen et al.[77] found that such single-crystal wire etches more uniformly then its polycrystalline counterpart, yielding a more consistent tunneling tip; consequently, some undesirable effects (such as multiple tips) may be avoided through the use of such wire.

The hillock-forming capabilities of single-crystal W tips were also investigated. The bias voltage used during this part of the study was 1.25V with a tunneling current of 0.75nA. All pinning pulses were 200ns in duration. The total voltage during the

pulse was varied from 2.0 to 4.5V. The tip scanned the surface during this part of the third study, and the pulse was triggered by the computer as the center of the scan was reached. Both air and liquid (n-$C_{10}H_{22}$ and n-$C_{16}H_{34}$) ambients were used. As in the second study, both the occurrences of hillocks, as well as the tunneling current and z piezo voltage were monitored.

3.6.2 Results

Static Measurements

Figure 3.7 shows both the average and maximum change in z piezo voltage encountered at each of the four bias voltages for a cold-worked PtIr tip. As material transfer can result in both positive and negative voltage changes, the absolute value was considered. The total tip voltage (sum of bias and pulse voltage) was 3.7V for the results shown in figure 3.7(a), while it was 4.3V in (b). The z piezo voltage activity drops dramatically at the higher bias voltages. Figures 3.8 and 3.9 show the results for polycrystalline and single-crystal W, respectively. As with the PtIr tip, the z voltage activity drops at the higher biases.

During this part of the study, a current spike was noticed even with the tip out of tunneling range. A typical trace of this spike is shown in figure 3.10. This anomaly is attributed to coupling of the voltage pulse to the current measurement circuits, probably by capacitive means. A plot of the natural logarithm of the coupling current versus pulse voltage is shown in figure 3.11. A plot of the natural logarithm of the tunneling current versus total voltage, for each of the four bias voltages, is shown in figure 3.13. An etched polycrystalline W tip yielded this figure; the PtIr and single-crystal W tips gave similar results. The initial behaviour of the four curves, particularly at the higher bias voltages, is similar to figure 3.11. This suggests that the current at the lower pulse voltages is dominated by the coupling current, and that a portion of the total current at the higher pulse voltages is due to it. Figure 3.12 shows this point vividly. The current recorded consists of an initial spike, which equals the coupling current value, followed by some additional activity. The exact reason for this activity is not yet known, but doubtless it is sometimes involved in

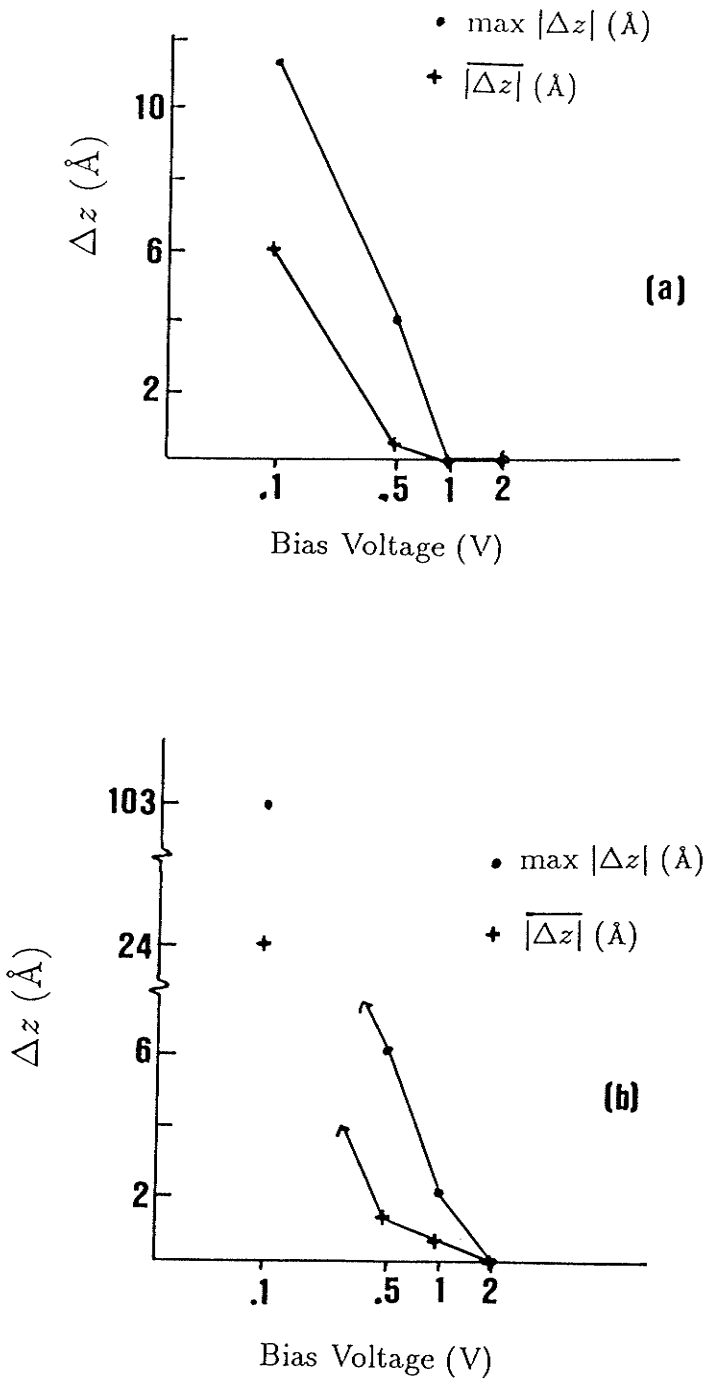

Figure 3.7: Average and maximum values of $|\Delta z|$ for a PtIr tip. Total voltage in (a) was 3.7V, while in (b) it was 4.3V.

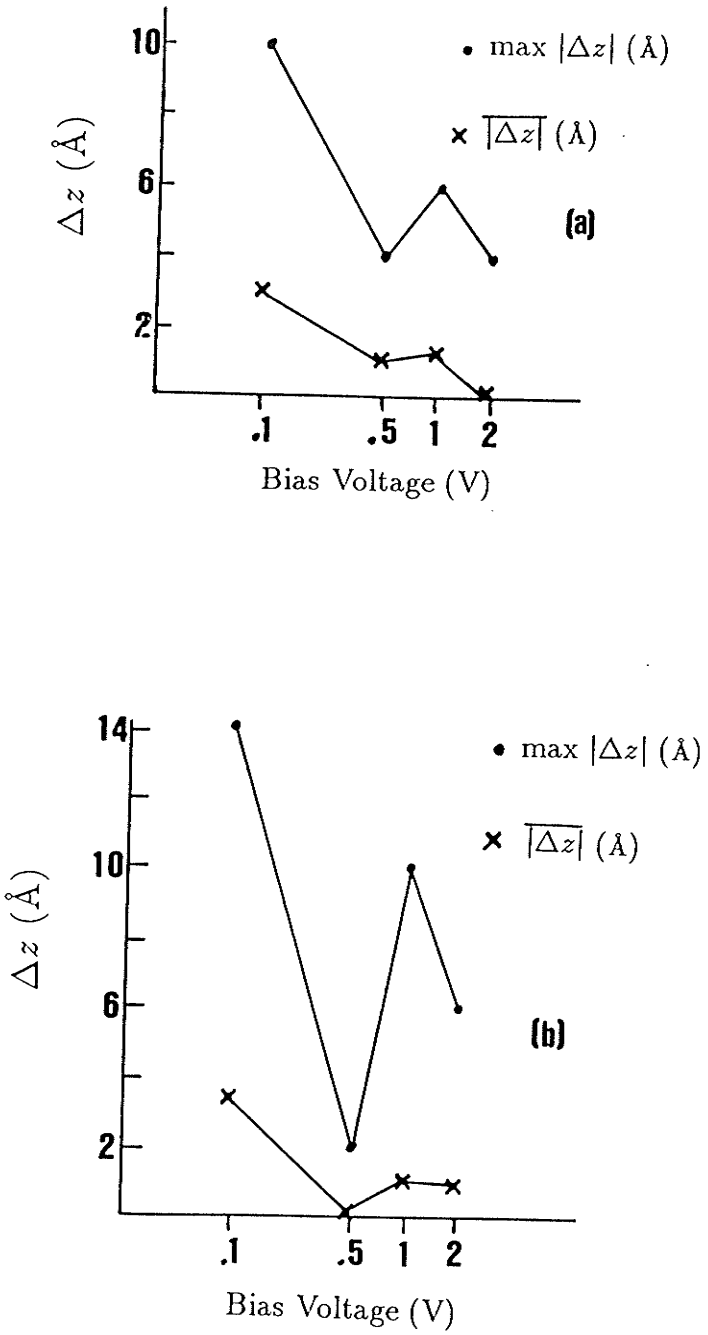

Figure 3.8: Average and maximum values of $|\Delta z|$ for a polycrystalline W tip. Total voltage in (a) was 4.1V, while in (b) it was 4.7V.

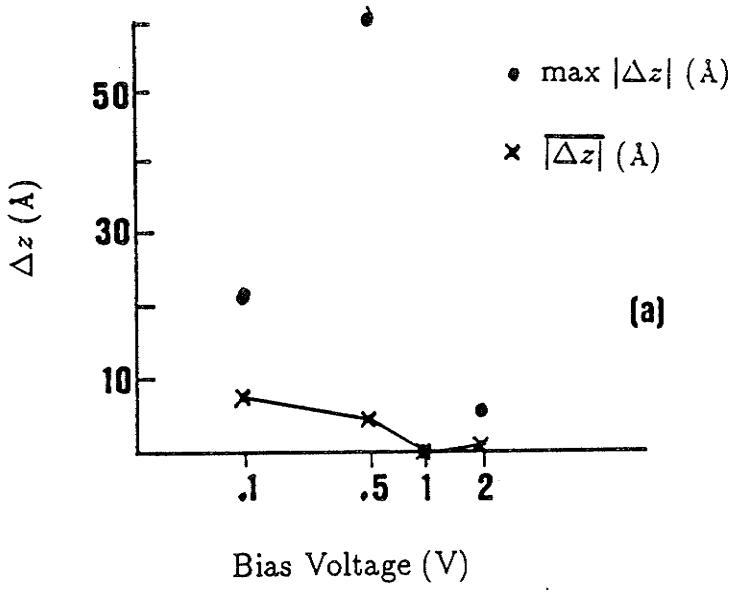

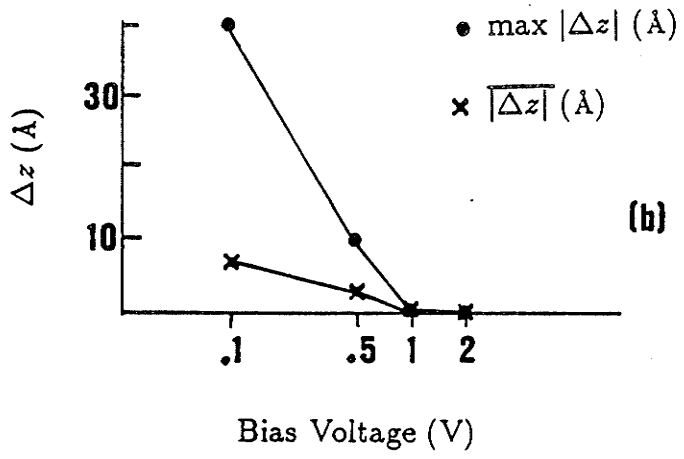

Figure 3.9: Average and maximum values of $|\Delta z|$ for a single-crystal W tip. Total voltage in (a) was 3.6V, while in (b) it was 4.6V.

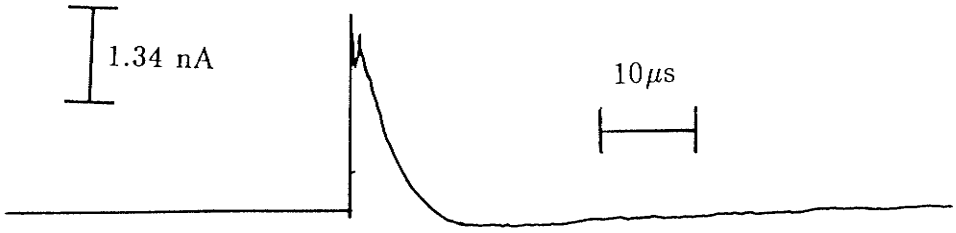

Figure 3.10: Oscilloscope trace recorded during a 2.8V pulse with tip out of tunneling range. The peak value of the coupling current is 2.8nA.

the formation of hillocks.

The tunneling current and z piezo behaviour seen during this part of the study can be categorized into roughly three areas. The first occurs at low pulse voltages (<3V) and is typified by the traces shown in figure 3.14. No z piezo activity is present; the current can be attributed to the coupling phenomenon described above. At higher pulse voltages, traces such as those in figure 3.15 were seen. In 3.15(a), the steady-state tip position does not change, while in (b) it has retracted from the surface by 10Å. Traces were also seen where the steady-state tip position approached the surface. The behaviour of the instrument during the traces was described in section 3.5.2. In general, the amount of initial z piezo retraction was greater at the lower bias voltages. Occasionally, traces such as those in figure 3.16 would occur. The activity is separate from the pulse yet is caused by it. Such activity is not seen unless a pulse occurs. Although not present in this example, the z traces also displayed such activity occasionally. Generally, activity on one trace would be reflected by a reaction in the other.

Single Crystal W Wire

The probability of producing hillocks in an air or n-alkane ambient using an etched single-crystal W tip is shown in table 3.6. These results include all attempts done

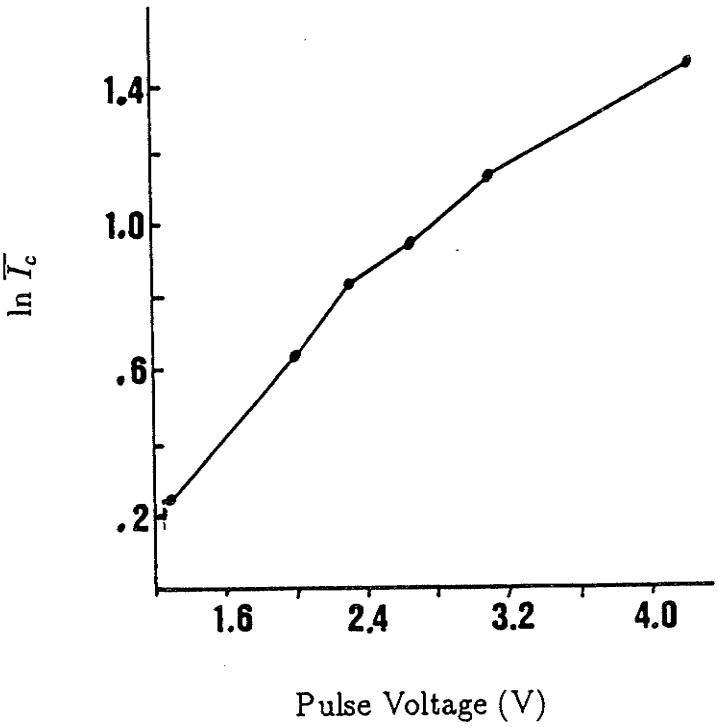

Figure 3.11: Natural logarithm of average coupling current vs. pulse voltage recorded with tip out of tunneling range.

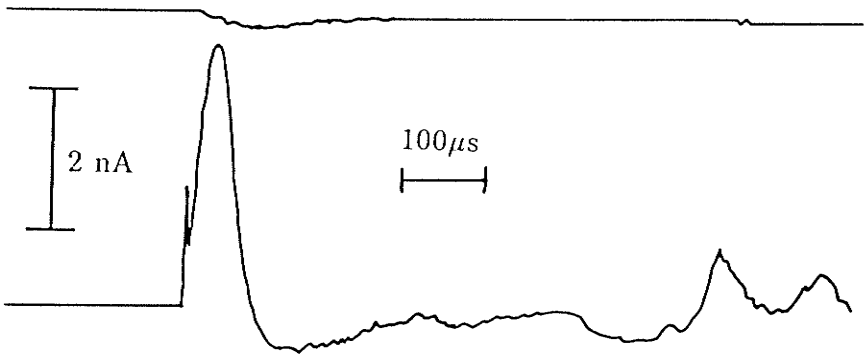

Figure 3.12: Scope trace taken showing initial coupling current followed by activity of unknown origin. Tip was single-crystal W. Bias was 1.25V and 0.75nA. Pulse was 1.6V. Value of coupling current spike is 1.7nA.

during this part of the study. They suggest that hillock formation is more probable in air than in liquid. This is not the case, as hillock production was discovered to be tip dependent. As described previously, during the etching process the single-crystal wire is believed to form more consistent tunneling tips. The stock is also very expensive. Because of this, the tip was etched repeatedly during this part of the study, whenever the image became untolerably noisy or the hillock production probability dropped to zero. After one of these rejuvenation etches, the probability of producing hillocks in either ambient approached one another, as shown in table 3.7. Many of the air attempts used this particular tip, resulting in the skew shown in table 3.6. At times with this tip, a series of twenty or more attempts with the total voltage exceeding 4V yielded pinning probabilities exceeding 0.9.

Eventually, the pinning probability of this tip also diminished to near zero. Another rejuvenation etch restored the production probability to 0.79 (37/47) when the total voltage was above 4V; however, the probability when the total voltage was below 4V increased to 0.25 (18/70).

During these pinning attempts, no clear dependence of hillock formation on peak tunneling current could be found. The z piezo voltage and tunneling current traces

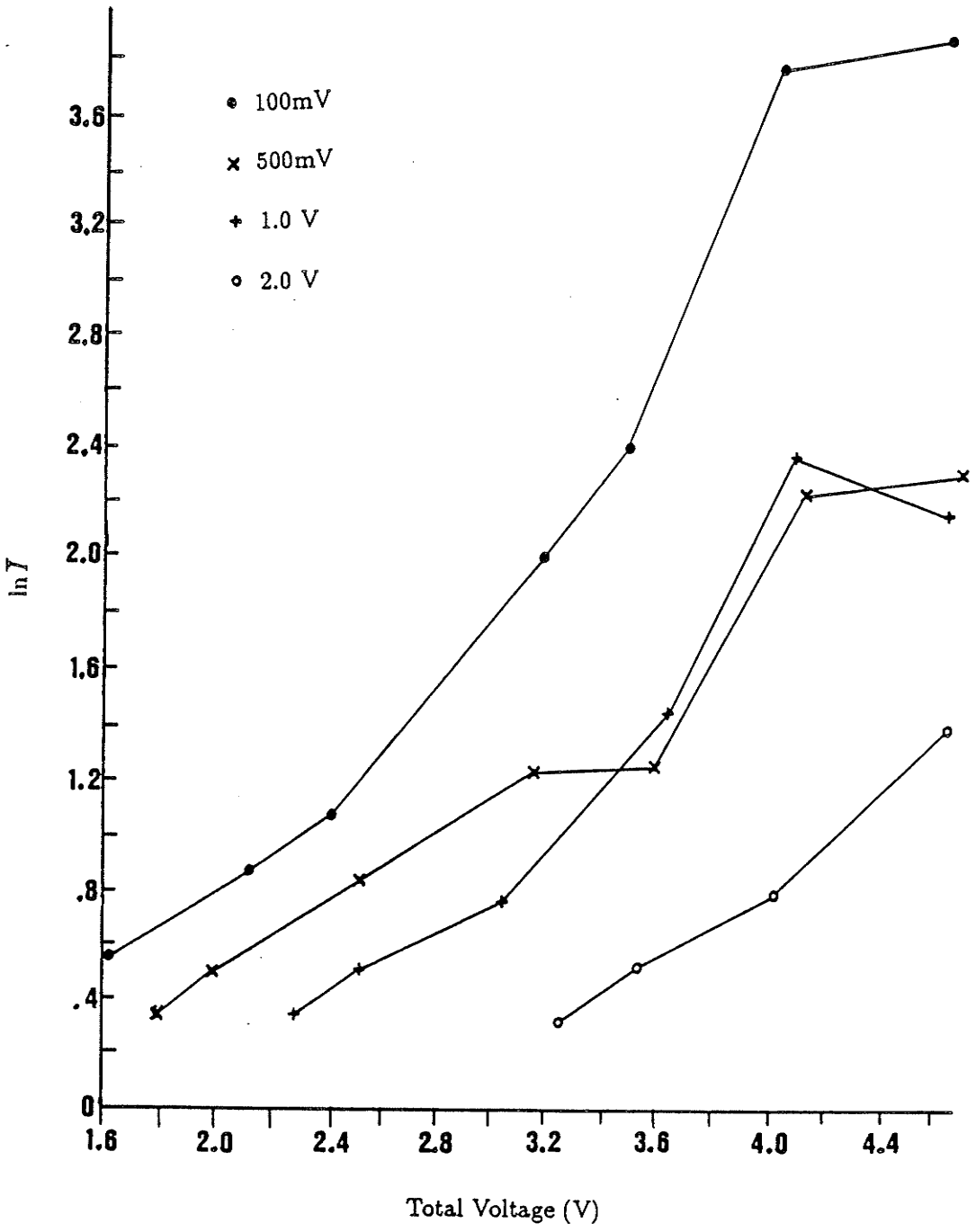

Figure 3.13: Natural logarithm of average tunneling current measured at the four biases using a polycrystalline W tip.

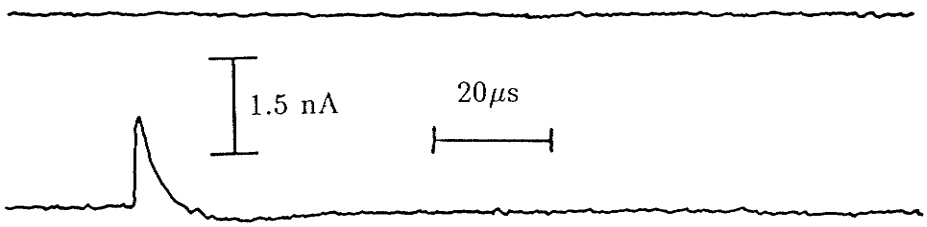

Figure 3.14: Typical z voltage (top trace) and tunneling current (bottom trace) seen at low pulse voltages. The tip was polycrystalline etched W. Bias voltage was 0.5V. Pulse voltage was 1.53V. The peak current (1.5nA) corresponds to the coupling current expected at this pulse voltage.

Ambient	Total Votage (V)	probability
alkane	> 4V	$122/251 = 0.49$
	< 4V	$18/202 = 0.09$
air	> 4V	$89/116 = 0.77$
	< 4V	$22/138 = 0.16$

Table 3.6: Probability of producing hillocks in n-alkane or air ambients

Ambient	Total Votage (V)	probability
alkane	> 4V	$83/105 = 0.79$
	< 4V	$2/31 = 0.06$
air	> 4V	$55/70 = 0.79$
	< 4V	$4/88 = 0.05$

Table 3.7: Hillock production probability in either ambient for a particular tip

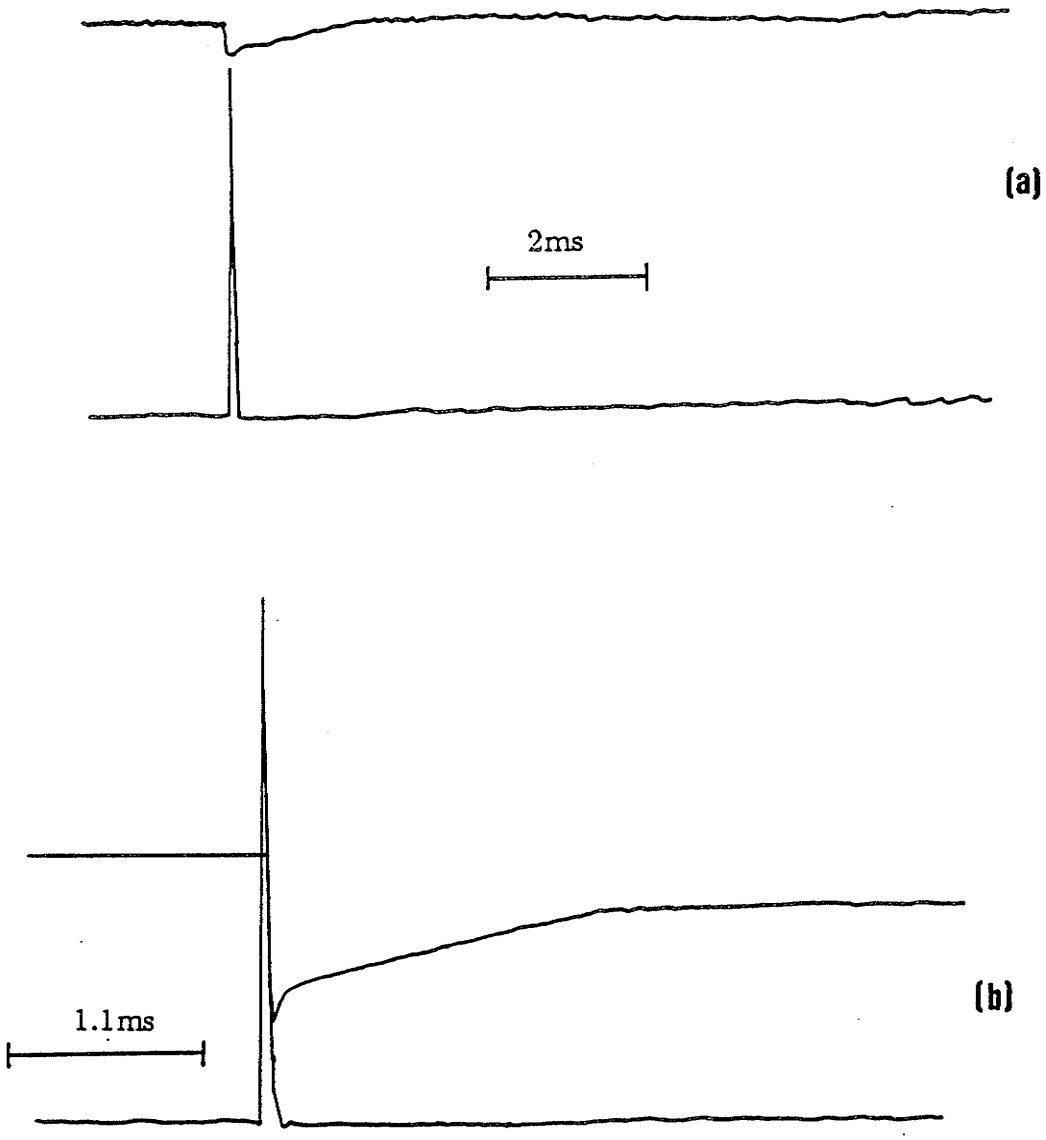

Figure 3.15: Typical traces seen at higher pulse voltages. In (a), the peak current was 33nA, with no change in steady-state tip position. In (b), the peak current was 73nA, with a -10Å change in steady-state position. Tip was polycrystalline W. Bias voltage and pulse voltage was 0.5 and 4V respectively in both cases.

Figure 3.16: Current activity seen following a pulse. Initial spike corresponds to coupling current (3.3 nA). Tip was PtIr biased at 1.1V. Pulse was 3.1V.

exhibited similar behaviour to that described previously for the first part of this study, and for the second study. In addition, tunneling current and z piezo activity similar to that shown in figure 3.16 was occasionally observed during this portion of the third study. The most severe example is shown in figure 3.17. The exact cause of this activity is not known. A hillock was not formed following this trace; however, during other similar events hillocks were observed.

The hillocks themselves were featureless. Their sizes and shapes varied greatly. The lifetimes were the same as those described previously; that is, some vanished abruptly, others drifted from the FOV, while still others faded gradually. One hillock was tracked for approximately 20 minutes, as it drifted and faded. Then, the size increased dramatically, roughly doubling over approximately 30 seconds. It maintained this size as it drifted completely from the FOV, which took an additional 5 minutes.

3.6.3 Discussion

The static measurements indicate that operation at higher bias voltages decreases z piezo activity and therefore material transfer between tip and surface. Consequently, higher bias voltages should be favored in further work. Indeed, the experiments with the single-crystal W tips made use of this discovery. Care must be exercised, however, as operation at bias voltages above approximately 1.5V leads to noisy imaging and

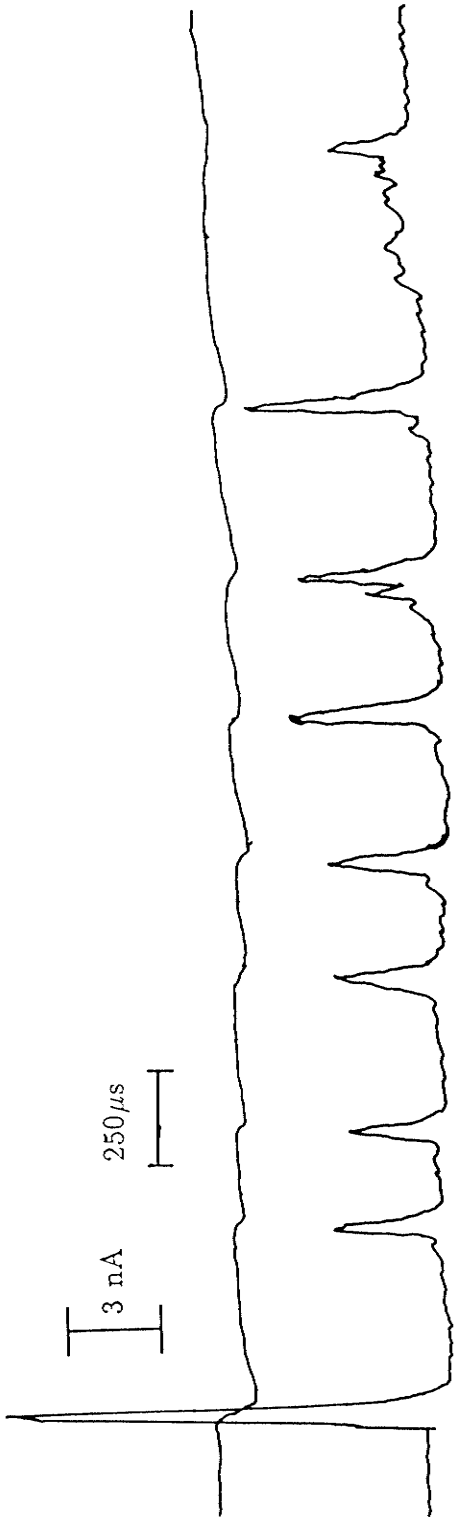

Figure 3.17: Severe z piezo and tunneling current activity seen following a pulse. Peak current was 13.4nA. Bias voltage was 1.25V, with a pulse voltage of 2.6V. No hillock was formed.

difficulty in image interpretation.

The z piezo and tunneling current traces obtained during the third study are quite similar to those recorded previously. At the lower total voltages, the response of the instrument is dominated by the coupling current. At higher voltages, the response changes as additional physical mechanisms, including material transfer, begin to dominate, sometimes resulting in hillocks. The exact nature of these other mechanisms is not yet known. The huge variations in hillock lifetime may be an indication of the type of mechanism responsible for its formation, and the material which formed it.

The single-crystal wire results are very encouraging as they indicate that some influence on the hillock production process is possible, and that reasonable hillock production probabilities may be achievable. The tip must undergo modification during the pinning attempts, as evidenced by the changes in pinning probability over the life of an experiment. Because of this, a method to characterize these tips is needed.

3.7 Conclusions

The results of the three studies indicate the following:

1. transfer of material between tip and surface is a mechanism responsible for the creation of hillocks in air and in liquid,
2. additional unknown mechanisms also exist,
3. a threshold voltage of approximately 3.5 to 4.5V exists, seemingly for all hillock-forming mechanisms,
4. mechanical contact between tip and surface is not responsible for the formation of craters,
5. operation at higher bias voltages is preferable, in order to decrease the possibility of material transfer between tip and surface,

6. operation with single-crystal W tips is preferable, due to their influence on pinning probability, and response to re-etching.

Chapter 4

Imaging Alkanes

4.1 Introduction

The hillocks manufactured by the pinning process and described in chapter 3 did not possess any distinct features which would enable their identification. In an effort to determine what features a hillock formed from an organic liquid might possess, a study was undertaken of the *n*-alkanes, of which decane is a member, adsorbed onto the surface of HOPG.

4.1.1 The *n*-alkanes

The *n*-alkanes are linear hydrocarbons characterized by a single carbon bond. The carbon atoms are arranged in a zig-zag chain, with a bond length of 1.54Å and an angle between adjacent bonds of 109°28'. The distance between carbon atoms on the same side of the zig-zag is 2.5Å. Figure 4.1(a) shows the relationship between carbon atoms in the chain. The ends of the chain are terminated by hydrogen atoms. Besides these terminations, two hydrogen atoms are bound to each carbon atom, with the same angle between these bonds as between the carbon bonds. Figure 4.1(b) illustrates the relationship between a pair of hydrogen atoms and its corresponding carbon atom. The chemical formula for an alkane consisting of m carbon atoms is n-C_mH_{2m+2}.

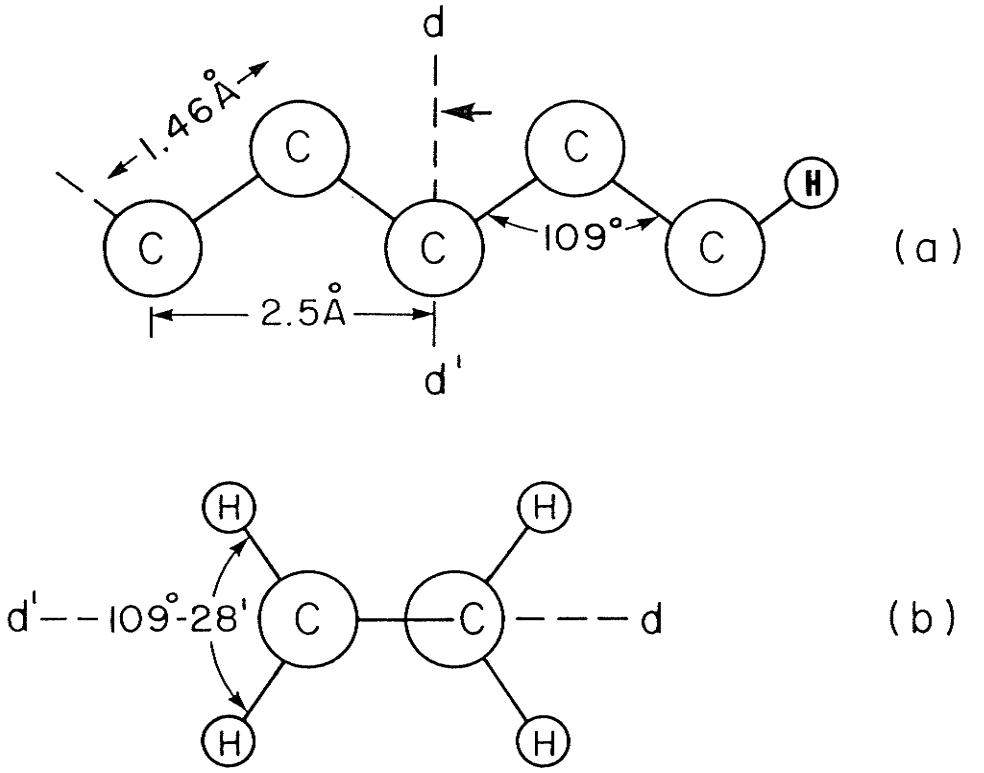

Figure 4.1: Structure of an *n*-alkane molecule. (a) shows carbon zig-zag and a hydrogen end termination (other H atoms not shown). (b) shows a view from an observer stationed along line d-d', looking in the direction of the arrow. This view indicates the positions of the H atoms.

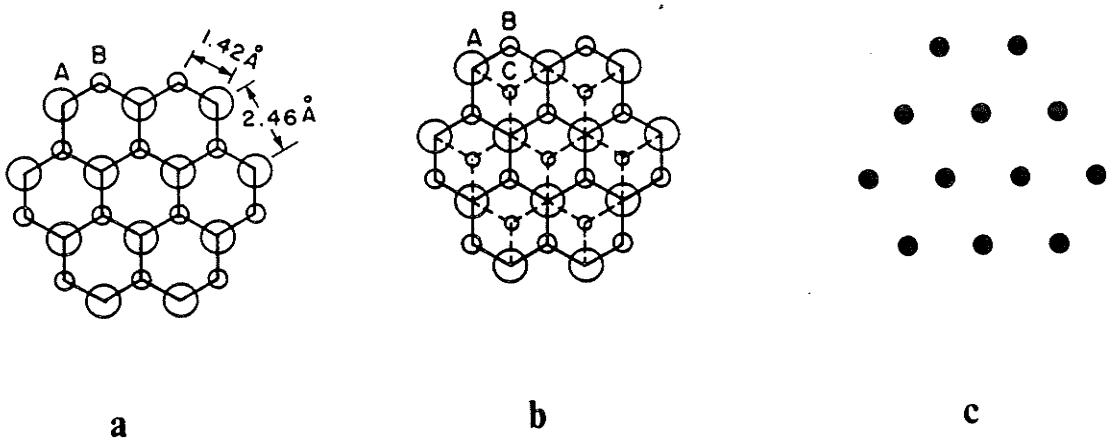

Figure 4.2: HOPG structure. (a) shows the A and B sites in the top layer. (b) shows the top layer along with the second layer C sites and structure (dashed). (c) shows the B sites in the top layer only - this corresponds to a typical STM image.

4.1.2 HOPG

As described in section 1.5, HOPG is a substrate used by many STM researchers. The graphite unit cell consists of 6 carbon atoms arranged in a hexagon, as shown in figure 4.2. In (a), atoms in sites labelled with an A have a neighbouring atom in the layer immediately underneath, while B site atoms do not. The hollow in the center of the hexagon also has an atom in the next layer, labelled with a C, as shown in 4.2(b). The structure of the second layer is drawn with dashed lines. The A site atoms are slightly higher than the B sites. Despite this, an STM image of HOPG is dominated by the B sites, as the influence of the A sites is diminished by electronic interaction with their neighbours in the next layer[84]. Because of this dominance, an STM image of graphite should correspond to figure 4.2(c). A typical HOPG image is shown for comparison in figure 4.3.

4.2 Alkane/Graphite Interaction

The adsorption of *n*-alkanes onto graphite has been characterized by low-energy electron diffraction[85], neutron diffraction[86] and calorimetry[87, 88]. Everett and Findenegg[88] measured the heats of adsorption onto HOPG of the even-numbered *n*-

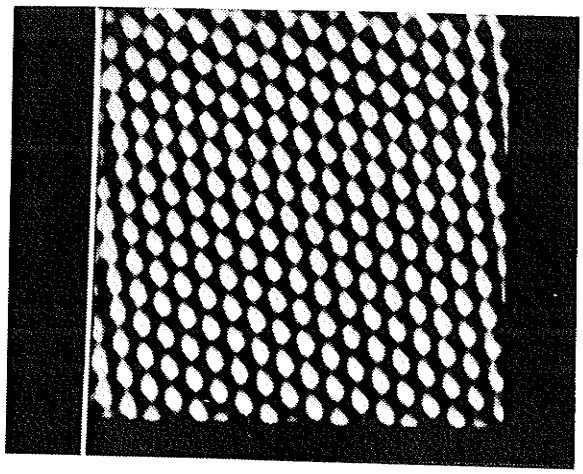

Figure 4.3: STM image of HOPG

alkanes from n-C_6H_{14} (hexane) to n-$C_{16}H_{34}$ (hexadecane). They found a rapid rise in the heat of adsorption with increasing molecular chain length. These longer molecules had melting points only slightly lower than the ambient temperature; because of this, Everett and Findenegg believed that, in the vicinity of the HOPG surface, adsorption forces were forming the molecules into an ordered structure.

Groszek[87] measured the heats of adsorption of n-$C_{32}H_{66}$ (dotriacontane) onto graphite from n-C_7H_{16} (heptane) and from 2,2,4-trimethylpentane (isooctane) solutions. The values obtained were in excess of those expected. He hypothesized that the dotriacontane must be forming an ordered structure on the surface, thus adding some heat of fusion to the heat of adsorption. In addition, he suggested a particular arrangement for this ordering. This arrangement, which is shown in figure 4.4, is due to the remarkable match between the alkane carbon backbone and the graphite hexagon. Groszek believed that the alkane hydrogen atoms (the hollow circles in figure 4.4) would fit into the hollow in the center of the graphite hexagon. However, at the time of his experiments, no direct observation of the adsorbed layers could be made.

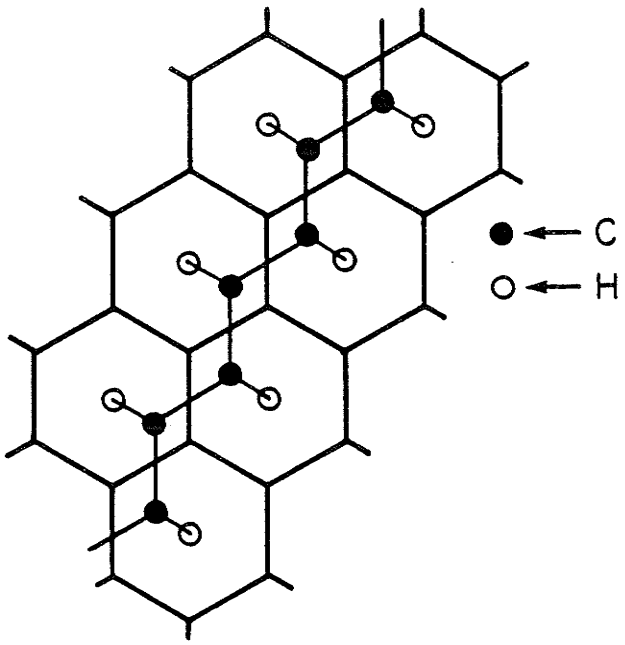

Figure 4.4: Groszek's suggested arrangement of $C_{32}H_{66}$ onto HOPG (from [87]).

4.3 Experimental Details

In an attempt to image Groszek's hypothesized structure, solutions containing dotriacontane were applied directly to a freshly-cleaved HOPG surface. The first solution consisted of 16mg of dotriacontane in 10ml of n-$C_{10}H_{22}$ (decane), while the second had 16mg of dotriacontane in 10ml of isooctane. The isooctane solution is applied to the surface first. This should deposit at least a monolayer of dotriacontane onto the graphite. However, isooctane evaporates quickly, so shortly after its application, the decane solution was added to the surface in an attempt to provide a relatively stable liquid environment. Following this, the surface was imaged by the NanoScope STM. Cold-worked PtIr tips were used predominantly, but similiar results were obtained with electrochemically etched W tips. Typical bias voltages were 0.4 to 1V, with current setpoints of 0.5 to 1nA.

As described above, Everett and Findenegg believed that pure n-alkanes near their melting temperature formed ordered structures on HOPG. Therefore, the adsorption of n-$C_{17}H_{36}$ (melting temperature of 22°C) onto HOPG was also investigated. In this case, the liquid was applied directly to the HOPG surface; no other

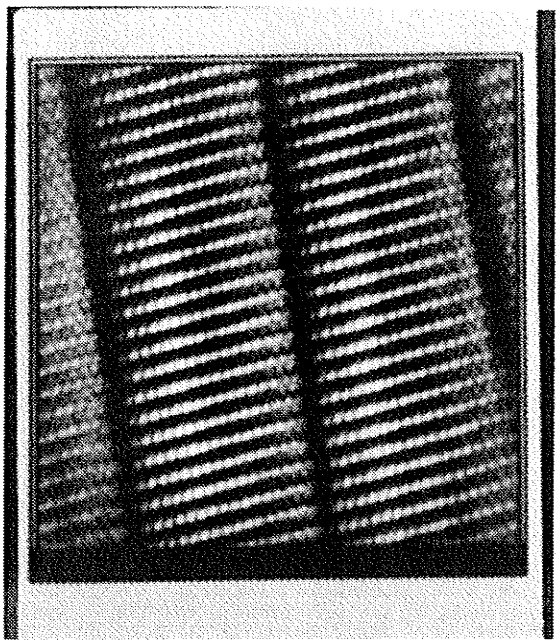

Figure 4.5: Image of an adsorbed layer of dotriacontane

solvent was used.

4.4 Results

4.4.1 Dotriacontane (n-$C_{32}H_{66}$)

An image of a dotriacontane monolayer is shown in figure 4.5[89], after filtering of its digital image. The layer consists of a two-dimensional array of dotriacontane molecules. Their long axes are parallel to each other and perpendicular to the gaps or troughs at their ends. Across the troughs, neighbouring molecules are offset by half their parallel spacing. The distance between troughs is consistent with the length of the molecule. The structure of this layer is similar to that of solid dotriacontane, which also consists of rows of parallel molecules[90].

The image seems to confirm Groszek's suggestion that the dotriacontane molecules form an adsorbed layer commensurate with the graphite. However, certain peculiarities can be found when the image is examined carefully. In particular, only sixteen

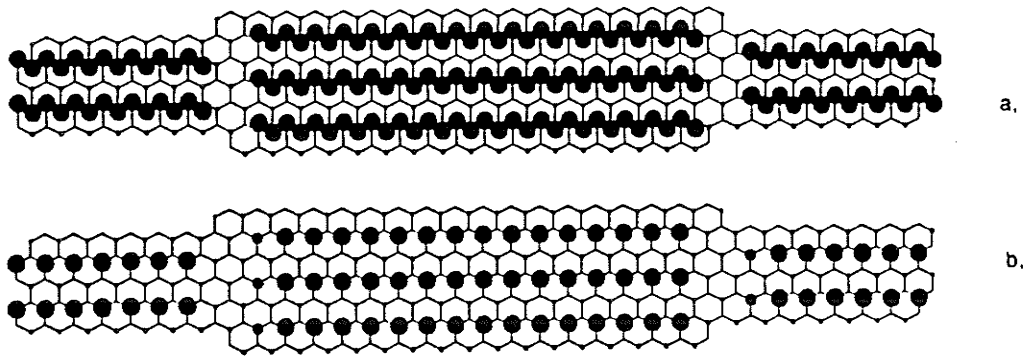

Figure 4.6: Model explaining dotriacontane image. (a) shows several molecules commensurate with the graphite. Also shown are graphite unit cells, each with the 3 sites imaged by the STM. (b) shows HOPG sites enhanced by the molecule.

maxima are seen along the molecule, whereas thirty-two might be expected due to the length of the molecule. Closer consideration of all details in the image indicate that it is dominated by features associated with the graphite substrate. This suggests that the molecule enhances tunneling into the substrate. To fully understand this, consider the illustration in figure 4.6(a), which shows several dotriacontane molecules adsorbed commensurate with the graphite. The graphite is represented by several of its unit cells, each with the three atomic sites imaged by the STM. In this model, the expected parallel spacing is 4.3Å which compares favorably with the measured spacing of 4.5±0.5Å. On the basis of this model, and assuming the molecule enhances tunneling into the substrate, only sixteen maxima should be seen, as shown in figure 4.6(b). Also, at the left end of each molecule, there is a partially enhanced site due to incomplete coverage of the substrate by the molecule. Excellent agreement exists between these interpretations of the model and the features in figure 4.5.

Additional evidence supporting tunneling enhancement can be found near the right end of each molecule. There, a zig-zag pattern reminiscent of the *n*-alkane chain can be observed. However, an examination of the distances and angles between points in the pattern reveals that they do not correspond to the alkane carbon chain;

instead, they match the substrate. Apparently, the molecule has shifted to straddle two rows of substrate tunneling sites. The exact reason for this is unknown but it may be related to the small but finite mismatch between the dotriacontane molecule and the graphite. The length of one of the alkane's C-C-C zig-zag is 2% longer than the 2.46Å spacing between hollows in the graphite lattice. Over the full length of the molecule, a mismatch greater than 20% could result. This mismatch may result in forces which dislocate the molecule from the substrate.

This feature provides further comfirmation that the dotriacontane adlayer must be commensurate with the HOPG. If the molecules did not adsorb in the manner shown in figure 4.6, then a more irregular image would result. Such an image may be so distorted that the presence of the molecules may be indistinguishable. Indeed, the appearance of the graphite lattice at the left end of each molecule suggests that the effect of the molecule may vanish altogether if it did not adsorb onto the surface in the manner described previously.

4.4.2 Heptadecane (n-$C_{17}H_{36}$)

An image of a heptadecane monolayer is shown in figure 4.7. The characteristic troughs are visible, but no parallel ordering of individual molecules can be seen. The spacing between the troughs is consistent with the two-dimensional ordering seen for dotriacontane, although the shorter length of the heptadecane molecule necessitates that the trough spacing be smaller. The heptadecane molecules enhance all the sites between the troughs, unlike dotriacontane. This lack of molecular resolution (in the same sense as dotriacontane), may be due to the higher surface mobility of the lighter heptadecane molecule.

4.5 Discussion

The experiments detailed above have a number of important ramifications in the following areas:

1. imaging mechanism,

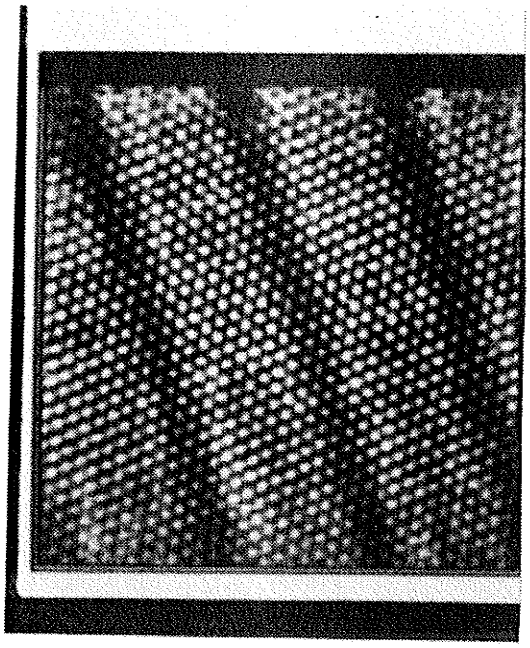

Figure 4.7: Image of an adsorbed layer of heptadecane

2. STM experimental techniques, and

3. hillock identification.

Prior to discussing each of these areas, an examination of the findings of other researchers who have investigated adsorbed organic molecules is useful.

4.5.1 Other Results

Spong et al. imaged adsorbed monolayers of various liquid crystals on graphite[91]. They also found ordered structures. However, their images did not show any atomic-like detail similar to that seen in figure 4.5, nor did they demonstrate how the molecule registered with the HOPG. Spong et al. suggested that the adsorbed molecule modulates the apparent barrier height of the substrate, as a result of local variations in the polarizibility of the liquid crystal.

Smith et al. also imaged adsorbed monolayers of liquid crystals, and also found ordered structures[92]. Unlike Spong et al. however, their images did contain atomic-like detail similar to figure 4.5. In addition, by changing the operating conditions, the

researchers were able to determine how the molecules registered with the graphite surface. They believe that the alkyl tail of their liquid crystal, which is similar in structure to the *n*-alkanes, matches the graphitic structure in the manner proposed by Groszek. However, they attribute the atomic-like detail in the tails to the hydrogen atoms, not the carbon ones. This interpretation is not consistent with the *n*-alkane results, and closer examination of the detail in the tails indicates that their interpretation may be incorrect[93]. The substrate carbon atoms appear enhanced by the tails; this enhancement must be due to the tail carbon atoms, assuming that the proposed registry of molecule with substrate is correct. Finally, Smith et al. suggest that the imaging mechanism is related to the density of states of the individual atoms in the molecule. They dispute the apparent barrier height modulation approach suggested by Spong et al.

Michel et al. imaged the *n*-alkanes on gold and platinum-carbon[94]. However, their images were of huge conglomerations of the molecules, as opposed to monolayers. These masses did not display any features which would readily allow for their identification as *n*-alkanes. However, a number did contain some periodic variations in their heights which matched the length of the molecule. In addition, some of the heights also matched the length of the molecule. In these cases, Michel et al. believed that the molecules were adsorbed onto the surface with their long axes perpendicular to the surface. The researchers were unsure of the imaging mechanism. In particular, they could not resolve how the very large, and supposedly insulating, masses could allow for any STM imaging.

4.5.2 Imaging Mechanisms

For monolayer adsorbates, the apparent substrate barrier height modulation proposed by Spong et al. is consistent with the *n*-alkane images shown above. In addition, atomic-like detail in the images of Smith et al. is also consistent with this imaging mechanism. The argument put forward by Smith et al., that the STM probes the density of states associated with the molecular hydrogen atoms, is inconsistent with the apparent enhancement of the substrate by the carbon atoms in the tail of their liquid crystal.

The results of Michel et al. and the existence of the amorphous hillocks described in chapter 3 indicate that imaging mechanisms besides substrate modulation must exist. Additional investigations are needed to ascertain these additional mechanisms.

4.5.3 STM Experimental Techniques

The observations of the dotriacontane and heptadecane adsorbed monolayers were repeatable but not predictable. Many attempts at observing the molecules proved less than satisfactory. On occasion, raising the bias voltage to almost 2V would cause the appearance of the monolayer. The elevated bias may change the condition of the tip, or it may promote the ordering of the molecules. The images generally were stable once formed. A voltage threshold between 0.3 and 0.5V was found; below this threshold the images became noisy. However, the adsorbate did not appear to be disturbed when the bias was lowered past this threshold.

Smith et al. also reported variations in the quality of their imaging attempts. Their best images were obtained after a 4V, 10μs pulse was applied to the tip. They also attribute this to a conditioning of the tip, or to a promotion of ordering of the molecules. Of particular interest is their finding that the graphite substrate could be imaged without noticing the effect of the molecules simply by decreasing the gap resistance (ie. by increasing the setpoint current or by decreasing the bias). When this occurs, they believe that the tip actually penetrates the monolayer. To minimize the possible disruption of the adsorbate by the tip, they normally operated with very small currents, between 50 to 400pA. This would allow for a large gap width.

Spong et al. also operated with a small current (200pA). In addition, Michel et al. normally used currents between 150 to 500pA. However, no disruption of their conglomerations were noted with a 2nA current.

The apparent need to operate at small setpoint currents (and therefore large gap widths), may be due to the effect of tip contamination. These contaminants may mechanically disrupt the adsorbates and inhibit the formation of the monolayers. A larger gap width would tend to decrease their adverse effects. Tip contamination would also explain the effect that increasing the tip voltage has on the imaging

process; the higher voltage "cleans" the tip and removes the disrupting influence. Note that this does not rule out the possibility that other factors (such as promoting the nucleation or polymerization of the layers) may also be influenced by the increased bias.

4.5.4 Hillock Identification

No convincing similiarities exist between features in the *n*-alkane monolayer images and the hillock images displayed in chapter 3. Consequently, some other method of identification of these hillocks is needed. The method of Michel et al. should be adopted in an attempt to provide some evidence that the hillocks were formed from the *n*-alkanes. Unfortunately, this will provide indirect evidence only.

4.6 Conclusions

The following can be concluded following consideration of the *n*-alkane experiments:

1. the composition of the pinned hillocks remains unknown,
2. *n*-alkane molecules form two-dimensional ordered monolayers commensurate with the graphite lattice,
3. the predominant imaging mechanism for these ordered monolayers involves modulation of the apparent substrate barrier height.

Chapter 5

Control System Limitations

5.1 Introduction

An STM is a complex electromechanical device which relies on precise positioning of a sharp tip for its sensing capabilities. Feedback control of tip position is essential to the operation of the instrument. Being physical entities, elements in the control system are non-ideal, and consequently suffer from limited frequency response, resonances, drifts, hysteresis and a whole host of other drawbacks. These place limits on the performance of the instrument, and may affect its utilization. However, a more fundamental limitation on STM performance exists. This results from noise in the tunneling junction and manifests itself as an uncertainty in the vertical position of the tip.

5.2 Review

Various researchers have explored the properties of STM control systems. Rather than addressing fundamental limitations, however, these individuals investigated particular implementations and determined design tradeoffs. To do this, many considered all facets of the instrument's design, such as the effects of vibrations and choice of scanner, rather then just the design of the control system.

Pohl was one such individual[95]. He examined vibrations in the environment and suggested ways of combating them. He also examined different piezo configurations and evaluated each in terms of displacement and stiffness, and undesirable properties, such as drift, hysteresis and creep. In his analysis, the control system had to provide precise positioning and fast response while preventing oscillations. He believed that the ability of the control system to position the tip must be better then the resolution desired. This results in tolerance requirements of approximately 0.01 Å vertically and 0.1Å parallel to the surface. This requirement should be applied to all instruments. However, because of the unique properties of a given design, the control system needed to implement this requirement will have to be individually tailored.

Park and Quate performed a theoretical analysis of both feedback control and vibration isolation systems for their STM design[96]. Their control system analysis concentrated on the time delay inherent in any physical system. The controller did not use integral feedback. Instead, large and slow variations in surface height were the responsibility of a second control system ignored in their analysis. Because of this, their system suffered from finite positioning errors when the nominal separation between tip and surface changed.

Kuk and Silverman briefly described the STM design process[97]. Like the researchers mentioned previously, they also included vibration considerations. Their suggested control system featured both proportional and integral feedback. A first order transfer function was used to model each element in the design, except for the tunnel junction itself which was modelled with a second order function. Using these individual models, a transfer function for the entire system was determined. At this point, the researchers determined the appropriate parameters for the overall transfer function by testing their own instrument. With this completed, a gain for the overall function was determined. This gain gave a critically damped performance, which allows for the fastest possible response without oscillatory behaviour. The control system electronics could then be designed to provide this gain. Again, the control system is tailored to individual designs.

DiLella et al. investigated the design of an STM featuring a tube scanner and integral feedback[98]. They measured directly the transient and frequency response of their instrument and used this information when the design of the control system

electronics was finalized. An analysis of their control system indicated that the steady-state error would be zero, as expected for an integral feedback or type 1 controller.

Tiedje and Brown investigated a tube scanner STM with both integral and proportional feedback[99]. They analyzed the noise of the preamp, the electromechanical response of the piezo and the performance of the control system, in order to obtain quick imaging of a fairly large surface area, yet still with atomic resolution. Their analysis led to the specification of a number of design tradeoffs which could prove useful for similar designs.

The analysis by Thomson differed from those just described as no specific design was investigated[100]. Instead, the potential use of an STM as an information storage device was explored by determining the limits to the read and write rate of such a device. Thomson argued that ultimately the rates would be limited by the shot noise of the tunneling current. Shot noise is the term given to variations in an electrical signal caused by the random emission of charge carriers. In an STM, the shot noise would be caused by the arrival of electrons tunneling across the junction at random times. With a setpoint current of 1nA, Thomson determined that the read and write rates would be limited to 20 Mbits/s.

With the exception of the analysis presented by Thomson, questions regarding the fundamental limitations of the STM were never addressed by these researchers. Some indication of the fundamental performance limits may prove useful. For example, they could be used to provide "rules of thumb" relating scan rates, scan ranges, setpoint current values and other operator-specified parameters to one another.

5.3 Analysis Assumptions

As mentioned in section 5.1, a fundamental limitation on STM performance results from noise in the tunneling junction, which manifests itself as an uncertainty in the vertical position of the tip. In order to analyze this situation a number of simplifying assumptions were made. These were:

1. tip positioning can be accomplished at arbitrarily high frequencies (this implies that the vertical piezo is ideal),

2. the only limitation to positioning is the noise inherent in the signal, and the bandwidth of the control system itself.

The only noise in the signal is assumed to be the shot noise of the current in the tunneling junction. The bandwidth is set by some component within the system, such as a high voltage amplifier for example.

In the first part of the analysis, an additional assumption was made. The tip is assumed to be stationary in x and y and as a result, in the absence of noise, the vertical position of the tip should be stationary as well. However, because of the shot noise in the current, the vertical position will oscillate as the control system adjusts to eliminate this noise.

The exponential dependence of the current on tip-to-surface separation introduces a non-linearity into the analysis. Two approaches were taken to surmount this non-linearity. The first is the standard control theory approach using a linear approximation. This approximation is valid provided the noise in the signal and the resulting variation in the separation is small. For this reason, it is referred to as the small signal approximation. In the second approach, dubbed the large signal case, the variation is no longer small and the assumption of a constant slope at the setpoint current can no longer be used. Instead, calculations must take into account the exponential dependence of the current on the separation.

5.4 Small Signal Approximation

Dorf describes the rationale behind the small signal approximation[101]. A portion of it is given here. Assume $y = g(x)$. A Taylor Series expansion of $g(x)$ about x_0 gives:

$$y = g(x_0) + \frac{dg}{dx}\Big|_{x_0} \frac{(x - x_0)}{1!} + \frac{d^2g}{dx^2}\Big|_{x_0} \frac{(x - x_0)^2}{2!} + \cdots \tag{5.1}$$

With $(x - x_0)$ small, the higher order terms can be disregarded, leaving,

$$y = y_0 + \frac{dg}{dx}\Big|_{x_0} (x - x_0) \tag{5.2}$$

$$y - y_0 = m(x - x_0) \tag{5.3}$$

$$\Delta y = m\Delta x \tag{5.4}$$

where m is the slope at $x = x_0$.

As described in chapter 1, the expression for the tunneling current is:

$$I_t = K\, V_t \exp -(A\sqrt{\phi}\, z) \tag{5.5}$$

Here z replaces s and a constant of proportionality, K, has been introduced (see equation 1.1). The derivative of tunneling current with respect to the vertical position of the tip is:

$$\frac{dI_t}{dz} = K\, V_t \exp -(A\sqrt{\phi}\, z) * (-A\sqrt{\phi}) \tag{5.6}$$

$$= -A\sqrt{\phi}\, I_t \tag{5.7}$$

$$\Rightarrow dz = \frac{-1}{A\sqrt{\phi}} \frac{dI_t}{I_t} \tag{5.8}$$

$$\approx \frac{-1}{\sqrt{\phi}} \frac{dI_t}{I_t} \tag{5.9}$$

The units of dz are in Å provided ϕ is in eV. The sign of dz indicates the direction of the change of the tip position. In this analysis, only the magnitude is important. Therefore,

$$|dz| = \frac{1}{\sqrt{\phi}} \frac{dI_t}{I_t} \tag{5.10}$$

$$\Rightarrow \Delta z = \frac{1}{\sqrt{\phi}} \frac{\Delta I_t}{I_t} \tag{5.11}$$

$$\tag{5.12}$$

The variation in the tunnel current, (ΔI_t), results from shot noise; an expression for it is[102],

$$\Delta I_t = (2eI_t\Delta f)^{1/2} \tag{5.13}$$

$$\Rightarrow \Delta z = \frac{1}{\sqrt{\phi}} \left[\frac{2e\Delta f}{I_t}\right]^{1/2} \tag{5.14}$$

In these expressions, e is the electronic charge and Δf is the control system bandwidth. For this analysis, a value of 4eV has been assigned to ϕ. This is typical of many metals[103]. Therefore, the expression for Δz becomes:

$$\Delta z \approx \frac{1}{2}\left(\frac{2e\Delta f}{I_t}\right)^{1/2} \tag{5.15}$$

This was used to determine the variation in tip position as a function of control system bandwidth, for a number of different setpoint currents. The results are shown in figure 5.1. A demarcation line was drawn on this figure. Below this line, the variation in the tip position will not exceed 0.01 Å, which was suggested by Pohl as a desirable vertical positioning accuracy.

The small signal approximation assumes that the deviation in the value of the current is negligible as the vertical position of the tip varies. The expression relating tunneling current to tip position can be used to determine the deviation for a given value of Δz. However, before this can be done, the nominal value of z_s must be determined. An expression for it can be found from equation 5.5. The expression is:

$$z_s = \frac{1}{A\sqrt{\phi}} \ln \frac{K V_t}{I_t} \tag{5.16}$$

As before, $A \approx 1\text{eV}^{-1/2}\text{Å}^{-1}$ and $\phi = 4\text{eV}$. The values chosen for V_t and K are 0.1V and $30\Omega^{-1}$, respectively. With the nominal value of z determined for a given setpoint current, the variation Δz can be used to determine the deviation in the current. Table 5.1 shows values associated with a 0.01Å variation in z. The deviation is about 2%, which is acceptable for a small signal approximation.

The deviation from the nominal current value increases with increasing variation in tip position. At a Δz of 0.05Å the deviation is approximately 10%. It increases to about 20% when Δz reaches 0.1Å. In addition, the error becomes increasingly asymmetric, with the deviations for negative values of Δz (tip approaching the surface) exceeding those for positive ones. This asymmetry is not unexpected as it is due to the exponential dependence of the current on z. The current deviations corresponding to a Δz of 0.5Å is -63.2% for a positive Δz and 172% for a negative one. As expected, the ratio of the deviations is e.

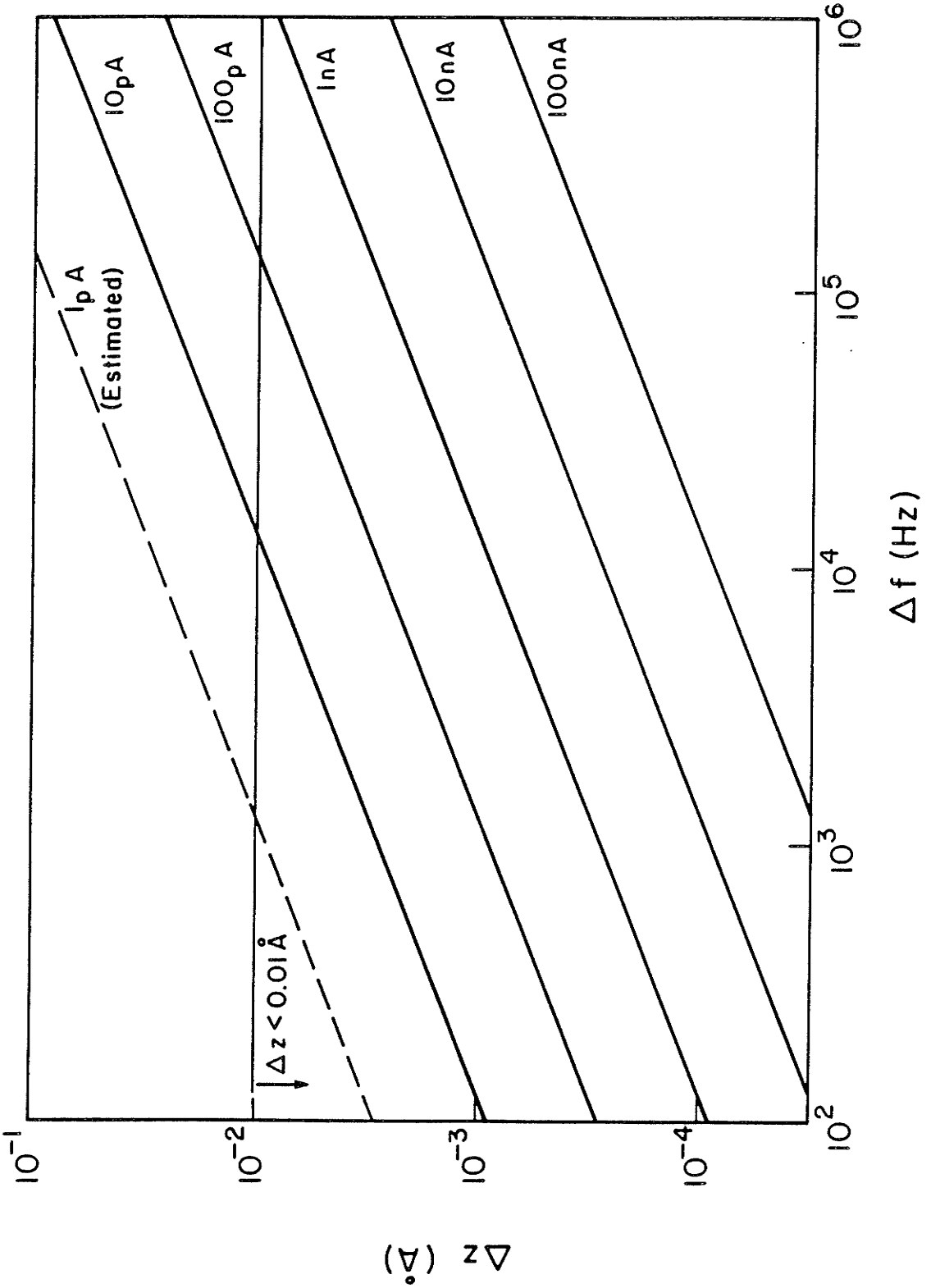

Figure 5.1: Noise-induced tip variation vs. bandwidth (small signal approximation)

I_t (nA)	z (Å)	I_t (nA)		ΔI_t(%)	
		$(+\Delta z)$	$(-\Delta z)$	+	-
100	8.61	97.7	101.7	-2.0	2.0
10	9.76	9.80	10.19	-2.0	2.0
1	10.91	0.98	1.02	-2.0	2.0
0.1	12.06	0.099	0.103	-2.0	2.0
0.01	13.21	9.87pA	10.27pA	-2.0	2.0

Table 5.1: Current deviations for a 0.01Å Δz

The Δz value at which the small signal approximation no longer holds is arbitrary. Pohl's suggested value of 0.01Å gives an error of about 2%. Dorf implies that a 2% error is acceptable. Consequently, this Δz value can be used as the boundary separating the small signal approximation from the large signal case.

5.5 Large Signal Case

5.5.1 Introduction

As Δf is increased, the noise increases also. As a result, the linear relationship between ΔI and Δz no longer holds. That is, the exponential behaviour of current on separation must now be considered. In addition, the increased noise and resulting deviations in the separation may appreciably change the value of the tunneling current. (In the small signal approximation, the tunneling current was assumed to stay constant at the setpoint value.) This appreciable change may in turn give a different value for the noise, which will affect the separation differently and may in turn result in yet another appreciable change in the tunneling current. Lastly, because the variation in current and separation was considered small in the small signal approximation, frequency response considerations were ignored. However, with these variations now much greater, the limited frequency response may have a noticeable effect. The large signal analysis addresses these issues.

5.5.2 Model

To determine the effect of these issues, consider the model of an ideal STM control system shown in figure 5.2. Both the tunnel junction and the piezo have frequency responses which extend well beyond that of the controller, which is assumed to have a 3dB bandwidth equal to Δf. The setpoint current is denoted by I_s, the actual tunneling current by I_t, the noise by ΔI and the voltage on the z piezo by V_z. In this model, the error in the current is given by:

$$e = I_s - (I_t + \Delta I) \tag{5.17}$$

The z piezo voltage is:

$$V_z = G(f)e \tag{5.18}$$

and the output of the tunneling junction is given by:

$$I_t + \Delta I = K_1 K_2 V_z \tag{5.19}$$

Combining these three equations gives:

$$V_z = \frac{G(f)I_s}{1 + G(f)K_1K_2} \tag{5.20}$$

Provided $G(f)K_1K_2 \gg 1$, this can be approximated by:

$$V_z \approx \frac{G(f)I_s}{G(f)K_1K_2} \tag{5.21}$$

or

$$V_z = \frac{I_s}{K_1K_2} \tag{5.22}$$

This leads to

$$I_t + \Delta I = I_s \tag{5.23}$$

or

$$I_t = I_s - \Delta I \tag{5.24}$$

This implies that the control system responds to the noise by adjusting the tip height so that the actual tunneling current is reduced (or increased if the noise is negative) by an amount equal to the noise. In addition, because there is no

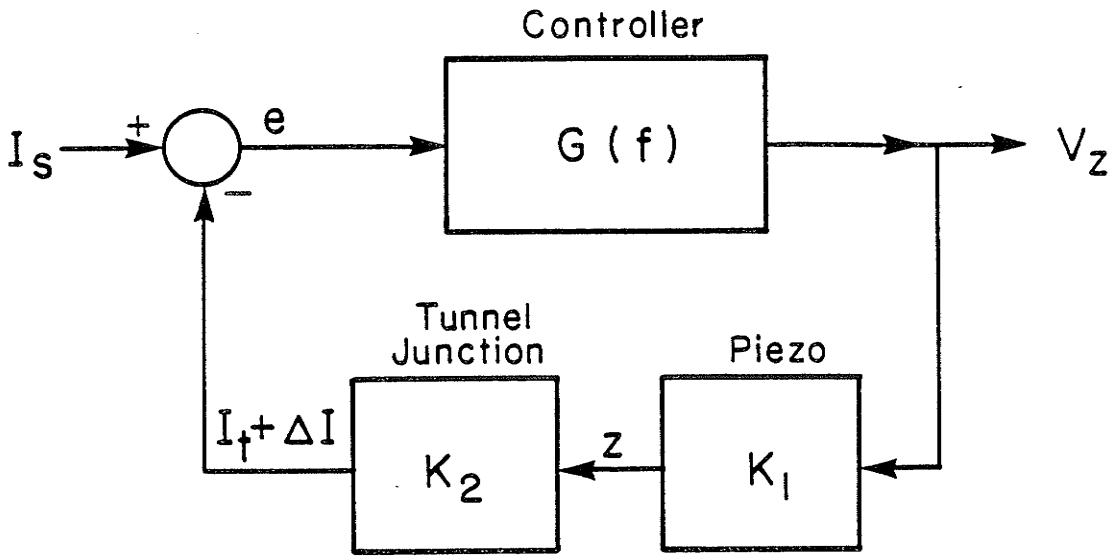

Figure 5.2: Model for an ideal STM control system with only one frequency limiting component.

frequency dependence in the equation, the control system makes this adjustment instantaneously. The limited bandwidth of the controller merely defines the value of the noise. The approximation made during this derivation must be treated cautiously. Making the gain $GK_1K_2 \gg 1$ may lead to oscillations and even instabilities in a non-ideal situation.

There is a somewhat more intuitive argument associated with the removal of the frequency dependence. As mentioned, the frequency limiting component is considered to have ideal characteristics. Noise with spectral content above Δf will be extinguished by this component, and therefore will not effect the rest of the system. Noise with frequencies below Δf will be passed by the component. However, the remainder of the control system can react to remove this perceived change in current with the same speed that the noise affects the instrument. As a result, the actual tunneling current I_t will equal the setpoint current I_s reduced by the noise.

5.5.3 Expression for Δz

The effect of large noise-induced current variations on the tip-to-sample separation can be determined using the equation just derived and equation 5.5, which relates current to separation.

$$I_t = I_s - \Delta I \tag{5.25}$$

$$K V_t \exp -(A\sqrt{\phi}\, z) = I_s - \Delta I \tag{5.26}$$

$$\Rightarrow z = \frac{-1}{A\sqrt{\phi}} \ln \frac{I_s - \Delta I}{K V} \tag{5.27}$$

$$\Delta z = z - z_s \tag{5.28}$$

$$= \frac{-1}{A\sqrt{\phi}} \ln \frac{I_s - \Delta I}{K V} - \frac{-1}{A\sqrt{\phi}} \ln \frac{I_s}{K V} \tag{5.29}$$

$$= \frac{-1}{A\sqrt{\phi}} \ln \frac{I_s - \Delta I}{I_s} \tag{5.30}$$

$$= \frac{-1}{A\sqrt{\phi}} \ln \left(1 - \frac{\Delta I}{I_s}\right) \tag{5.31}$$

where

$$\Delta I = (2eI_t \Delta f)^{1/2} \tag{5.32}$$

The value of the tunneling current must be known in order to determine the change in the separation resulting from the noise caused by this current. For small bandwidths and large currents, $I_t \approx I_s$. This was the basis for the small signal approximation. As the bandwidth increases, the instantaneous tunneling current deviates from this approximation; however, the average tunneling current is maintained at the setpoint value. Therefore, even though the instantaneous value is not known, the average can be used as an estimate for it. Therefore,

$$\Delta I \approx (2eI_s \Delta f)^{1/2} \tag{5.33}$$

This gives

$$\Delta z \approx \frac{-1}{A\sqrt{\phi}} \ln \left(1 - \frac{(2eI_s \Delta f)^{1/2}}{I_s}\right) \tag{5.34}$$

The noise acts to increase and decrease the current; therefore, ΔI can be considered to be both positive and negative. For example, a setpoint current of 10pA and a

bandwidth of 1MHz gives two Δz.

$$\Delta z^{+} = \frac{-1}{A\sqrt{\phi}} \ln\left(1 - \frac{1}{5.59}\right) \tag{5.35}$$

$$= 0.0985\text{Å} \tag{5.36}$$

$$\Delta z^{-} = \frac{-1}{A\sqrt{\phi}} \ln\left(1 - \frac{-1}{5.59}\right) \tag{5.37}$$

$$= -0.0823\text{Å} \tag{5.38}$$

Again, $A \approx 1\text{eV}^{-1/2}\text{Å}^{-1}$ and $\phi = 4\text{eV}$. In the Δz^{+} case, the noise has acted to increase the tunneling current seen by the control system. It reacts to this by increasing the tip-to-sample separation. This reduces the real tunneling current to a value equal to the setpoint current less noise; it also reduces the current seen by the control system to the setpoint value. In the Δz^{-} case, the noise has decreased the tunneling current seen by the control system. It reacts to this by decreasing the separation, thereby increasing the tunneling current. This has the effect of restoring the current seen by the control system to the setpoint value.

The technique just described was used to determine the variation in tip position as a function of control system bandwidth, for a number of different setpoint currents. Figure 5.3 shows a plot of the results. Both Δz^{+} and Δz^{-} results are shown, as well as Δz_{rms}, which is defined as

$$\Delta z_{rms} = \sqrt{\frac{(\Delta z^{+})^2 + (\Delta z^{-})^2}{2}} \tag{5.39}$$

At small Δf, the small signal values are approached. At higher Δf, the asymmetry due to the exponential dependence of I_t on z begins to manifest itself.

The 1 and 10pA curves end at bandwidths of approximately 3 and 30 MHz respectively. At these points, the noise current value has equalled the setpoint current. This results in the argument of the natural logarithm in equation 5.34 being equal to zero when the noise acts to increase the current seen by the control system (ie. $\Delta I > 0$). The interpretation of this enigmatic result illustrates a possible problem with the instrument.

When the noise value equals the setpoint current and is positive, then the current seen by the control system appears to have doubled. To remove the excess, which

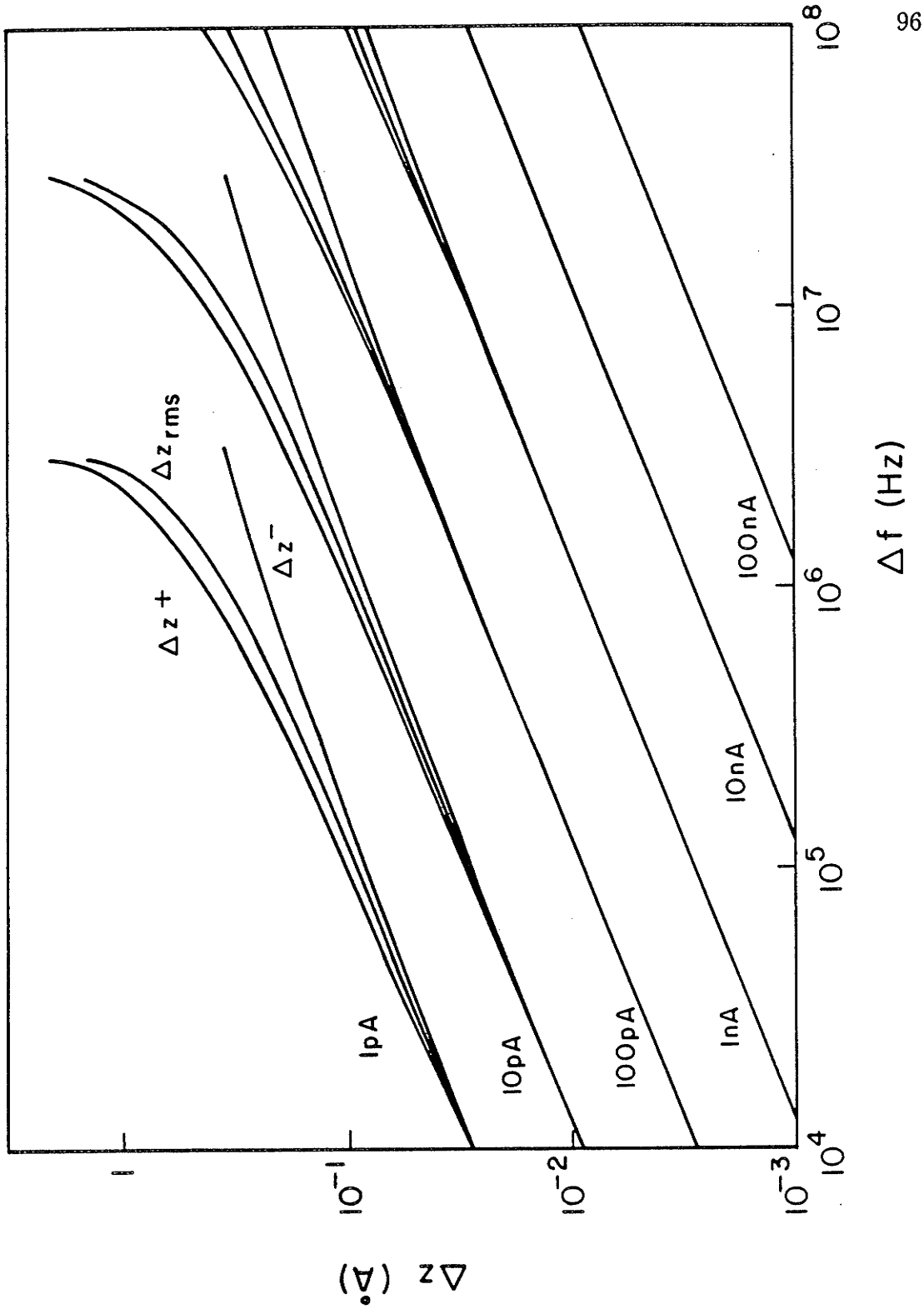

Figure 5.3: Noise-induced tip variation vs. bandwidth (large signal case)

equals the setpoint value, the control system must position the tip so that the actual tunneling current drops to nothing. Physically, the tip must be moved out of tunneling range. Mathematically, $\Delta z \rightarrow \infty$. This requirement is reflected in the argument of the natural log becoming zero.

An even more interesting interpretation arises when ΔI equals the setpoint current and is considered negative. Equation 5.34 can accommodate any large negative value for ΔI. Indeed, at a 1pA current, the noise can be five times the setpoint and still result in a Δz of less then 1Å. However, a negative ΔI refers to a reduction in the tunneling current, not a change in the direction of its flow, so at most a negative ΔI can only equal the setpoint value. When this occurs, the tunneling current seen by the control system appears to have dropped to zero. This should result in a large negative Δz as the control system attempts to increase the current back to the setpoint value.

Of these two possible control system reactions to large noise variations, the second is much more serious, as it might result in contact between tip and surface.

5.5.4 Crash Probability

Noise is a random process, so even when its value equals the setpoint current, contact between tip and surface, or a *crash* may not occur. Perhaps more importantly, a crash may occur even when the noise value is smaller then the setpoint. The discussion of a crash must be based on the statistics of the noise. The conclusions will vary depending upon the distribution considered for the noise. Because of this, two different distributions were investigated.

The first was the Gaussian distribution. Here, ΔI represents the standard deviation of the tunneling current about the average value, which is the setpoint current. This distribution can be related easily to equation 5.34 in that ΔI can take on positive or negative values. With this distribution, a crash will occur when the instantaneous current is 0 or negative. Therefore, the probability of a crash in a duration of time equal to $1/\Delta f$ is simply the area under the Gaussian curve to the left of 0, as shown in figure 5.4.

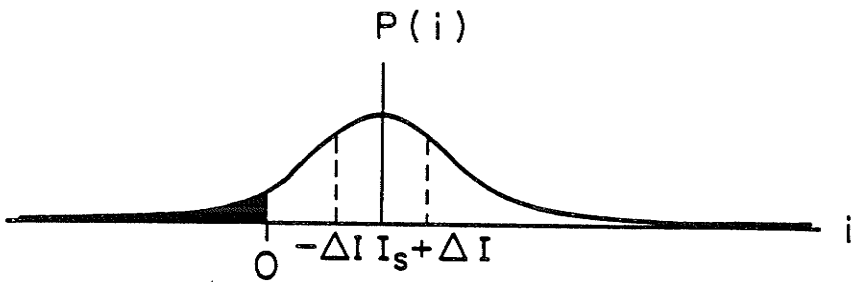

Figure 5.4: Gaussian distribution of tunneling current. Crash probability is given by the shaded area.

The equation for a Gaussian curve with the mean shifted by I_s and with a standard deviation of ΔI is:

$$p(i) = \frac{1}{\Delta I\sqrt{2\pi}} \exp \frac{-(i - I_s)^2}{2(\Delta I)^2} \tag{5.40}$$

Therefore the probability of a crash, P_c, is:

$$P_c = \int_{-\infty}^{0} p(i)di \tag{5.41}$$

$$= \int_{-\infty}^{0} \frac{1}{\Delta I\sqrt{2\pi}} \exp \frac{-(i - I_s)^2}{2(\Delta I)^2} di \tag{5.42}$$

By making the change of variable $z = (i - I_s)/\Delta I$, the expression for P_c reduces to:

$$P_c = \frac{1}{\sqrt{2\pi}} \int_{-\infty}^{-I_s/\Delta I} \exp \frac{-z^2}{2} dz \tag{5.43}$$

$$= \text{erf}\left(\frac{-I_s}{\Delta I}\right) \tag{5.44}$$

The argument of the error function is simply the signal-to-noise ratio (SNR). Therefore,

$$P_c = \text{erf}(-\text{SNR}) \tag{5.45}$$

$$= \text{erfc}(\text{SNR}) \tag{5.46}$$

where erfc is the complementary error function defined as:

$$\mathrm{erfc}(x) = \frac{1}{\sqrt{2\pi}} \int_x^\infty \exp \frac{-x^2}{2}\, dx \tag{5.47}$$

The unfortunate aspect of the use of the Gaussian distribution is its reliance on the concept of negative current, which, as described earlier, is very unphysical.

This reliance can be removed by considering the distribution of the noise to be Poisson. Indeed, shot noise has been found to be Poisson, so its use in determining the probability of a crash is much more appropriate. The Poisson distribution is[104]:

$$P(n) = \frac{\overline{n}^n \exp(-\overline{n})}{n!} \tag{5.48}$$

where n is the actual number of events occuring in an interval and $\overline{n}$ is the average number of events occurring in this interval. For the purposes of this discussion, n is the actual number of electrons crossing the tunnel junction in an interval of time $\tau = 1/\Delta f$, and $\overline{n}$ is the average number of electrons in this interval. The average number of electrons is determined by the setpoint current:

$$\overline{n} = \frac{I_s}{e\Delta f} \tag{5.49}$$

A crash occurs when the actual number of electrons tunneling across the junction in time τ is 0. Therefore:

$$\begin{aligned} P_c &= P(n=0) && (5.50)\\ &= \frac{\overline{n}^0 \exp(-\overline{n})}{0!} && (5.51)\\ &= \exp(-\overline{n}) && (5.52)\\ &= \exp\left(\frac{-I_s}{e\Delta f}\right) && (5.53) \end{aligned}$$

Another figure of merit can be defined. This is the time until a crash occurs, denoted as τ_c. This figure of merit is determined by multiplying the probability of a crash by the duration of the interval. This gives the frequency of crashing. The time-to-crash is then the inverse of this value. Therefore:

$$\tau_c = \frac{1}{P_c \Delta f} \tag{5.54}$$

The units of τ will be in seconds provided Δf is in Hz.

Figure 5.5 is a plot of the crash probabilities for the two distributions assuming a setpoint current of 1pA. Along with the curves, various SNR's and $\overline{n}$ are also shown. The Gaussian probability of a crash, P_c^G, will never exceed 0.5, even with a SNR $\rightarrow \infty$. In this limit, any noise which decreases the current will cause a crash, while any which increases the current will not. This is a very unrealistic limit and is a reflection of the inadequacy of the Gaussian distribution to represent the process in the tunnel junction when the bandwidth becomes so large that the noise current equals the setpoint value. Meanwhile, as expected, the Poisson probability of a crash, P_c^P, does tend to 1.0 as Δf increases.

Figure 5.6 provides some insight when the limit is reached. It is a plot of the time-to-crash for the two distributions, again with a setpoint current of 1pA. At a bandwidth of 1MHz, where P_c is still quite small for both distributions, the time-to-crash is less then 1ms. This could not be tolerated in a realistic situation. The time-to-crash for the Poisson distribution, τ_c^P rises much quicker then τ_c^G as the approximation used for erfc(SNR), when SNR > 3, causes

$$\tau_c^G \propto \exp \frac{I_s}{4e\Delta f} \tag{5.55}$$

whereas

$$\tau_c^P \propto \exp \frac{I_s}{e\Delta f} \tag{5.56}$$

To fully exploit this difference, however, would require the use of sophisticated electron counting techniques which could not be adapted for use in an STM. As the bandwidth diminishes and the average number of electrons rises, the Poisson distribution approaches the Gaussian. Because of this, the Gaussian curve may more closely represent the normal time-to-crash in a conventional STM, provided the average number of electrons crossing the tunnel junction is large. At a bandwidth of 100kHz, the time-to-crash for a 1pA current with Gaussian noise is 884s or about 15 minutes. The associated SNR is 5.6 and on average, 62 electrons cross the tunnel junction in τ, which is 10μs in this case. Table 5.2 shows a selection of currents and bandwidths required to give a τ_c of approximately 15 minutes.

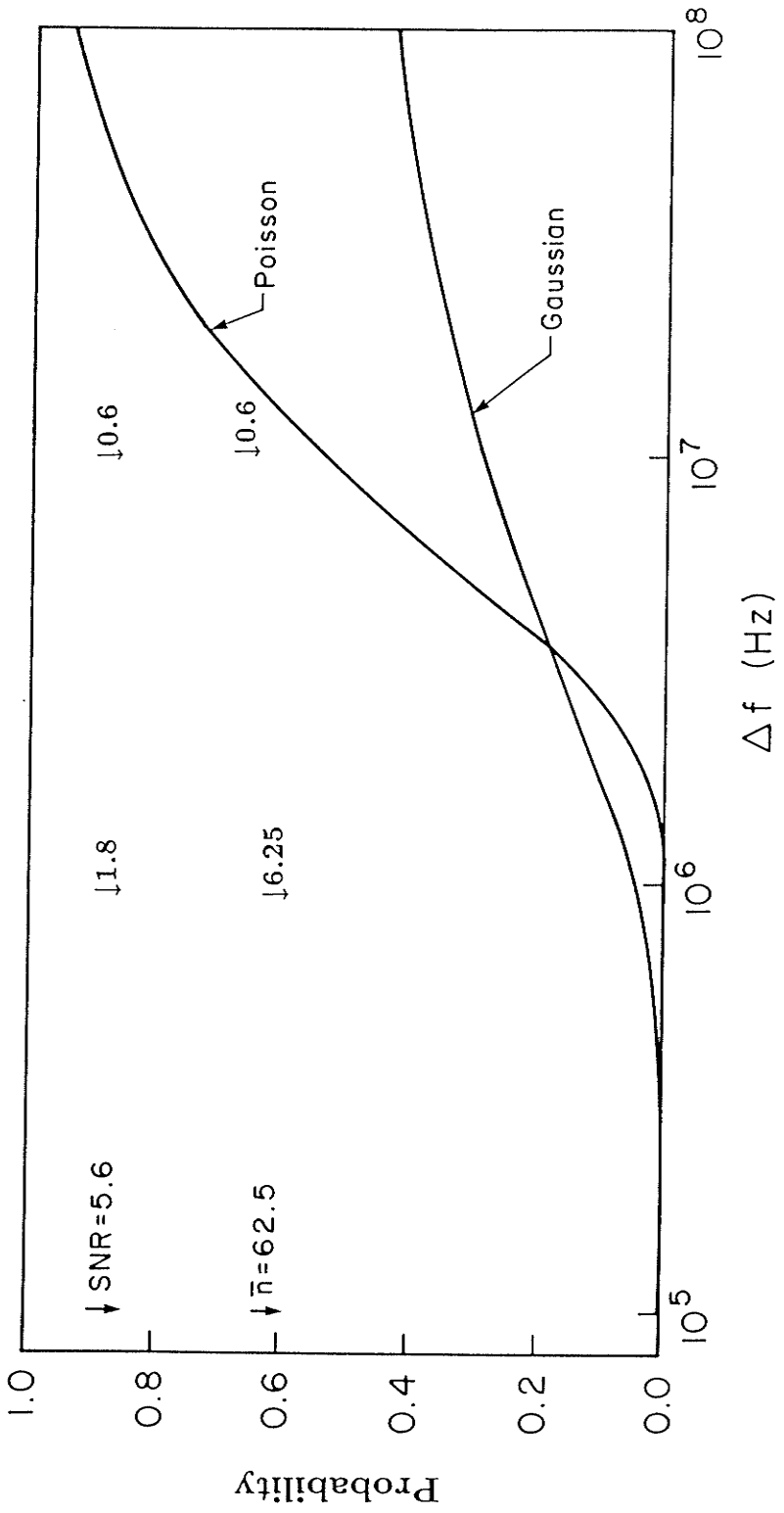

Figure 5.5: Crash probability vs. bandwidth for Poisson and Gaussian distributed noise currents. I_s =1pA.

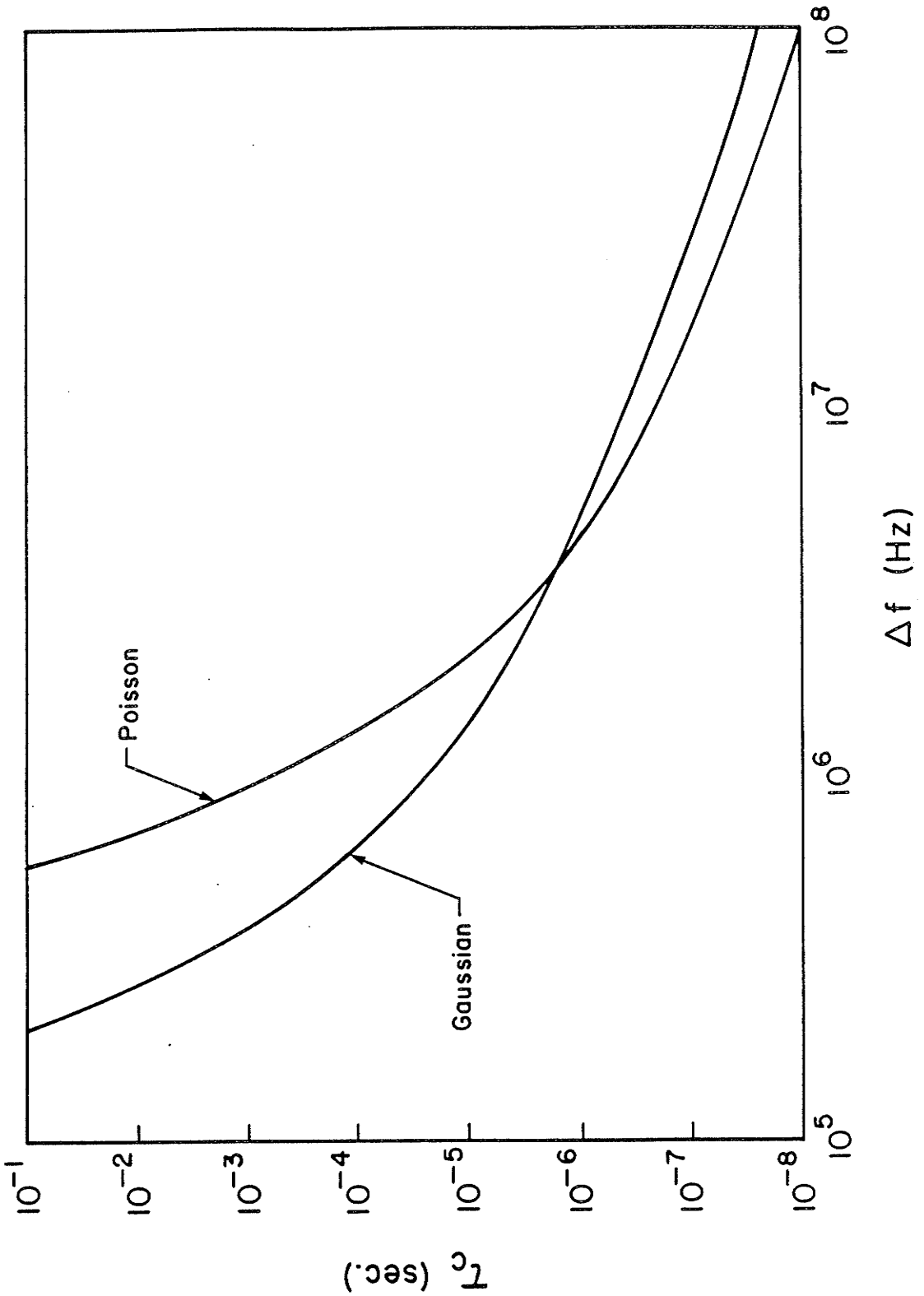

Figure 5.6: Time-to-crash vs. bandwidth for Poisson and Gaussian distributed noise currents. I_s =1pA.

I_s (pA)	Δf (MHz)	SNR	$\overline{n}$	τ_c (s)
1	0.1	5.6	62.5	884
10	0.88	6.0	71.0	898
100	7.85	6.3	79.6	911
1 nA	71.0	6.6	88.0	865
10 nA	647.0	7.0	96.6	846

Table 5.2: Currents and bandwidths required for time-to-crash of about 15 minutes

5.5.5 Effect of changing current

The preceding discussions all used the approximation that the tunneling current equals the setpoint current. On average, this equality is correct. However, the instantaneous tunneling current was found to differ from the setpoint by an amount equal to the noise. In an attempt to see the effects of this, a computer simulation was performed. The essential calculations performed during each iteration are:

$$\Delta I_i = \left[\frac{2eI_i}{\Delta f}\right]^{1/2} \tag{5.57}$$

$$I_{t_i} = I_i + r_i \Delta I_i \tag{5.58}$$

$$e_i = I_{t_i} - I_s \tag{5.59}$$

$$I_i = I_s - e_i \tag{5.60}$$

$$\Delta z_i = -0.5 * \ln \frac{I_i}{I_s} \tag{5.61}$$

$$Z = Z + (\Delta z_i)^2 \tag{5.62}$$

$$I = I + I_i \tag{5.63}$$

Following this last calculation, the sequence would start again. At the start of the simulation, I_i was set to I_s. At the end of a prescribed number of iterations, N, the rms value of Δz was determined using $(\Delta z)_{rms} = \sqrt{Z/N}$. In addition, the average current value was found using $I_{av} = I/N$. In the second equation, r_i denotes a random value with a Gaussian distribution. For each iteration, the computer first generated a uniformly distributed random value which ranged between 0 and 1.

# iterations	$(\Delta z)_{rms}$ (Å)	I_{av} (pA)	$\frac{(\Delta z)_{rms}}{(\Delta z)_{ss}}$
1	0.0031 ± 0.0021	0.999 ± 0.008	1.1
10	0.0057 ± 0.0035	1.001 ± 0.001	2.0
100	0.0178 ± 0.0018	1.000 ± 0.003	6.3
1000	0.0508 ± 0.0321	1.000 ± 0.000	18.0
10000	0.177 ± 0.0983	1.000 ± 0.003	62.5

Table 5.3: Simulation results using a setpoint current of 1pA and a bandwidth of 100Hz

The program used this value in a procedure which equated areas to determine a corresponding Gaussian distributed value.

The results of this computer simulation are shown in table 5.3. The setpoint current used was 1pA with a bandwidth of 100Hz. Because of the small bandwidth, the calculated values should match the small signal approximation, which is 0.00283Å. The last column is a ratio of calculated values to the value determined by the small signal approximation. The ratio grows with increasing number of iterations. The calculated value is approximately $0.6\sqrt{N}$ times greater then the small signal value. Even though the uncertainty in the tip-to-sample separation is growing, the average current still remains at the setpoint value, however. These results suggest that the control system is fluctuating about the nominal separation, and that this fluctuation is growing. This growth is the manifestation of the assumption made earlier that $G(f)K_1K_2 \gg 1$. As stated, this can lead to oscillations and even instabililty. To counteract this, the gain must be decreased.

Decreasing the system gain would reduce the large variations in the tunneling current demanded by the control system in its attempts to eliminate the noise. As a result, the instantaneous tunneling current would be closely approximated by the setpoint value. This, of course, is the assumption made during the small signal analysis and the first portion of the large signal analysis. Therefore, their results provide a good indication of the fundamental limitations of the STM.

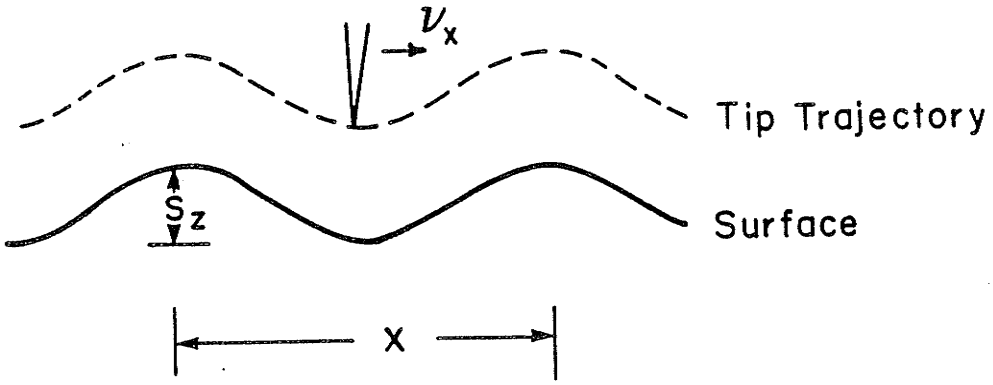

Figure 5.7: Surface with a sinusoidal variation

5.6 Scanning Rate

The maximum rate at which the tip can be scanned laterally over the surface is also determined by the bandwidth of the control system, as well as the shot noise in the junction. To determine the effect of the limited bandwidth and the shot noise, an additional assumption must be made. This is that the tip is moving both vertically and laterally above the surface.

Consider the surface shown in figure 5.7, which is assumed to have a sinusoidal variation in its height. The apparent frequency of the surface, f_s, is determined by the distance between peaks x and the lateral velocity of the tip v_x and is:

$$f_s = \frac{v_x}{x} \tag{5.64}$$

When $f_s > \Delta f$, the control system is not fast enough to react to the variations and as a result, the surface appears flat. However, when $f_s < \Delta f$, the control system responds at the same frequency, and the tip is able to follow the surface perfectly, *in the absence of noise.*

Because of noise, the vertical position of the tip varies even when the surface is essentially flat, yielding what may be misinterpreted as a surface feature. In addition, variations in the surface may be missed if the noise is so great that it masks these

variations. The probability of the noise being interpreted as a surface feature, or of a surface feature being masked by the noise, depends on the distribution of the noise. For this analysis, the distribution is assumed to be Gaussian. This implies that the instrument is not being operated at a setpoint current and a bandwidth where the average number of electrons traversing the tunnel junction is small.

With no surface features present, the average variation in the tip height is zero, whereas the average will be s_z (see figure 5.7) when a feature is present. The distribution of the tip height for these two situations is shown in figure 5.8. An error occurs when the surface is seen to be flat when in fact a feature is present or when a feature is deemed to be present when none exists. The probability of an error being made can be found from the overlap of the two distributions shown in figure 5.8. In a similar situation, Lathi[105] found that the probability of an error occuring is given by:

$$P_e = \frac{1}{\sqrt{2\pi}\sigma_z}\int_{s_z/2}^{\infty} \exp\frac{-z^2}{2\sigma_z}\,dz \tag{5.65}$$

$$= \operatorname{erfc}\left(\frac{s_z}{2\sigma_z}\right) \tag{5.66}$$

$$= \operatorname{erfc}\left(\frac{\mathrm{SNR}}{2}\right) \tag{5.67}$$

This assumes that the decision threshold between the two distributions is $s_z/2$. Lathi determined that such a threshold minimizes the error.

Therefore, a given P_e will yield a value, through the erfc, which is equal to the desired SNR. The corrugation value, s_z is also pre-determined. As a result, the tolerable noise-induced deviation in the tip height, Δz can be calculated by:

$$\Delta z = \frac{s_z}{\mathrm{SNR}} \tag{5.68}$$

This Δz can be used to calculate the needed bandwidth Δf, given a particular setpoint current. For example, using the small signal approximation, the bandwidth becomes:

$$\Delta f = \frac{\phi I_s}{2e}\left[\frac{As_z}{\mathrm{SNR}}\right]^2 \tag{5.69}$$

This bandwidth then determines the maximum frequency f_s and hence the scanning speed of the tip. For example, table 5.4 shows the limiting bandwidth and associated

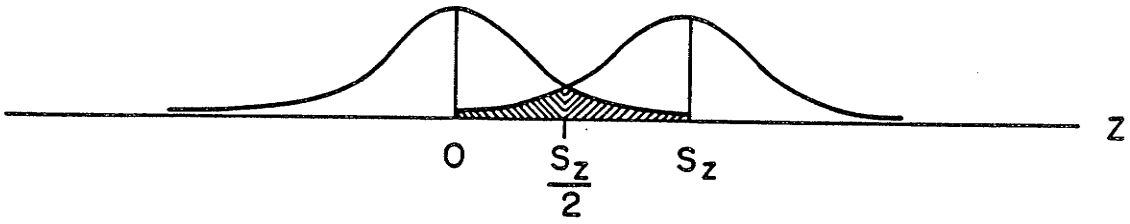

Figure 5.8: Tip height distributions. Either lined area represents the probability of an error

current (pA)	Δf (MHz)	v_x (μm/s)
1	0.078	0.063
10	0.78	0.63
100	7.8	6.3
1nA	78.	63.
10nA	780	630

Table 5.4: Maximum tip speed yielding an error probability of 10^{-10}

tip speed for a number of different currents. The error probability was 10^{-10}, which gives a SNR of 12.7. This error probability will result in only one error occurring when the surface contains a matrix of 10^5 by 10^5 possible features. The surface corrugation is assumed to be 1Å with a spacing between feature centers of 5Å. The small signal approximation was used to determine the bandwidths. The resulting bandwidths are quite high; consequently, the scanning speed does not appear to be a primary limitation.

5.7 Conclusions

The following can be concluded from the analysis presented here:

1. shot noise inherent in the tunneling current manifests itself as an uncertainty in the vertical position of the tip,

2. for good resolution, this uncertainty should be maintained below 0.01Å; this results in a bandwidth limitation of 1MHz at a setpoint current of 1nA,

3. operating at higher frequencies results in increasing uncertainty in the vertical position of the tip; eventually, this uncertainty will result in a crash of the tip into the surface,

4. at setpoint currents above 1nA, the limiting bandwidths are well into the MHz and as a result should not effect the design or operation of realizable STM's,

5. for smaller currents around 1 to 10pA, generally used for biological imaging, the bandwidth limitation of tens to hundreds of kilohertz may effect the design and operation of realizable instruments,

6. tip speed does not appear to be a primary limitation; instead, other factors, such as vertical resolution, result in more stringent bandwidth limitations.

Chapter 6

Recommendations

Future experiments and analyses should continue in each of the three main areas described in this thesis. With regards to the deposition experiments, the following should be addressed:

- additional experiments with the single crystal W tips, at the higher bias voltages should be undertaken,
- these experiments should be conducted in inert, vacuum and water vapour saturated ambients,
- the aim of these experiments should be to further separate and clarify the different deposition mechanisms,
- during the experiments, nothing should be deposited when no deliberately introduced material is present.

Additional work involving the *n*-alkanes should include:

- barrier height imaging to further examine and explain the imaging mechanisms,
- experiments involving *n*-alkane-like systems performed in order to examine possible variations in the imaging mechanism.

Further analysis of the control system should be undertaken to:

- determine the fundamental limitations imposed by other noise sources, such as thermal noise,
- incorporate a method of damping into the computer simulation, while ensuring that no loss of generality occurs.

References

[1] J.R. Oppenheimer, "Quantum Theory of Aperiodic Effects," *Phys. Rev.* **31**, 66 (1928).

[2] R.H. Fowler and L. Nordheim, "Electron Emission in Intense Electric Fields," *Proc. Roy. Soc. Lond. A* **119**, 173 (1928).

[3] J. Frenkel, "On the Electrical Resistance of Contacts Between Solid Conductors," *Phys. Rev.* **36**, 1604 (1930).

[4] L. Esaki, "New Phenomenon in Narrow Germanium p-n Junctions," *Phys. Rev.* **109**, 603 (1958).

[5] R.C. Jaklevic and J. Lambe, "Molecular Vibration Spectra by Electron Tunneling," *Phys. Rev. Lett.* **17**, 1139 (1966).

[6] R. Young, J. Ward and F. Scire, "The Topografiner: An Instrument for Measuring Surface Microtopography," *Rev. Sci. Instrum.* **43**, 999 (1972).

[7] G. Binnig, H. Rohrer, Ch. Gerber and E. Weibel, "Tunneling through a controllable vacuum gap," *Appl. Phys. Lett.* **40**, 178 (1982).

[8] G. Binnig, H. Rohrer, Ch. Gerber and E. Weibel, "Surface Studies by Scanning Tunneling Microscopy," *Phys. Rev. Lett.* **49**, 57 (1982).

[9] G. Binnig and H. Rohrer, "Scanning Tunneling Microscopy," *Surf. Sci.* **126**, 236 (1983).

[10] J.G. Simmons, "Generalized Formula for the Electric Tunnel Effect between Similar Electrodes Separated by a Thin Insulating Film," *J. Appl. Phys.* **34**, 1793 (1963).

[11] C.F. Quate, "Vacuum tunneling: A new technique for microscopy," *Physics Today* **39**, 26, August (1986).

[12] G. Binnig and D.P.E. Smith, "Single-tube three-dimensional scanner for scanning tunneling microscopy," *Rev. Sci. Instrum.* **57**, 1688 (1986).

[13] J.A. Golovchenko, "The Tunneling Microscope: A New Look at the Atomic World," *Science* **232**, 48 (1986).

[14] D.P.E. Smith and G. Binnig, "Ultrasmall scanning tunneling microscope for use in a liquid-helium storage Dewar," *Rev. Sci. Instrum.* **57**, 2630 (1986).

[15] J. Bardeen, "Tunnelling from a many-particle point of view," *Phys. Rev. Lett.* **6**, 57 (1961).

[16] J. Tersoff and D.R. Hamann, "Theory of the scanning tunneling microscope," *Phys. Rev. B* **31**, 805 (1985).

[17] N.D. Lang, "Vacuum Tunneling Current from an Adsorbed Atom," *Phys. Rev. Lett.* **55**, 230 (1985).

[18] D.J. Thomson, private communication.

[19] C.J. Chen, "Origin of atomic resolution on metal surfaces in scanning tunneling microscopy," preprint, journal and date not known

[20] J. Tersoff, "Anomalous Corrugations in Scanning Tunneling Microscopy: Imaging of Individual States," *Phys. Rev. Lett.* **57**, 440 (1986).

[21] J.M. Soler, A.M. Baro, N. García, and H. Rohrer, "Interatomic Forces in Scanning Tunneling Microscopy: Giant Corrugations of the Graphite Surface," *Phys. Rev. Lett.* **57**, 444 (1986).

[22] J.B. Pethica, "Comment on "Interatomic Forces in Scanning Tunneling Microscopy: Giant Corrugations of the Graphite Surface"," *Phys. Rev. Lett.* **57**, 3235 (1986).

[23] J.H. Coombs and J.B. Pethica, "Properties of vacuum tunneling currents: Anomalous barrier heights," *IBM J. Res. Develop.* **30**, 455 (1986).

[24] H.J. Mamin, E. Ganz, D.W. Abraham, R.E. Thomson and J. Clarke, "Contamination-mediated deformation of graphite by the scanning tunneling microscope," *Phys. Rev. Lett.* **34**, 9015 (1986).

[25] G. Binnig and H. Rohrer, "Scanning tunneling microscopy," *IBM J. Res. Develop.* **30**, 355 (1986).

[26] R.J. Behm and W. Hösler, "Scanning Tunneling Microscopy," in *Chemistry and Physics of Solid Surfaces VI,* ed. by R. Vanselow and R. Howe, Chap. 14, Springer-Verlag, Berlin, 1986.

[27] R.C. Jaklevic and J. Lambe, in *Tunneling Phenomena in Solids,* ed. by E. Burnstein and S. Lundqvist, Chap. 18, Plenum, New York, 1969.

[28] W.J. Kaiser and R.C. Jaklevic, "Spectroscopy of electronic states of metals with a scanning tunneling microscope," *IBM J. Res. Develop.* **30**, 411 (1986).

[29] G. Binnig, N. García and H. Rohrer, "Conductivity sensitivity of inelastic scanning tunneling microscopy," *Phys. Rev. B* **32**, 1336 (1985).

[30] A.L. deLozanne, S.A. Elrod and C.F. Quate, "Spatial Variations in the Superconductivity of Nb_3Sn Measured by Low-Temperature Tunneling Microscopy," *Phys. Rev. Lett.* **54**, 2433 (1985).

[31] G. Binnig, N. García, H. Rohrer, J.M. Soler and F. Flores, "Electron-metal interaction potential with vacuum tunneling: Observation of the image force," *Phys. Rev. B* **30**, 4816 (1984).

[32] M.C. Payne and J.C. Inkson, "Measurement of Workfunctions by Tunneling and the Effect of the Image Potential," *Surf. Sci.* **159**, 485 (1985).

[33] J.H. Coombs, M.E. Welland and J.B. Pethica, "Experimental Barrier Heights and the Image Potential in Scanning Tunneling Microscopy," *Surf. Sci.* **198**, L353 (1988).

[34] J.M. Pitarke, P.M. Echenique and F. Flores, "Apparent Barrier Height for Tunneling Electrons in STM," *Surf. Sci.* **217**, 2672 (1989).

[35] N.D. Lang, "Apparent barrier height in scanning tunneling microscopy," *Phys. Rev. B* **37**, 10395 (1988).

[36] J.M Gómez-Rodríguez, J. Gómez-Herrero and A.M. Baró, "Imaging cos(s,z): A Method to Separate the Geometric and Compositional Contributions on STM Barrier Height Profiles," *Surf. Sci.* **220**, 152 (1989).

[37] M.A. McCord and R.F.W. Pease, "High resolution, low-voltage probes from a field emission source close to the target plane," *J. Vac. Sci. Technol. B* **3**, 198 (1985).

[38] M.A. McCord and R.F.W. Pease, "The Effect of Reflected and Secondary Electrons on Lithography with the Scanning Tunneling Microscope," *Surf. Sci.* **181**, 278 (1987).

[39] M.A. McCord and R.F.W. Pease, "Lithography with the scanning tunneling microscope," *J. Vac. Sci. Technol. B* **4**, 86 (1986).

[40] M.A. McCord and R.F.W. Pease, "Exposure of calcium fluoride resist with the scanning tunneling microscope," *J. Vac. Sci. Technol. B* **5**, 430 (1987).

[41] M.A. McCord and R.F.W. Pease, "Lift-off metallization using poly(methyl methacrylate) exposed with a scanning tunneling microscope," *J. Vac. Sci. Technol. B* **6**, 293 (1988).

[42] M.A. McCord, D.P.Kern and T.H.P. Chang, "Direct deposition of 10-nm metallic features with the scanning tunneling microscope," *J. Vac. Sci. Technol. B* **6**, 1877 (1988).

[43] R.M. Silver, E.E. Ehrichs and A.L. deLozanne, "Direct writing of submicron metallic features with a scanning tunneling microscope," *Appl. Phys. Lett.* **51**, 247 (1987).

[44] E.E. Ehrichs, S. Yoon and A.L. deLozanne, "Direct writing of 10 nm features with the scanning tunneling microscope," *Appl. Phys. Lett.* **53**, 2287 (1988).

[45] C.W. Lin, F.-R.F. Fan and A.J.Bard, "High Resolution Photoelectrochemical Etching of n-GaAs with the Scanning Electrochemical and Tunneling Microscope," *J. Electrochem. Soc.* **134**, 1038 (1987).

[46] M.A. McCord and R.F.W. Pease, "Scanning tunneling microscope as a micromechanical tool," *Appl. Phys. Lett.* **50**, 569 (1987).

[47] R.C. Jaklevic and L. Elie, "Scanning-Tunneling-Microscope Observation of Surface Diffusion on an Atomic Scale: Au on Au(111)," *Phys. Rev. Lett.* **60**, 120 (1988).

[48] E.J. van Loenen, D. Dijkamp, A.J. Hoeven, J.M. Lenssinck and J. Dieleman, "Nanometer Scale Structuring of Silicon by Direct Indentation," *J. Vac. Sci. Technol. A* **8**, 574 (1990).

[49] E.J. van Loenen, D. Dijkamp, A.J. Hoeven, J.M. Lenssinck and J. Dieleman, "Direct writing in Si with a scanning tunneling microscope," *Appl. Phys. Lett.* **55**, 1312, (1989).

[50] U. Staufer, R. Wiesendanger, L. Eng, L. Rosenthaler, H.R. Hidber, H.-J. Güntherodt and N. García, "Nanometer scale structure fabrication with the scanning tunneling microscope," *Appl. Phys. Lett.* **51**, 244 (1987).

[51] U. Staufer, R. Wiesendanger, L. Eng, L. Rosenthaler, H.R. Hidber, H.-J. Güntherodt and N. García, "Surface modification in the nanometer range by the scanning tunneling microscope," *J. Vac. Sci. Technol. A* **6**, 537 (1988).

[52] U. Staufer, L. Scandella and R. Wiesendanger, "Direct Writing of Nanometer Scale Structures on Glassy Metals by the Scanning Tunneling Microscope," *Z. Phys. B* **77**, 281, (1989).

[53] M. Ringger, H.R. Hidber, R. Schlögl, P. Oelhafen and H.-J. Güntherodt, "Nanometer lithography with the scanning tunneling microscope," *Appl. Phys. Lett.* **46**, 832 (1985).

[54] D.W. Abraham, H.J. Mamin, E. Ganz and J. Clarke, "Surface modification with the scanning tunneling microscope," *IBM J. Res. Develop.* **30**, 492 (1986).

[55] J. Schneir, R Sonnenfeld, O. Marti, P.K. Hansma, J.E. Demuth and R.J. Hamers, "Tunneling microscopy, lithography, and surface diffusion on an easily prepared, atomically flat gold surface," *J. Appl. Phys.* **63**, 717 (1988).

[56] J. Schneir, O. Marti, G. Remmers, D. Gläser, R Sonnenfeld, B. Drake, P.K. Hansma and V. Elings, "Scanning tunneling microscopy and atomic force microscopy of the liquid-solid interface," *J. Vac. Sci. Technol. A* **6**, 283 (1988).

[57] Y.Z. Li, L. Vasquez, R. Piner, R.P. Andres and R. Reifenburger, "Writing nanometer-scale symbols in gold using the scanning tunneling microscope," *Appl. Phys. Lett.* **54**, 1424 (1989).

[58] R. Emch, J. Nogami, M.M. Dovek, C.A. Lang and C.F. Quate, "Characterization of gold surfaces for use as substrates in scanning tunneling microscopy studies," *J. Appl. Phys.* **65**, 79 (1989).

[59] T.R. Albrecht, M.M Dovek, C.A. Lang, P. Grütter, C.F. Quate, S.W.J. Kuan, C.W. Frank and R.F.W. Pease, "Imaging and modification of polymers by scanning tunneling and atomic force microscopy," *J. Appl. Phys.* **64**, 1178 (1988).

[60] T.R. Albrecht, M.M Dovek, C.A. Lang, C.F. Quate and D.P.E. Smith, "Nanometer-scale hole formation on graphite using a scanning tunneling microscope," *Appl. Phys. Lett.* **55**, 1727 (1989).

[61] J.S. Foster, J.E. Frommer and P.C. Arnett, "Molecular manipulation using a tunnelling microscope," *Nature* **331**, 324 (1988).

[62] R.S. Becker, J.A. Golovchenko and B.S. Swartzentruber, "Atomic-scale surface modifications using a tunnelling microscope," *Nature* **325**, 419 (1987).

[63] J. Jahanmir, P.E. West, S. Hsieh and T.N. Rodin, "Surface modification of *a*-Si:H with a scanning tunneling microscope operated in air," *J. Appl. Phys.* **65**, 2064 (1989).

[64] Technical Staff, *Digital Instruments NanoScope^{TM} I Scanning Tunneling Microscope Instruction Manual Version 1.1,* Digital Instruments Inc. Santa Barbara, California, 1988.

[65] Sang-il Park, J. Nogami and C.F. Quate, "Effect of tip morphology on images obtained by scanning tunneling microscopy," *Phys. Rev. B* **36**, 2863 (1987).

[66] H.A. Mizes, Sang-il Park and W.A. Harrison, "Multiple-tip interpretation of anomalous scanning-tunneling-microscopy images of layered materials," *Phys. Rev. B* **36**, 4491 (1987).

[67] R.J. Colton, S.M. Baker, R.J. Driscoll, M.G. Youngquist and J.D. Baldeschwieler, "Imaging graphite in air by scanning tunneling microscopy: Role of the tip," *J. Vac. Sci. Technol. A* **6**, 349 (1988).

[68] T.R. Albrecht, H.A. Mizes, J Nogami, Sang-il Park and C.F. Quate, "Observation of tilt boundaries in graphite by scanning tunneling microscopy and associated mulitple tip effects," *Appl. Phys. Lett.* **52**, 362 (1988).

[69] R.J. Colton, S.M. Baker, J.D. Baldeschwieler and W.J. Kaiser, " "Oxide-free" tip for scanning tunneling microscopy," *Appl. Phys. Lett.* **51**, 305 (1987).

[70] M.J. Heben, M.M. Dovek, N.S. Lewis, R.M. Penner and C.F. Quate, "Preparation of STM tips for *in-situ* characterization of electrode surfaces," *J. Microsc.* **152**, 651, (1988).

[71] E.W. Müller and T.T. Tsong, *Field Ion Microscopy, Principles and Applications,* American Elsevier, New York, 1969.

[72] J.J. Hren and S. Ranganathan, *Field-Ion Microscopy,* Plenum, New York, 1968.

[73] K.M. Bowkett and D.A. Smith, *Field-Ion Microscopy,* North-Holland, Amsterdam, 1970.

[74] P.J. Bryant, H.S. Kim, Y.C. Zheng and R. Yang, "Technique for shaping scanning tunneling microscope tips," *Rev. Sci. Instrum.* **58**, 1115 (1987).

[75] R. Nicolaides, Y. Liang, W.E. Packard, Z.W. Fu, H.A. Blackstead, K.K. Chin, J.D. Dow, J.K. Furdyna, W.M. Hu, R.C. Jaklevic, W.J. Kaiser, A.R. Penton, M.V. Zeller and J. Bellina, Jr. "Scanning tunneling microscope tip structures," *J. Vac. Sci. Technol. A* **6**, 445 (1988).

[76] D.K. Biegelsen, F.A. Ponce, J.C. Tramontana and S.M. Koch, "Ion milled tips for scanning tunneling microscopy," *Appl. Phys. Lett.* **50**, 696 (1987).

[77] D.K. Biegelsen, F.A. Ponce, and J.C. Tramontana "Simple ion milling preparation of <111> tungsten tips," *Appl. Phys. Lett.* **54**, 1223 (1989).

[78] T. Tiedje, J. Varon, H. Deckman and J. Stokes, "Tip contamination effects in ambient pressure scanning tunneling microscopy imaging of graphite," *J. Vac. Sci. Technol. A* **6**, 372 (1988).

[79] H.-W. Fink, "Mono-atomic tips for scanning tunneling microscopy," *IBM J. Res. Develop.* **30**, 460 (1986).

[80] V.T Binh and J. Marien, "Characterization of Microtips for Scanning Tunneling Microscopy," *Surf. Sci.* **202**, L359 (1988).

[81] V.T Binh, "*In-situ* fabrication and regeneration of microtips for scanning tunnelling microscopy," *J. Microsc.* **152**, 355, (1988).

[82] H. Neffermeyer and M. Drechsler, "Electric field-induced changes of W(110) and W(111) tips," *J. Microsc.* **152**, 459, (1988).

[83] R.H. Bernhardt, G.C. McGonigal, R. Schneider and D.J. Thomson, "Mechanisms for the deposition of nanometer-sized structures from organic fluids using the scanning tunneling microscope," *J. Vac. Sci. Technol. A* **8**, 667 (1990).

[84] I.P. Batra, N. García, H. Rohrer, H Salemink, E. Stoll and S. Ciraci, "A Study of Graphite Surface with STM and Electronic Structure Calculations," *Surf. Sci.* **181**, 126 (1987).

[85] J. Suzanne, J.L. Seguin, H. Taub and J.P. Biberian, "A LEED study of ethane adsorbed on graphite in the monolayer range," *Surf. Sci.* **125**, 153 (1983).

[86] J. Suzanne, "Phase transitions, dynamics and orientational ordering in hydrocarbon molecules adsorbed on graphite," in *Adsorption at the gas-solid and liquid-solid interface,* ed. by J. Rouquerol and K.S.W. Sing, pg. 421, Elsevier, Amsterdam, 1982.

[87] A.J. Groszek, "Selective adsorption at graphite/hydrocarbon interfaces," *Proc. Roy. Soc. Lond. A* **314**, 473 (1970).

[88] D.H. Everett and G.H. Findenegg, "Calorimetric Evidence for the Structure of Films adsorbed at the Solid/Liquid Interface: the Heats of Wetting of 'Graphon' by some n-Alkanes," *Nature* **223**, 52 (1969).

[89] G.C. McGonigal, R.H. Bernhardt and D.J. Thomson, "Imaging alkane layers at the liquid/graphite interface with the scanning tunneling microscope," submitted to *Appl. Phys. Lett.* , January 1990.

[90] A.I. Kitaigorodsky, *Molecular Crystals and Molecules,* Academic Press, New York, 1973.

[91] J.K. Spong, H.A. Mizes, L.J. LaComb Jr, M.M. Dovek, J.E. Frommer, and J.S. Foster, "Contrast mechanism for resolving organic molecules with tunnelling microscopy," *Nature* **338**, 137 (1989).

[92] D.P.E. Smith, H.H. Hörber and G. Binnig, "Alkylcyanobiphenyl molecules studied by tunneling microscopy: Determination of graphite registry and molecular orbital calculations," accepted by *Nature*, January 1990.

[93] D.J. Thomson, private communication.

[94] B. Michel, G. Travaglini, H. Rohrer, C. Joachim and M. Amrein, "Images of crystalline alkanes obtained with scanning tunneling microscopy," *Z. Phys. B* **76**, 99 (1989).

[95] D.W. Pohl, "Some design criteria in scanning tunneling microscopy," *IBM J. Res. Develop.* **30**, 417 (1986).

[96] Sang-il Park and C.F. Quate, "Theories of the feedback and vibration isolation systems for the scanning tunneling microscope," *Rev. Sci. Instrum.* **58**, 2004 (1987).

[97] Y. Kuk and P.J. Silverman, "Scanning tunneling microscope instrumentation", *Rev. Sci. Instrum.* **60**, 167 (1989).

[98] D.P. DiLella, J.H. Windlass, R.J. Colton and C.R.K. Marrian, "Control systems for scanning tunneling microscopes with tube scanners," *Rev. Sci. Instrum.* **60**, 997 (1989).

[99] T. Tiedje and A. Brown, "Performance limits for the scanning tunneling microscope," preprint, April 1990.

[100] D.J. Thomson, "The STM as an information storage device," *J. Microscopy* **152**, 627 (1988).

[101] R.C. Dorf, *Modern Control Systems,* Addison-Wesley, Reading Mass., 5th Ed., pp. 35, 1989.

[102] R. King, *Electrical Noise,* Chapman and Hall, London, pp. 55, 1966.

[103] A.H. Sommer, *Photoemissive Materials Preparation, Properties and Uses,* John Wiley & Sons, New York, pp. 21, 1968.

[104] G.R. Cooper and C.D. McGillem, *Probabilistic Methods of Signal and System Analysis,* Holt, Rinehart and Winston, New York, pp. 227, 1971.

[105] B.P. Lathi, *Communications Systems,* John Wiley & Sons, New York, pp. 405, 1968.